

SNAPSHOT IMAGING SPECTROSCOPY OF THE SOLAR TRANSITION  
REGION: THE MULTI-ORDER SOLAR EUV SPECTROGRAPH (MOSES)  
SOUNDING ROCKET MISSION

by

James Lewis Fox

A dissertation submitted in partial fulfillment  
of the requirements for the degree

of

Doctor of Philosophy

in

Physics

MONTANA STATE UNIVERSITY  
Bozeman, Montana

April 2011

© Copyright

by

James Lewis Fox

2011

All Rights Reserved

APPROVAL

of a dissertation submitted by

James Lewis Fox

This dissertation has been read by each member of the dissertation committee and has been found to be satisfactory regarding content, English usage, format, citations, bibliographic style, and consistency, and is ready for submission to The Graduate School.

Dr. Charles C. Kankelborg

Approved for the Department of Physics

Dr. Richard J. Smith

Approved for The Graduate School

Dr. Carl A. Fox

### STATEMENT OF PERMISSION TO USE

In presenting this dissertation in partial fulfillment of the requirements for a doctoral degree at Montana State University, I agree that the Library shall make it available to borrowers under rules of the Library. I further agree that copying of this dissertation is allowable only for scholarly purposes, consistent with “fair use” as prescribed in the U.S. Copyright Law. Requests for extensive copying or reproduction of this dissertation should be referred to ProQuest Information and Learning, 300 North Zeeb Road, Ann Arbor, Michigan 48106, to whom I have granted “the exclusive right to reproduce and distribute my dissertation in and from microform along with the non-exclusive right to reproduce and distribute my abstract in any format in whole or in part.”

James Lewis Fox

April 2011

## DEDICATION

This work is the fulfillment of a life-long aspiration, the accomplishment of a goal set at age 5. I dedicate it to my father, who first sparked my interest in astronomy, who dared me to dream about the universe and imagine what might be in it, and who wouldn't let me give up when I thought I would never understand fractions. I dedicate it to my mother who believed I could do anything, and made me believe it as well. I dedicate it to my wife who gives my life purpose and direction, whose loving patience, care, and support mean so much.

## ACKNOWLEDGEMENTS

The *MOSES* sounding rocket is the work of many hands. So many have been involved it is difficult even to list them all, let alone to adequately thank them. What follows is my attempt to do so. I apologize in advance for any errors or omissions; they are unintentional.

First and foremost, I want to thank my adviser, Charles C. Kankelborg, for all he has taught me, and for all the ideas he has loaned to me, including the original idea itself. No student could ask for a more generous mentor. I express sincere appreciation to another mentor, our collaborator, Roger J. Thomas from Goddard Space Flight Center. He has meant so much to *MOSES* and to me.

I thank our many collaborators: Ritva Keski-Kuha, Scott Owens, and others at the GSFC optics branch; Roger J. Thomas, Marvin Swartz, and others at GSFC Solar Physics Laboratory; Len Culhane, Louise Harra, Phil Thomas, Ady James, and many others at Mullard Space Science Laboratory; Marilyn Bruner, Tom Metcalf, and Jean-Pierre Wuelser of Lockheed Martin Solar Astrophysical Laboratory; Barry Kent and many others at Rutherford Appleton Laboratory.

I express gratitude to the 52 *MOSES* students who put the rocket together, for their dedication and sacrifice. Some of those who worked with me most closely are named in chapter 3. I wish I had space to name them all and speak of their individual contributions.

The entire NASA Sounding Rocket Program team showed marvelous professionalism and fortitude. I thank them all, but especially want to mention by name those I worked with personally: Our telemetry engineers, Jim Diehl and John Aasen, worked with me closely, and went above and beyond the call; Bill Payne, our mission man-

ager; Ken Starr, who helped rebuild electronics at the range; Jesus Martinez, Carlos Martinez, and Chris Hoxworth in Attitude Control; Rick Evavold, Paul Evans, and Chris Christeson in Vehicle Systems; Lupe Archuleta and the PSL folks; and the ever-hospitable Becky Grzelachowski in the office.

I also express appreciation to Rick Nelson and the Navy crew at White Sands Missile Range. To Rick Nelson in particular I offer very personal thanks for his unintentional services as matchmaker. Rick changed my life much for the better, and forever, by reintroducing me to the woman who would become my wife, six years subsequent to our last acquaintance. Neither Rick nor I could have foreseen the happy result of that introduction. Thanks Rick!

Norm Williams, MSU Physics machine shop supervisor, and John Getty, formerly MSU Physics Electronics Design Laboratory supervisor, both went above and beyond the call of duty. Heartfelt thanks to both.

This work was supported by NASA Low Cost Access to Space grants NAG5-10997 and NNX-07AG6G. I was supported for three years by NASA Graduate Student Research Program fellowship grant NGT5-50471, and for two years by the Montana Space Grant Consortium fellowship program.

## TABLE OF CONTENTS

1. INTRODUCTION .....	1
2. THE <i>MOSES</i> CONCEPT, A TOMOGRAPHIC ANALOGUE.....	10
2.1 Instrument Concept .....	10
2.2 Limited Angle Tomography .....	12
2.3 Inversion .....	15
3. THE <i>MOSES</i> ROCKET.....	17
3.1 Optics .....	17
3.1.1 LOTS .....	18
3.1.2 Detectors .....	21
3.2 Focusing the <i>MOSES</i> Optics .....	24
3.3 Electronics and Software .....	29
3.3.1 Interfaces .....	31
3.3.1.1 NASA Interface.....	31
3.3.1.2 Wiring Harness .....	34
3.3.2 Flight Computer.....	34
3.3.3 Power Control Unit (PCU).....	35
3.3.4 Interface Control Unit (ICU) .....	36
3.3.4.1 Timers and Uplinks.....	37
3.3.4.2 Shutter .....	38
3.3.5 Thermal Control System (TCS).....	38
3.3.6 Thermistor Vacuum Gauge.....	39
3.3.7 Electronic Ground Support Equipment (EGSE).....	40
3.3.8 Software.....	40
3.4 Calibration .....	41
3.5 Range Operations .....	43
3.6 Launch and Mission Data.....	46
3.6.1 Data .....	47
4. OBTAINING INSTRUMENT FLAT-FIELD FROM A NON-UNIFORM SOURCE .....	55
4.1 Flat-fielding.....	55
4.2 In EUV .....	57
4.3 The Flat-field Experiment .....	58
4.4 Flat-field Experiment Data .....	61
4.5 The Algorithm .....	66
4.6 The First Pass .....	70

## TABLE OF CONTENTS – CONTINUED

4.7 Cross-correlation .....	73
4.8 The Second Pass .....	75
4.9 Acknowledgements .....	79
 5. A TRANSITION REGION EXPLOSIVE EVENT OBSERVED IN HE II WITH THE <i>MOSES</i> SOUNDING ROCKET .....	80
5.1 Introduction .....	80
5.2 Data Reduction .....	82
5.2.1 Alignment .....	83
5.3 Zero Order Data and Magnetic Context .....	83
5.4 Difference Images .....	88
5.5 Parallax Analysis .....	91
5.5.1 Procedure .....	92
5.6 Results .....	97
5.7 Discussion and Conclusions.....	107
 6. DATA INVERSION FOR THE MULTI-ORDER SOLAR EXTREME ULTRAVIOLET SPECTROGRAPH .....	110
6.1 Inversion of Simulated Data.....	111
6.1.1 Fourier Backprojection.....	112
6.1.2 Pixon Inversion .....	114
6.1.3 Smooth Multiplicative Algebraic Reconstruction Technique .....	120
6.2 Discussion of Simulation Results .....	124
6.3 Inversion of <i>MOSES</i> Flight Data .....	126
6.4 Flight Inversion Results and Discussion .....	130
6.5 Acknowledgements .....	132
 7. CONCLUSIONS .....	133
7.1 Potential Applications .....	135
 REFERENCES CITED.....	137
 APPENDICES .....	143
APPENDIX A: List of Acronyms .....	144
APPENDIX B: List of Supplemental Material .....	150
APPENDIX C: Instrument Aberrations .....	153

## LIST OF TABLES

Table	Page
3.1 Optical Characteristics .....	19
3.2 Optical Prescription .....	19
3.3 Electronics and Software subsystem team members.....	31
3.4 Catalog of flight exposures .....	50
5.1 Fit parameters for three cases .....	102
6.1 Comparison of true and reconstructed line profiles.....	125
6.2 Line parameters .....	128

## LIST OF FIGURES

Figure	Page
1.1 Imaging spectroscopy techniques .....	6
1.2 Skylab SO82A image .....	8
2.1 Conceptual sketch of <i>MOSES</i> .....	11
2.2 Projection diagram.....	13
2.3 Radon transform .....	14
3.1 Optical layout of <i>MOSES</i> .....	18
3.2 <i>MOSES</i> full assembly drawing .....	21
3.3 <i>MOSES</i> detector housings .....	23
3.4 Sketch of the focus experiment .....	25
3.5 Focus spot series .....	27
3.6 Focus spot series fits.....	28
3.7 Spot size parameters vs. focus position .....	29
3.8 Electronics system block diagram .....	30
3.9 Grounding and Isolation Scheme .....	32
3.10 The author operating the payload during I&T.....	44
3.11 Team members with the rocket .....	45
3.12 <i>MOSES</i> leaves the launch rail .....	46
3.13 GOES X-ray flux for the day of launch .....	48
3.14 Flight data, all 3 orders .....	49
3.15 Flight data, frame 21.....	51
3.16 Flight data, frame 22 .....	51
3.17 Flight data, frame 23 .....	52
3.18 Flight data, frame 20.....	52

## LIST OF FIGURES – CONTINUED

Figure	Page
3.19 Flight data, frame 24 .....	53
3.20 Flight data, frame 25 .....	53
3.21 Flight data, frame 26 .....	54
4.1 KPNO Mayall telescope dome flat .....	56
4.2 The witness slide .....	59
4.3 View through the rear chamber door. ....	62
4.4 View through the front chamber door. ....	63
4.5 Detector 5 average signal .....	63
4.6 Rescaled average signal .....	64
4.7 Cleaned average signal, Detector 5 .....	65
4.8 Clean data frames from adjacent positions .....	67
4.9 “Naive” fourier smoothing .....	70
4.10 Detector 5 flat-field, first pass .....	72
4.11 Detector 5 beam, first pass.....	72
4.12 Detector 5 residuals, first pass.....	73
4.13 Unfiltered cross-correlation.....	74
4.14 Filtered cross-correlation.....	75
4.15 Detector 5 flat-field, second pass.....	76
4.16 Detector 5 beam, second pass.....	76
4.17 Residuals for detector 5, position 3. ....	77
4.18 Flat-fields and beams for all detectors.....	78
5.1 <i>MOSES</i> zero order data frame .....	85
5.2 Comparison of +1 order, 0 order, and their difference .....	86
5.3 Explosive event light curve.....	87
5.4 Light curve ROI's.....	88

## LIST OF FIGURES – CONTINUED

Figure	Page
5.5 Comparison of MDI magnetogram and <i>MOSES</i> 0 order data .....	89
5.6 Sky-plane velocity calculation .....	90
5.7 Parallax analysis projection diagram.....	92
5.8 Raw data for line 768 .....	94
5.9 Background subtracted data, line 768 .....	96
5.10 Raw data for line 781 .....	97
5.11 Background subtracted data, line 781 .....	98
5.12 Raw data for line 792 .....	99
5.13 Background subtracted data, line 792 .....	100
5.14 Zero order data with gaussian parameters overlayed .....	101
5.15 Doppler shift as a function of $y$ axis position.....	104
5.16 Line width as a function of $y$ axis position .....	105
6.1 Fourier slice theorem .....	115
6.2 Backprojection reconstruction of simulated spectrum.....	116
6.3 Backprojection quartiles .....	117
6.4 Pixon basis .....	119
6.5 Pixon reconstruction of simulated spectrum .....	120
6.6 Pixon quartiles.....	121
6.7 SMART reconstruction of simulated spectrum.....	123
6.8 Systematic error in line center.....	126
6.9 Flight section used in inversion.....	127
6.10 Dopplergram of EE data.....	130
C.1 FOV for PSF demonstration .....	155
C.2 Comparison of flight data in FOV 1 and 2 .....	156
C.3 Comparison of flight data in FOV 3 and 4 .....	157

## LIST OF FIGURES – CONTINUED

Figure	Page
C.4 Difference image for FOV 1.....	158

## ABSTRACT

We have developed a revolutionary spectroscopic technique for solar research in the extreme ultraviolet. This slitless spectrographic technique allows snapshot imaging spectroscopy with data exactly cotemporal and cospectral. I have contributed to the successful realization of an application of this technique in the Multi-Order Solar EUV Spectrograph, *MOSES*. This instrument launched 2006 Feb 8 as a NASA sounding rocket payload and successfully returned remarkable data of the solar transition region in the He II 304 Å spectral line. The unique design of this spectrometer allows the study of transient phenomena in the solar atmosphere, with spatial, spectral, and temporal resolution heretofore unachievable in concert, over a wide field of view. The fundamental concepts behind the *MOSES* spectrometer are broadly applicable to many solar spectral lines and phenomena and the instrument thus represents a new instrumentation technology.

The early fruits of this labor are here reported: the first scientific discovery with the *MOSES* sounding rocket instrument, our observation of a transition region explosive event, phenomena observed with slit spectrographs since at least 1975, most commonly in lines of C IV (1548 Å, 1550 Å) and Si IV (1393 Å, 1402 Å). This explosive event is the first seen in He II 304 Å. With our novel slitless imaging spectrograph, we are able to see the spatial structure of the event. We observe a bright core expelling two jets that are distinctly non-collinear, in directions that are not anti-parallel, in contradiction to standard models of explosive events, which give collinear jets. The jets have sky-plane velocities of order  $75 \text{ km s}^{-1}$  and line-of-sight velocities of  $+75 \text{ km s}^{-1}$  (blue) and  $-30 \text{ km s}^{-1}$  (red). The core is a region of high non-thermal doppler broadening, characteristic of explosive events, with maximal broadening  $380 \text{ km s}^{-1}$  FWHM. It is possible to resolve the core broadening into red and blue line-of-sight components of maximum doppler velocities  $+160 \text{ km s}^{-1}$  and  $-220 \text{ km s}^{-1}$ . The event lasts more than 150 s. Its properties correspond to the larger, long-lived, and more energetic explosive events observed in other wavelengths.

Eleven supplemental files<sup>1</sup> are available on CD in Special Collections at the Montana State University Library. See appendix B for a description of supplemental material.

---

<sup>1</sup>36193\_DR.pdf, flightharness.pdf, HLP.pdf, MOSES\_MRR\_EDP.pdf, Launch.mov, MOSES\_flight\_sequence.mov, moses\_ff.tgz, moses\_coregistrate.tgz, EE\_1530\_0780.mov, moses\_pa.tgz, and smart3Dm.tgz

## CHAPTER 1

### INTRODUCTION

In 1835 the French philosopher August Comte, writing about the limitations of human knowledge, gave his famous opinion that humanity would never know what the stars are made of. He further opined that we would never know the chemical composition or temperature of the Sun or any of the planets, nor the rotation rate or density of any star (Comte, 1858). From the modern point of view it is astonishing how fabulously wrong he was. At the time of Comte's pronouncement the data that would prove him wrong already existed. In 1814 Joseph von Fraunhofer, at the time the maker of the finest optical glass in the world, observed the spectrum of the Sun using a prism on a small telescope. Contrary to the expectations of the time, he did not observe a smooth spectrum: certain narrow ranges of colors were missing. Fraunhofer observed and cataloged 574 absorption lines in the solar spectrum. Not knowing what they meant, he assigned them letters beginning in the red, with capital letters for stronger lines (or groups of lines), and lower case letters for weaker ones (Zirker, 2002; Zeilik et al., 1992).

In 1860, two years after Comte's death, Gustav Kirchhoff and Robert Bunsen (who invented his famous gas burner for the purpose of studying the spectra produced when elements were burned in it) discovered that materials had characteristic spectra; they identified the Fraunhofer D line as Sodium (Zirker, 2002). 5 years later two amateur astronomers, William Huggins and his wife Margaret, used Kirchhoff and Bunsen's results to determine what stars are made of (Huggins & Huggins, 1899).

Most of what we now know about the Sun comes from study of its spectrum beginning with Fraunhofer. While the absorption lines that Fraunhofer discovered come from cool gas absorbing light from the photosphere beneath it, other parts

of the solar spectrum contain emission lines from hot, highly ionized plasma. Such lines are found in the Far UltraViolet (FUV), Extreme UltraViolet (EUV) and X-ray spectral ranges and come from high in the solar atmosphere in the transition region, and corona. These lines cannot be observed from the ground due to the total absorption of the high-energy photons in Earth's atmosphere. Only by carrying instruments into space can we study this region of the solar spectrum and the parts of the solar atmosphere where it originates. Since the beginning of the space age dramatic advances in our understanding of the Sun's upper atmosphere have been made.

The aptly named transition region is a place of great change. A thin layer between the lower lying chromosphere and the corona above, the transition region starts at the relatively low temperature of  $\sim 20,000$  K, but only a few thousand km higher it is close to 1,000,000 K. While the chromosphere is dominated by optically thick absorption lines in the visible and FUV, the corona and transition region are dominated by optically thin emission lines that are only found in the FUV and EUV regions of the spectrum. The ionization state of the solar plasma also changes rapidly in the chromosphere and transition region, going from cooler areas where the emission is dominated by neutral atoms of H, and He, to the corona which is dominated by highly ionized heavier atoms, Si, Ne, or Fe. The plasma  $\beta$ , the ratio of gas pressure to magnetic pressure, also changes suddenly in these regions, going from  $\beta \gg 1$  in the photosphere below to  $\beta \ll 1$  in the corona above. All these sudden changes point to a region of the solar atmosphere, difficult to understand with the lack of simplifying assumptions, and highly dynamic. The transition region and chromosphere evolve rapidly. To study them we need space-borne instruments with high spatial and temporal resolution.

When viewed through a telescope in white light the Sun is a fairly featureless disk. Sunspots can be seen, but not much else; only very rarely do other solar features make their presence known in white light. A hint of the Sun's true complexity, hidden in the white light haze, could be glimpsed during solar eclipses, which revealed the corona and upper chromosphere to the naked eye. In 1890, George Ellery Hale invented the spectroheliograph, an instrument which takes pictures of the Sun in a single narrow wavelength band, allowing us to see the complex spatial and time-varying features of the Sun's atmosphere by singling out a particular part of the solar spectrum. Today spectroheliograph images are routinely made from the ground in the Fraunhofer lines of the visible spectrum. Improvements in narrow-band imaging technology have allowed us to observe the intricate structure and rapid evolution of the Sun at wavelengths throughout its spectrum, even in the FUV, EUV and X-ray regions. In modern times FUV/EUV narrow-band imagers are commonly made using multi-layer coatings, which reflect only wavelengths from a narrow range. Recent multi-layer imager instruments such as the TRACE (Handy et al., 1999) satellite, and now SDO/AIA have revolutionized our understanding of the transition region and corona. However to truly make sense of the physical processes that govern the solar atmosphere we will need more information than can be provided with imagers alone.

Spectroscopy allows measurement of a wealth of solar plasma parameters: temperature, density, pressure, magnetic field, doppler velocity, doppler broadening, can all be measured with choice of appropriate spectral lines. Such physical measurements are necessary for true understanding of solar behavior. Theories can be tested with such knowledge, as well as by their predictions of more subtle features of spectral lines than those attributable to a specific plasma parameter, such as self-reversals or asymmetric line profiles. Stigmatic spectroscopy uses a slit to restrict spatial information

along a single axis and spectral information along the other. A telescope forms an image of the Sun on the slit, and the spectrograph images the slit to obtain spatial resolution along it. It has generated valuable scientific results, but is limited due to lack of information in the other spatial dimension. It can be difficult to understand the context of dynamic events without a full spatial picture. Imagers provide such context, but lacking spectral information, do not produce the necessary data on physical properties of the plasma. Only the evolution of brightness and morphology can be studied. Therefore it is common to combine data from imagers and spectrographs to obtain a more complete picture of solar phenomena. In the conventional approach there are often difficulties in using the two types of instruments in concert. It is often troublesome, for example, to know precisely where the spectrograph slit lies in the field of view (FOV)<sup>1</sup>; the lack of spatial information in one axis makes coalignment tricky. Differences in spatial and temporal resolution limit data interpretation. More fundamentally the chosen location of the slit is always limiting. The slit will often miss interesting features in the imager data.

Imaging Spectroscopy is a fundamentally powerful observational technique, combining the features of an imager and a spectrograph. This capability is a key to understanding the physics of a complicated evolving source, such as the solar atmosphere. Image data is obtained as before, over some spectral bandpass and spatial field of view, but a spectrum is available at each spatial pixel in the image. It is also possible to view images at specific wavelengths within the bandpass, or integrated over sub-bands to separate the solar image in different closely spaced spectral lines.

The achievement of solar imaging spectroscopy has been realized in the realm of visible wavelengths for a number of years, via arrangements of optical narrowband

---

<sup>1</sup>This is not the case for a slit-jaw spectrograph.

tunable filters, such as Fabry-Pérot etalons (Scherrer et al., 1995; Bendlin et al., 1992, see references for examples). It can also be achieved by scanning the slit of a stigmatic spectrograph in the orthogonal spatial axis. Figure 1.1 illustrates how various types of instruments sample the Sun in hyper-spectral space, a hybrid space of two spatial ( $x, y$ ) dimensions and one spectral ( $\lambda$ ) dimension. The function of these dimensions that represents the Sun is called a “cube”. A tunable filtergraph device is shown schematically in green. Each filter position is an image of the Sun at a particular wavelength. The cube is built up by tuning the filter through the band-pass. A slit spectrograph is represented by magenta. The conventional spectrograph creates a spectrum with spatial resolution only along one dimension. Scanning the slit across the field of view samples the cube. In the EUV, imaging spectroscopy has been accomplished by scanning the slit of a stigmatic spectrograph across the field of view, as in the case of the *Coronal Diagnostic Spectrometer* (CDS) aboard the Solar and Heliospheric Observatory (*SOHO*) spacecraft (Kent et al., 1995).

Because the Sun is constantly evolving, complications can arise in imaging spectroscopy which are not a consideration in conventional spectroscopy or imaging. If the time required to scan over the cube is large compared to the timescale on which the Sun changes appreciably the spectra will not be cotemporal across the cube. This can cause misinterpretation of the data. For example, observers can be fooled into believing they have found a traveling wave, when no such wave exists (Settele et al., 2002). In the case of raster scanning the problem arises from spectra which are not cotemporal with those taken at other spatial locations. With tunable filters the problem arises from spectra that are not cotemporal in different parts of the spectrum.

What is needed is Snapshot Imaging Spectroscopy (SIS), where by “snapshot” we mean that the cube is built up faster than the Sun can evolve. The relevant

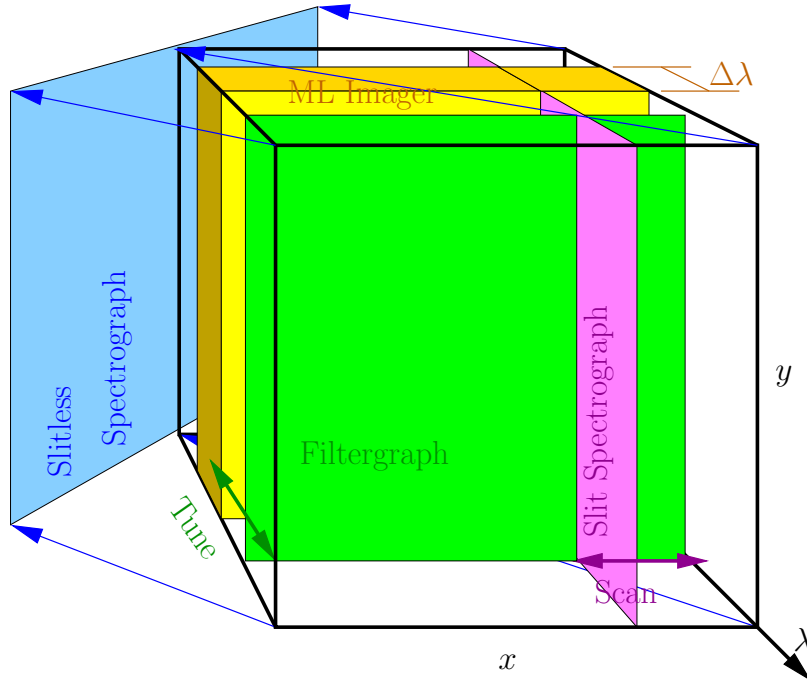


Figure 1.1: Imaging spectroscopy techniques and how they sample a hyper-spectral object. The region in  $(x, y, \lambda)$  space delineated by the FOV and bandpass is called an “image cube”, or just “cube”. For reference, a multi-layer (ML) imager has been diagrammed in yellow.

time-scale will depend on the particular solar phenomena under observation. In the visible regime, SIS has, in some measure, been achieved through advances in tunable filter technology. In the Extreme UltraViolet (EUV) SIS has remained elusive, largely due to the inherently low reflectivity of optics in this wavelength regime. Materials do not exist in nature which can achieve EUV reflectivities high enough to make possible a usable Fabry-Pérot etalon filtergraph (Gore, 1999). Transmission optics do not function in EUV; everything absorbs these wavelengths. Coupled with the much lower intensity of the Sun in EUV, as compared to visible, this limits the scanning speed of EUV imaging spectrographs. However, both methods are inherently photon inefficient. Whether by filter, or slit, most incident photons are thrown away before they can be detected.

Slitless spectroscopy defies the conventions of standard spectroscopy, throwing away the slit and not using a tunable filter (see chapter 2). In this approach all data are taken simultaneously over the whole field of view. There is no scanning, either spatially or spectrally, and hence no confusion of temporal evolution with spatial or spectral variation. Such slitless spectroscopy was accomplished by the Naval Research Laboratory’s Skylab *SO82A* instrument, nicknamed the “Overlappograph” because it resulted in overlapping images of the Sun. See figure 1.2. Such a slitless spectrograph is shown in blue in figure 1.1. The image on the detector is a projection at an angle through the cube (see §2.2). Such projections confuse spatial and spectral data along the dispersion axis.

By contrast our instrument, the Multi-Order Solar EUV Spectrograph (*MOSES*, see chapter 2) uses *multi-order* slitless spectroscopy. Multiple detectors measure data each from a different spectral order. Each order represents a different projection through the cube. By combining the data from multiple projections the contents of the cube can be inferred. Like single-order slitless spectroscopy there is no scanning; all data are exactly cotemporal. The data are taken in a snapshot, like an imager, but unlike an imager spectral information is recorded. This technique is also inherently photon efficient; far fewer photons are wasted, resulting in very high cadence instruments, with orders of magnitude more time resolution when compared to traditional imaging spectroscopy.

Multi-order slitless spectroscopy has been applied in the infrared and visible regimes; in those applications it is frequently referred to as Computed Tomography Imaging Spectroscopy (CTIS). Both transmissive and reflective systems have been built, frequently with up to 25 spectral orders, see Johnson et al. (2005); Descour et al. (1997); Wilson et al. (1997). Parallel developments in solar slitless spectroscopy

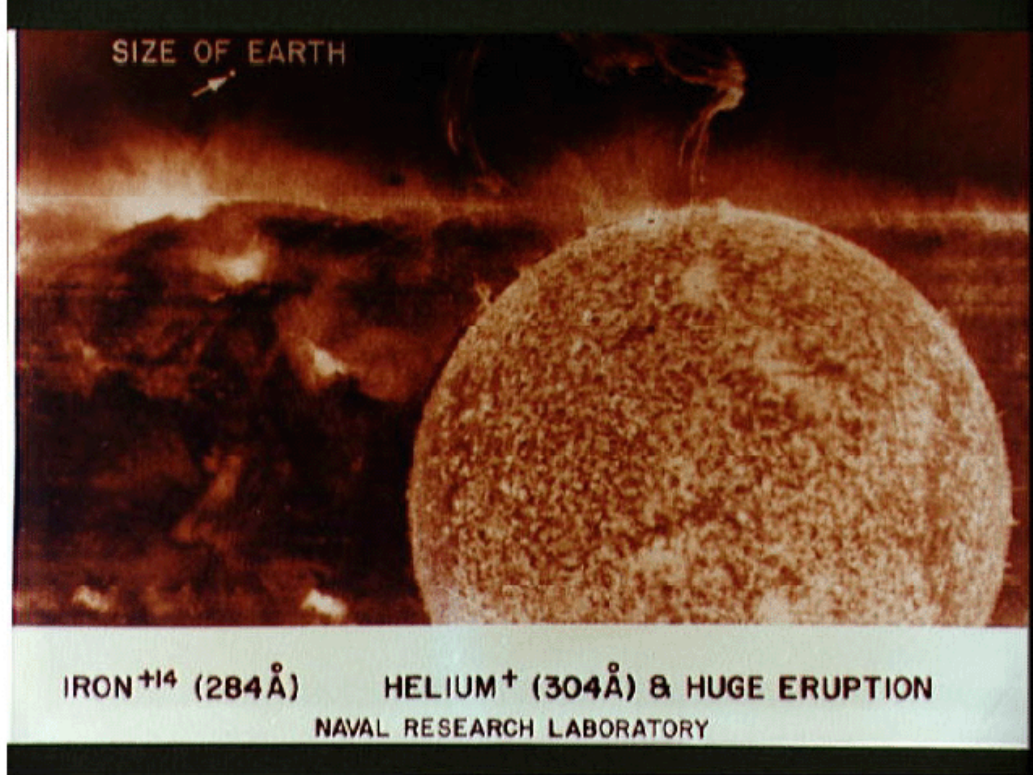


Figure 1.2: Part of an “overlappograph” image, 1 January 1974, from JSC Digital Image Collection. Lacking a slit the dispersion of the grating “smears out” the solar image. Well defined disk-like images of the Sun show the locations of strong spectral lines. In this image the strongest lines are He II 304 Å, the same line observed by *MOSES*, and Fe XV 284 Å.

are also being pursued by other research groups (DeForest, 2003; DeForest et al., 2004), but *MOSES* is the first of this class of instrument to operate in the EUV.

The *MOSES* instrument concept and its relation to tomography is covered in chapter 2. The *MOSES* instrument, based on the concept described in that chapter, has been built and flown successfully, launching 2006 Feb 8, as a NASA sounding rocket payload. Sounding rockets, which do not reach orbit, provide a relatively low-cost method of testing new ideas under flight conditions. A typical flight lasts 10 – 15 minutes. The data window for the *MOSES* flight was  $\sim$  5 minutes long.

Detailed description of the payload, optics, electronics, calibration, and launch are given in chapter 3. Flat-field calibration is discussed in chapter 4.

Chapter 5 describes the first result of the *MOSES* instrument: the discovery of a transition region explosive event with a structure at odds with typical models of such. This discovery is also discussed in Fox et al. (2010). We could not have made it with only an imager or only a spectrograph, nor with a conventional slit-scanning spectrograph, which would have been too slow to observe the dynamics of this highly transient event.

To reconstruct the cube from spatial and spectral information recorded at multiple orders, we must solve an ill-posed inversion problem. Chapter 6 discusses our initial work on such reconstructions. Portions of that chapter have also been published in Fox et al. (2003).

## CHAPTER 2

### THE *MOSES* CONCEPT, A TOMOGRAPHIC ANALOGUE

I will now briefly discuss the instrument concept (§2.1), its relationship to the problem of tomography (§2.2), and the inversion problem it presents (§2.3).

#### 2.1 Instrument Concept

The *MOSES* concept, illustrated in figure 2.1, was first described by Kankelborg & Thomas (2001). The instrument is a slitless, objective grating spectrograph. By taking images at multiple spectral orders, it is possible to acquire spatial and spectral information simultaneously over a wide field of view (FOV). In principle, detectors may be placed at any number of spectral orders. If more orders are recorded, more spectral information will be obtained.

The *MOSES* instrument obtains three images over the field of view, in a narrow passband about the He II 303.8 Å emission line. These three images correspond to spectral orders  $m = -1, 0, +1$ .

The diagram in figure 2.1 shows only the objective grating and detectors. It displays the effect of imaging an object which, for illustrative purposes, contains only the monochromatic letters “A” (red-ward of passband center) and “B” (blue-ward of passband center). In the  $m = 0$  order the letters are projected onto the same spatial location and overlap. In the  $m = +1, -1$  orders the spectral dispersion of the grating causes the letters to be separated on the detector by a distance proportional to the wavelength difference between them. Although they still overlap, as will typically be the case for an extended object, this separation allows us to infer the spectral content of the sources observed in the undispersed ( $m = 0$ ) image. Note that the information

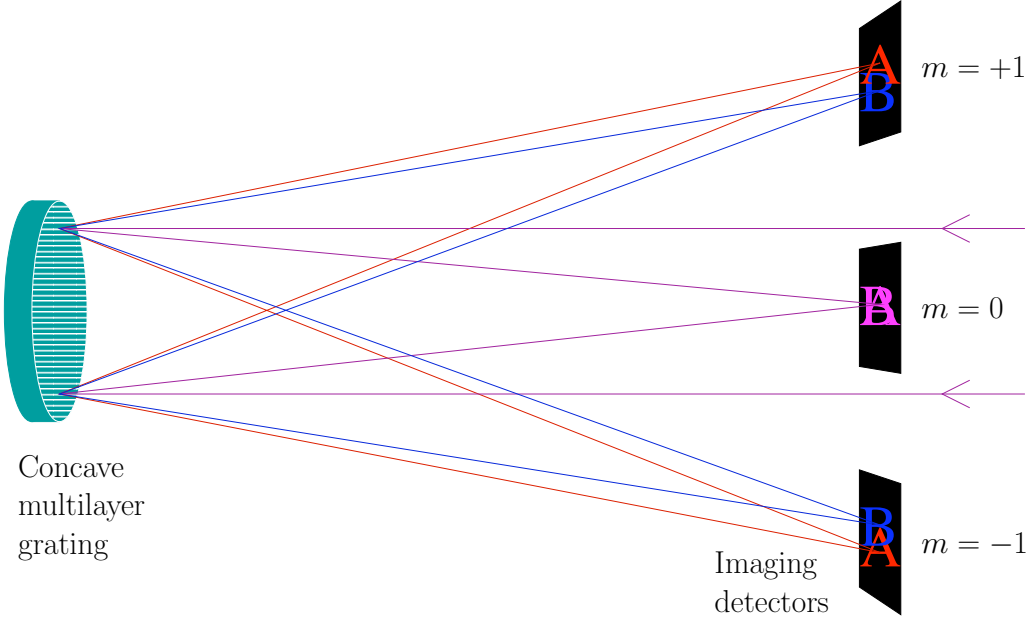


Figure 2.1: Conceptual sketch of *MOSES*.

in the  $m = +1$  and  $m = -1$  orders is not redundant. The direction of the  $+x$  spatial axis is unchanged (the letters are not flipped) but the wavelength axes are oppositely directed, causing us to read “ $_B^A$ ” in one order but “ $_A^B$ ” in the other.

Since there is no slit, each frame on the detector is an overlapping series of images of the Sun from spectral lines in the passband. The *MOSES* 2006 passband has only two: He II  $\lambda 303.8$  and Si XI  $\lambda 303.3$ . The projection of the Sun on the plane of the sky is an image “cube”, a 3-D function of  $(x, y, \lambda)$ . The grating has dispersion only in one direction, defined as the  $x$  axis. Each slice along the  $y$  axis will be independent of the others. To simplify the analysis conceptually and in practice we often consider a fixed value of  $y = y_0$ . The solar cube then collapses to a 2-D function  $v(x, \lambda)$  and the data become three 1-D intensity frames. The data are functions of a single coordinate  $x' = (x + m\lambda)$ , where  $x$  and  $\lambda$  are in pixel units. The mapping relating  $v(x, \lambda)$  to  $I_m(x + m\lambda)$  is analogous to tomography of a hybrid “object” in spatio-

spectral coordinates along three directions at  $(-45^\circ, 0^\circ, 45^\circ)$ ; this is shown in section 2.2. Analysis of the data can be carried out by forward-modeling or inversion to recover the image “cube” representing the part of the Sun which fits in our field of view and passband.

## 2.2 Limited Angle Tomography

I will now show that a direct correspondence exists between tomography and *MOSES*. Our instrument performs tomography on a “hyper-spectral” object with two spatial dimensions  $x$  and  $y$  and one spectral dimension  $\lambda$ . The three *MOSES* orders correspond to three different look-angles in conventional tomography. This correspondence is mathematically exact.

We generalize this discussion with the projection equation (eq. 2.1) depicted graphically in figure 2.2. The equation is cast in a form that allows consideration of a system with any number of spectral orders. The treatment is readily generalizable to include dispersion in the vertical as well as horizontal directions. An object  $v(x, y, \lambda)$  forms images at spectral orders  $m$ :

$$I_m(x', y') = \int_B v(x' - m\lambda, y', \lambda) d\lambda, \quad (2.1)$$

where  $(x', y')$  are the detector coordinates and domain  $B$  represents the passband of the instrument.<sup>1</sup> For the *MOSES* rocket experiment,  $m = (+1, 0, -1)$ . For convenience, position  $(x', y')$  on the detector, position  $(x, y)$  on the Sun, and wavelength  $\lambda$  are all measured in pixels. The kernel is a projection operator. For example, in the  $m = +1$  order, a pixel at position  $(x', y')$  receives light integrated (projected) along

---

<sup>1</sup>We find this formulation more natural than the notation developed previously in Kankelborg & Thomas (2001).

a slice  $x + \lambda = x'$  in the  $x\lambda$ -plane with  $y = y'$  a constant (compare figure 2.2). The integral equation 2.1 defines this operator, which we denote  $\mathbf{T}$ . It operates on  $v$  to produce the spectral order data,  $I_m = \mathbf{T}[v]$ .

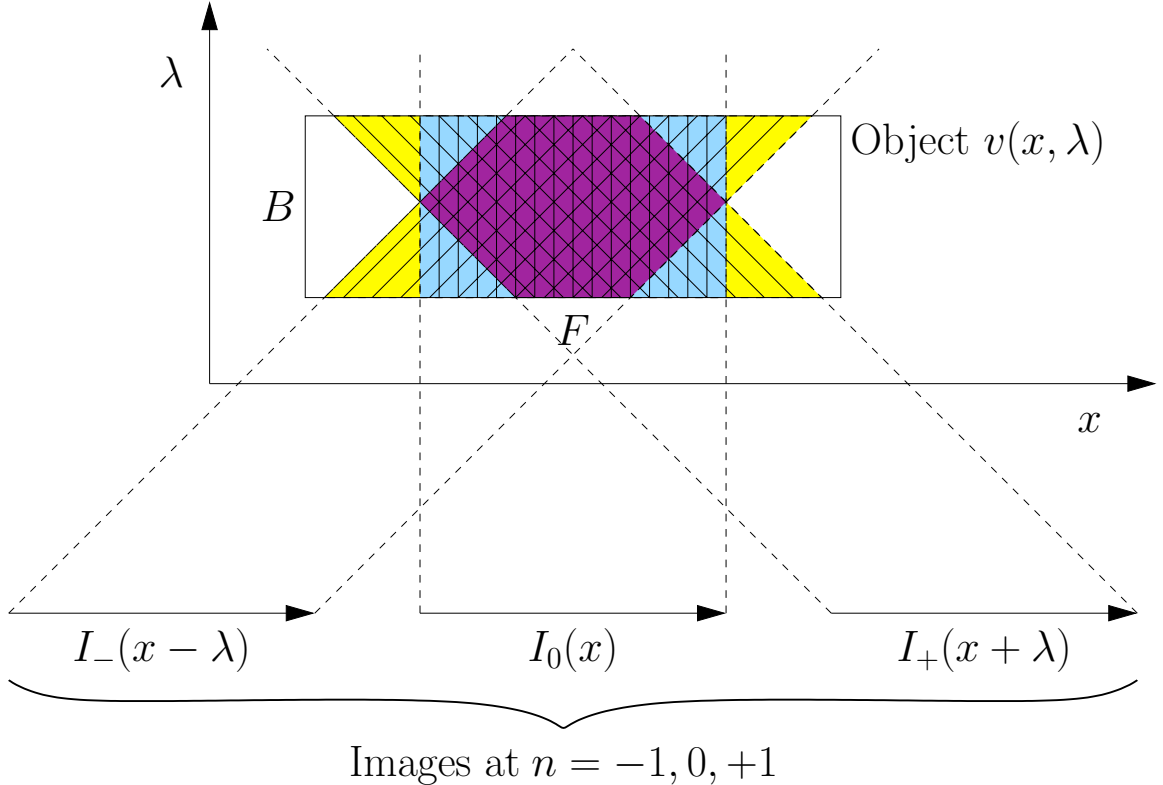


Figure 2.2: A projection diagram demonstrating how eq. 2.1 produces the 3 *MOSES* data orders by projection through the volume of a hyper-spectral object, mathematically equivalent to tomographic projection at 3 angles. The colors indicate the number of overlapping orders which sample a given region of  $(x, \lambda)$  space. Similar constructions apply for each  $y$ -slice of the image perpendicular to the spectrograph's dispersion plane.

Once the spectral orders are intercalibrated, the projections of  $v(x, y, \lambda)$  obey a normalization condition,

$$N = \int_F I_m dx = \int_B \int_F v dx d\lambda \quad (2.2)$$

for all orders  $m$ . The normalization condition holds exactly if the field of view is defined by a field stop prior to the dispersive element. Otherwise, the projections of the three orders will cover slightly different domains in  $(x, y, \lambda)$  at the edges of the field of view, as shown in figure 2.2.

The projection equation 2.1 is a form of the Radon transform (Kak & Slaney, 1988),  $R(m, x')$ , ordinarily parameterized as  $R(\alpha, s)$  where  $\tan \alpha = -1/m$  and  $s$  is related to  $x'$  by an additive constant. See figure 2.3. The *MOSES* images are three of the Radon transforms of the hyper-spectral cube. The *MOSES* inversion problem is an exercise in extreme Limited Angle Tomography.

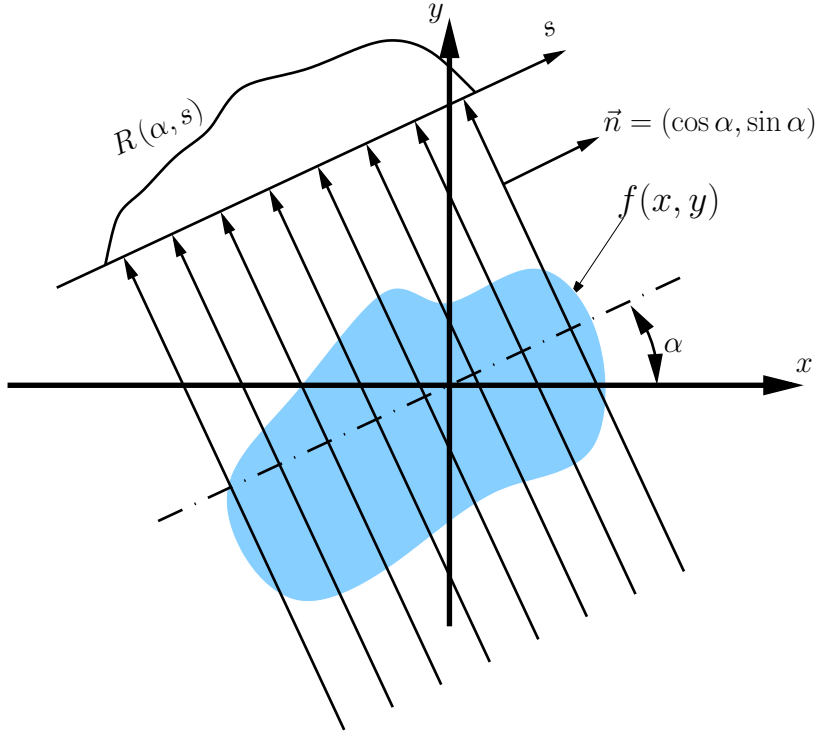


Figure 2.3: Cartoon of the construction of a generic Radon transform. The *MOSES* orders are a special case at three angles,  $-45^\circ, 0^\circ, +45^\circ$ .

### 2.3 Inversion

Inverting the data functions  $I_m$  to recover the image cube  $v$  is clearly an ill-posed problem. The data functions represent  $3N$  pieces of information while the cube contains (approximately)  $NM$ , where  $N$  and  $M$  are the number of  $x$  and  $\lambda$  pixels respectively. As a result there are an infinite number of cubes which can accommodate the data. Compounding this problem, the data functions do not sample precisely the same sections of the cube. As figure 2.2 shows, some sections are sampled by only 1 or 2 lines of sight.

We deal with these issues by taking advantage of prior information and careful instrument design choices. As shown by Kankelborg & Thomas (2001), the *MOSES* nullspace is filled by things which contain negative intensity. The instrument passband has been chosen to be narrow enough that only two spectral lines are contained therein. Because the solar spectrum is sparse in our passband many cubes which fit the data contain nullspace elements with negative intensities in places where there are very few photons. These can be eliminated by positivity constraints.

To deal with the effects of sampling at the edges, we only attempt to reconstruct the part of the cube sampled by two or more orders. The design of the instrument further diminishes the effect of this ambiguity by making the  $x$  direction much longer than the  $\lambda$  direction ( $N \gg M$ ). *MOSES* has  $N = 2048$   $x$ -pixels but only  $M \sim 64$   $\lambda$ -pixels.

With simulated *MOSES* data, we have found it possible to locate the line center by cross-correlation of the three observed orders. When the orders are coaligned (see § 5.2.1 on page 83) the He II spectral line will be in the center of the cube.

We also have a great deal of information about the spectral lines in our passband. Prior experiments have shown that these lines can be well represented by gaussian

profiles (Andretta et al., 2000), have established their average integrated linewidths, and have measured the separation of the line centers (Brosius et al., 1998). We implement this complex prior knowledge by assuming that we know the integrated spectrum or “infinite” order projection (the line-of-sight looking into the cube from the side, at 90°). We thus add an “inferred projection” to our three measured projections for a total of 3+1 orders. This “infinite order heuristic” is a key to solving the *MOSES* inversion problem. The performance of all inversion algorithms that we have investigated significantly deteriorates when it is left out.

Discussion of the results of trial inversions of simulated data, by three different reconstruction techniques and the first inversion of *MOSES* flight data is deferred to chapter 6 on page 110.

## CHAPTER 3

### THE *MOSES* ROCKET

The Multi-Order Solar EUV Spectrograph (*MOSES*) rocket is a novel multi-order slitless imaging spectrometer. *MOSES* provides high spatial resolution ( $0''.6$  pixels), high cadence ( $< 10$  s), wide field of view ( $10' \times 20'$ ) images in a narrow EUV spectral band around  $304\text{ \AA}$ . Images are recorded at three spectral orders  $m = +1, 0, -1$ , allowing simultaneous imaging and spectroscopy.

#### 3.1 Optics

The optical configuration of *MOSES* is illustrated in figure 3.1. The primary mirror is a concave spherical diffraction grating operated 1 degree off axis, with focal length  $4.74\text{ m}$ , and  $8\text{ cm}$  square clear aperture ( $f/59$ ) with a pitch of  $950$  lines/mm, giving a reciprocal dispersion of  $29\text{ m\AA}$  ( $29.6\text{ km s}^{-1}$ ) per pixel at  $304\text{ \AA}$ . The pixel subtent in this optical system is  $0''.6$  or  $440\text{ km/pixel}$  on the Sun. The design was ray traced and optimized by Roger J. Thomas at Goddard Space Flight Center (GSFC) (Thomas & Kankelborg, 2001). The major optical elements are shown in figure 3.1. Thin film aluminum filters (not shown) cover the open end of each detector housing to make a light tight box. The optical characteristics are summarized for reference in table 3.1 and the optical prescription from Dr. Thomas' design is given in table 3.2.

The grating flown on *MOSES* is a Zerodur substrate with laminar rulings fabricated by Carl Zeiss Laser Optics (Owens et al., 2005). Precise control of the groove depth allows an optimal distribution of light in the three central spectral orders, where our detectors are placed; nearly all of the reflected light goes into those three orders. The fold flat is Ultra-Low Expansion (ULE) glass with a protected aluminum

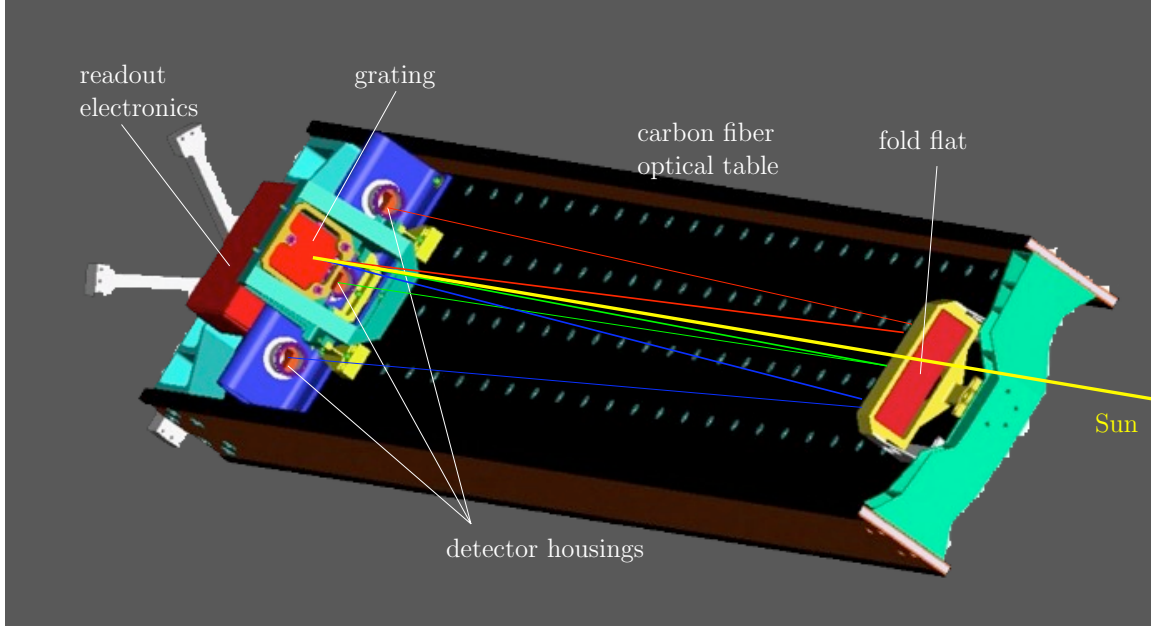


Figure 3.1: Layout of the *MOSES* instrument. Not shown are the baffles, filter tubes, front aperture plate, shutter and LN2 plumbing. Most of the payload electronics are on the opposite side of the optical table. The colored lines show principal optical rays. The yellow ray comes from the Sun. The red, green, and blue rays show the path of light going to the  $m = +1$ ,  $m = 0$ , and  $m = -1$  orders respectively.

coating on the reverse side for instrument alignment. Multilayer  $B_4C/Mg_2Si$  coatings were applied to the gratings and fold flat at GSFC. The coatings provide a high reflectivity ( $\approx 0.4$ ), narrow passband peaked at 304 Å. The band contains two strong solar emission lines: He II 303.8 Å and Si XI 303.3 Å. Nearby contaminant lines at 284 Å and 335 Å are suppressed by factors of 92.7 and 223.4 in  $m = +1$ , 98.6 and 51.0 in  $m = 0$ , and 76.4 and 137.7 in  $m = -1$  respectively (see Owens et al., 2005, table 2a and 2b).

### 3.1.1 LOTS

The optics are mounted on the Lockheed Optical Table System (LOTS) developed by Marilyn Bruner at Lockheed-Martin Solar-Astrophysics Laboratory for the Solar

Table 3.1: Optical Characteristics.

Focal length	4.74 m
Aperture	8 cm square ( $f/59$ )
Pixel subtent	0''.59, 29 mÅ, 29 km/s , 440 km
FOV	20' × 10'
Grating	9.48 m sphere, 950 lines/mm
Coatings	B <sub>4</sub> C/Mg <sub>2</sub> Si multilayer, Reflectivity ∼ 0.4 , $\lambda$ 304 Å
Filters	1500 Å Al on Ni mesh, 38 mm diameter
	1 each at $m = \pm 1$ , 2 at $m = 0$ .
Lines	He II 303.8 Å, Si XI 303.3 Å

Table 3.2: Optical Prescription. All linear measures are given in millimeters. All angular measures are given in degrees. Optical element positions are referenced to the geometric center of the element. The *MOSES* coordinate system is used in the optical prescription. It is defined by an origin at the center of the  $m = 0$  order detector, with the  $X$  axis pointing toward the Sun, the  $Z$  axis pointing away from the table on the optics side (“up” in fig. 3.1), and the  $Y$  axis completing the right-handed triad. Pitch and yaw angles are given in a right-handed sense about the  $Y$  and  $Z$  axes, respectively. The third angle, roll about the  $X$  axis, is not used in the optical prescription; all optical elements have a roll of 0°.

Item	Surface	Width	Height	X	Y	Z	Pitch	Yaw
Pupil	Flat	94.0	87.0	2518.7	0.0	78.5	0.000	0.000
Stop	Flat	80.0	80.0	118.7	0.0	78.5	+0.973	0.000
Grating	R=9480	90.0	90.0	118.7	0.0	78.5	+0.973	0.000
Folding	Flat	192.6	50.0	2428.6	0.0	0.0	+0.973	0.000
Det(+1)	Flat	28.0	14.0	3.0	-136.7	0.0	-0.011	+2.463
Det( 0)	Flat	28.0	14.0	0.0	0.0	0.0	-0.004	0.000
Det(-1)	Flat	28.0	14.0	3.0	+136.7	0.0	-0.011	-2.463

Plasma Diagnostics Spectrometer mission (Bruner et al., 1989). It flew twice, 1992 May 12, and 1994 April 25. The LOTS table, along with its rocket skins, electrical feedthrough connectors, and H- $\alpha$  guide telescope which were retained for *MOSES*,

provides flight heritage through these reusable components. The LOTS system is a very stable, strong, lightweight, low thermal-expansion structure capable of space-flight but with all the advantages of an optical test bench.

The LOTS table is made of carbon fiber composite face sheets bonded to an aluminum honeycomb core with an I beam structure. The carbon fiber sheets are layed up in such a way that thermal expansion in the long axis of the bench is cancelled, resulting in nearly zero coefficient of thermal expansion in that direction. A grid of threaded metal inserts on 4 inch centers is fitted on both sides of the table. The tops of the inserts are machined coplanar and precision cylindrical counterbores are machined along the axis to provide for 1/4"-28 shoulder bolts. Together these provide repeatability of optical element positioning. Parts can be removed and replaced during integration and testing with confidence that they will return to the same location. LOTS is attached inside the rocket skins by aluminum fittings at each end. At one end a steel shaft and spherical bearing assembly are attached to the skin by an aluminum "spider". These provide support for lateral and thrust loads. The spherical bearing absorbs bending moments. At the other end the table is supported by a steel diaphragm bolted to the skins along its perimeter. This diaphragm, doubling as an aperture plate, supports LOTS laterally and in torsion. Strain along the long axis of the table due to thermal expansion of the rocket skins during flight is absorbed by the flexure of this diaphragm. The overall design provides a securely mounted yet isolated optical platform. The table itself does not change due to environmental factors, and external loads placed on the skin are not transmitted to the table. The layout of the optics and detectors on LOTS is shown in figure 3.1. The full payload assembly drawings, with skins removed, showing both sides of LOTS, and all components except for liquid nitrogen plumbing are shown in figure 3.2.

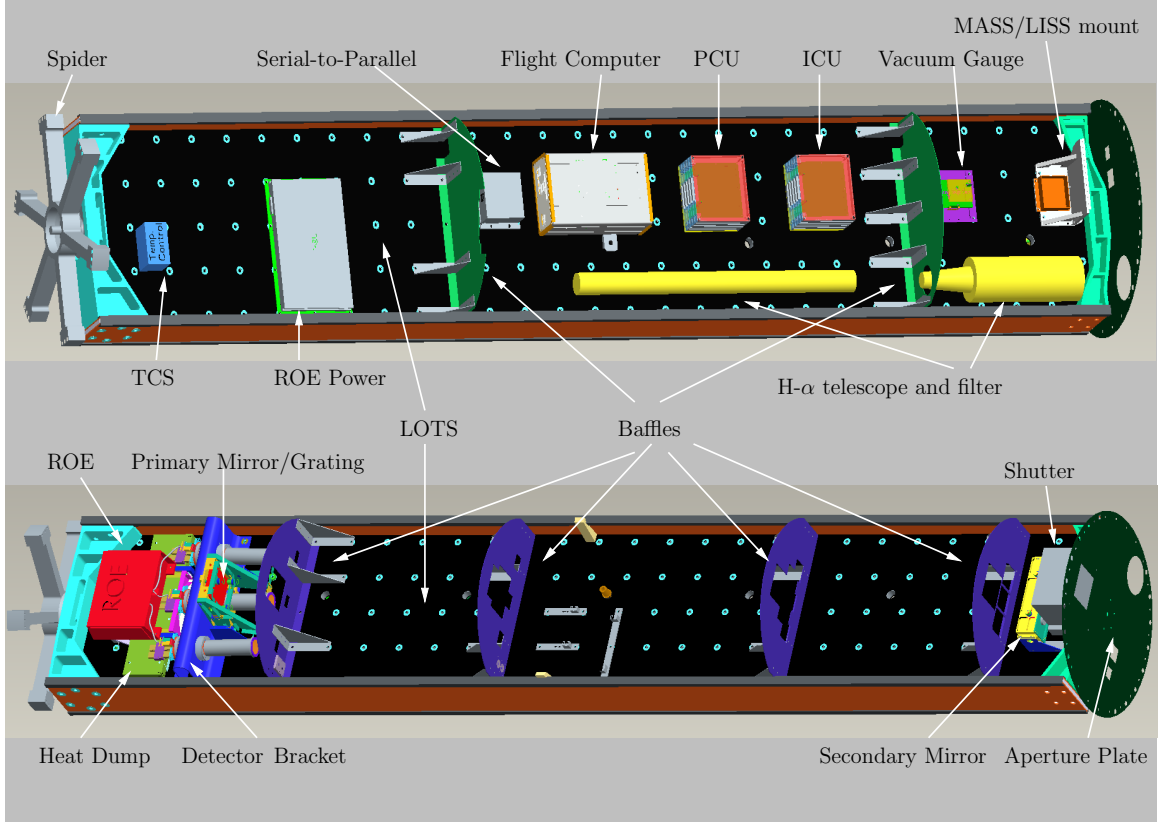


Figure 3.2: The full *MOSES* assembly. A view of the optical side is shown at bottom. The electronics side is shown at top. All major components are labeled. The LN2 plumbing and electrical harnesses are not shown.

### 3.1.2 Detectors

The detectors are three  $2048 \times 1024$ , rear-illuminated E2V CCD42-20 devices at spectral orders  $m = +1, 0, -1$ . The readout electronics (ROE) are a three-channel variant of the *Hinode*/EIS system, contributed by Mullard Space Science Laboratory (MSSL). The power supply is also a copy of the corresponding EIS system (Kosugi et al., 2007; Culhane et al., 2007). Thermoelectric coolers (TECs) regulate CCD temperature to  $-30^\circ\text{C}$ . An aluminum block, kept cold with liquid nitrogen (LN2) until launch, is the heat dump for the thermal control system (TCS) (see §3.3.5).

Invar plates, on which the CCD's are mounted by E2V, are coupled at the back to copper “cold fingers”, which are actively cooled, and coupled at the front to black anodized aluminum shielding tubes. The tubes provide stray light rejection, and feature a rectangular cut-out at the front, just large enough to prevent vignetting without allowing stray light input. The tubes are directly attached to the “cold finger” at a flange, and achieve thermal equilibrium at the  $-30^{\circ}\text{C}$  control temperature of the CCD's, and thus provide thermal isolation to the detectors which see an immediate thermal environment in equilibrium with themselves. The plates and shield are inserted through a thin-walled titanium outer housing, and only touch it at the back. The complete detector housings are cantilevered from the opposite end of the titanium outer housing in a carbon fiber bracket via aluminum inserts. The titanium outer housing provides a low thermal conduction path to the rest of the payload, reducing thermal input to the detectors from solar heating. The carbon fiber bracket also contributes to the thermal isolation of the system, and provides a stable optical position due to its stiffness and low thermal expansion. The thermal stability of the detectors at  $-30^{\circ}\text{C}$  provides constant dark current at a very low level, essentially unmeasurable for flight exposures. The detector housings and mounting bracket assembly are shown in figure 3.3.

Filter tubes mounted to the front of the detector housings position the thin film  $1500\text{\AA}$  aluminum filters. The metal film filters reject visible light while transmitting about 40% of the EUV light. This is especially important in the  $m = 0$  order, which receives most of the visible solar irradiance from the telescope,  $\sim 1,000,000$  times more intense than the EUV irradiance. Visible light is diffracted at wide angles and low diffraction efficiency in  $m = \pm 1$  orders. Visible light only reaches the  $m = \pm 1$  detectors by scattering. Accordingly, the  $m = 0$  order has two filters, while the outboard orders have 1 each. The design of the grating diffracts about twice as

much EUV light into the central order as the outboard orders to compensate for the extra filter. The length of the filter tubes was carefully chosen to place the filters so as to make the shadow of the Ni support mesh uniform. No residual pattern from the square mesh is seen in *MOSES* images. In figure 3.3 the filter tubes have been shortened for clarity. Their true length is apparent in figure 3.2.

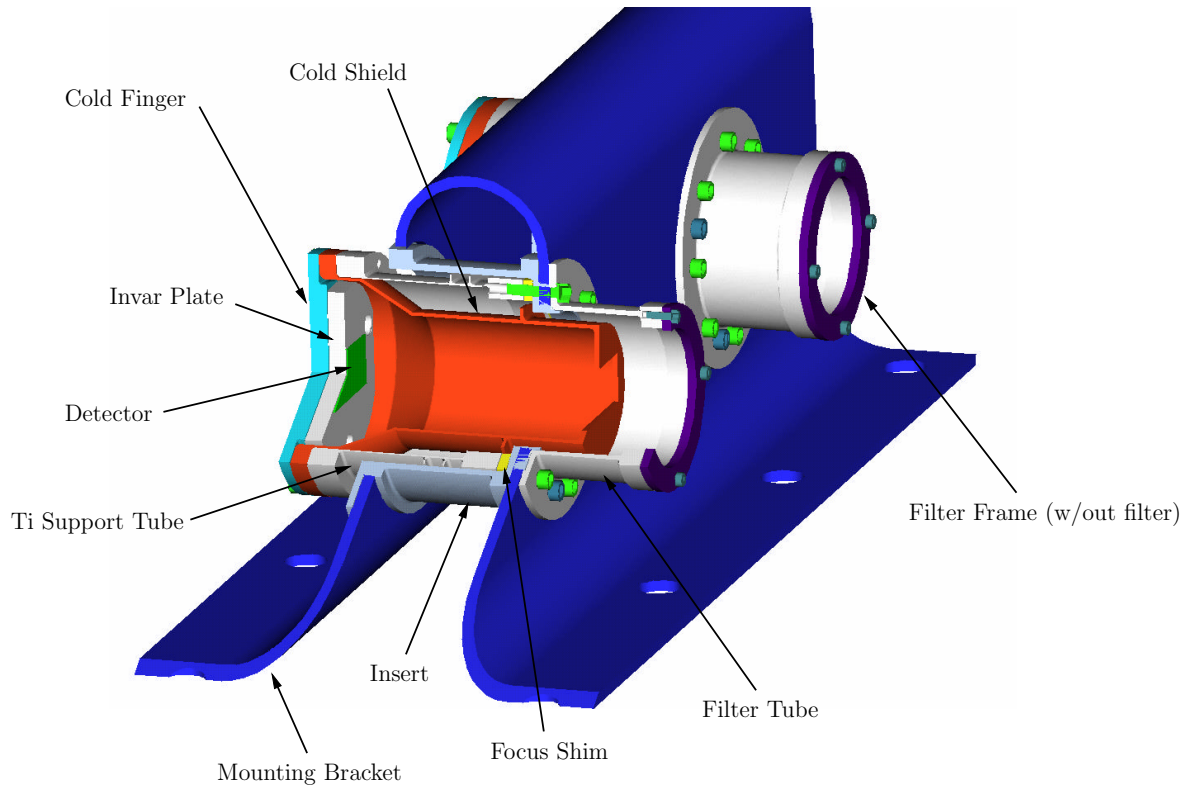


Figure 3.3: *MOSES* detector housings and mounting bracket. The cutaway shows the parts of the detector housing. The connector bracket which brings out the CCD wiring and connector are not shown. The full mounting bracket holds three housings and can be seen in fig. 3.2.

### 3.2 Focusing the *MOSES* Optics

*MOSES* cannot afford the time (or the money) to adjust focus during flight. With only a five minute window for taking data, it must launch in focus, and remain in focus for the duration of the flight. Focus adjustment for *MOSES* is performed on the ground by means of a focus spacer (or shim) inserted in the detector housing between the titanium support tube and the aluminum insert (see fig. 3.3). The spacers for each spectral order are machined to the correct thickness for focus.

Precise measurement of focus was surprisingly difficult due to the very large focal length of the *MOSES* primary mirror (see table 3.1). Multiple measurements of the grating radius of curvature were performed at Goddard Space Flight Center and at MSU, accurate to a few mm, or  $\sim 0.02\%$ , but this is not accurate enough for focus (the *MOSES* depth-of-focus is  $\sim 0.8$  mm). *MOSES* was built with focus shim “blanks”, of over-large thickness, and then the instrument was focused at MSU using a collimated light source. The focus experiment gave a length by which to shift the detectors to bring them into focus. The spacers were removed, machined to the correct measured thickness, and replaced, as the final step before shipping *MOSES* to the launch range.

The ideal method of focusing *MOSES* requires an EUV source collimated to  $< 1''$ , which we could observe with *MOSES* and thereby find best focus. However we do not have access to a collimated EUV source of the required quality. We built a collimated visible light source using a green HeNe laser and a 10" Dobsonian telescope with custom figured mirrors (focal length 1250 mm) used in reverse. Laser light is passed through a pinhole (25  $\mu\text{m}$  diameter) placed  $\sim 0.5$  m from a 20 mm Plössl eyepiece. The image of the pinhole was placed at the focus of the telescope, producing a collimated beam. The focus was found by autocollimation: A cube corner retroreflector sends light back down the telescope. When the collimator is in focus this return beam will

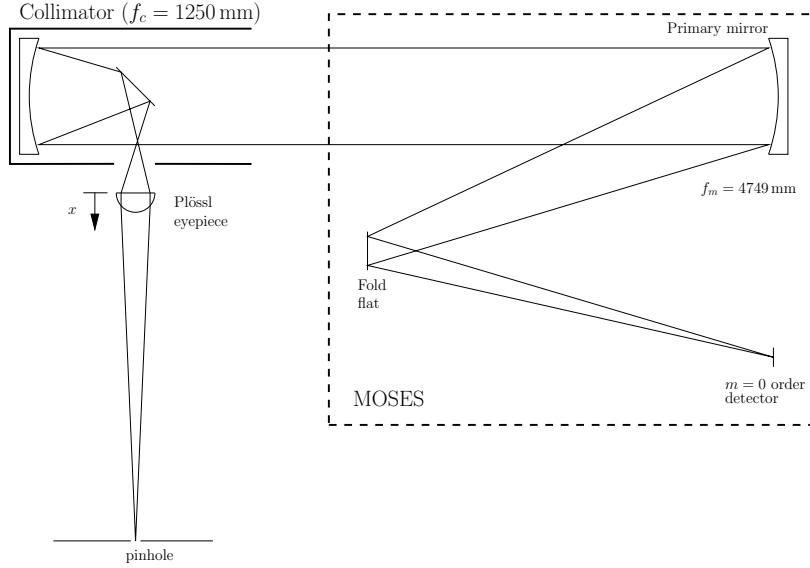


Figure 3.4: Sketch of the focus experiment.

go back through the pinhole again. A beam splitter between the laser and the pinhole picks off the return beam and it is detected by a photodiode. The collimator focus knob is adjusted until the photocurrent from the diode is maximized. Focus position is measured by a precision dial gauge to an accuracy of 0.001 in. Precision in pitch and yaw of the input beam are not essential.

The light from our collimator was used to produce an image on the *MOSES*  $m = 0$  order detector. The experiment setup is diagrammed in figure 3.4. Using visible light prevents us from directly focusing the outboard orders, but the  $m = 0$  focus position will be the same for all wavelengths (although the focus spot will not). After focusing the central order, the outboard orders were adjusted based on the design relative focal positions, see table 3.2.

Beginning with the collimator in focus, data is taken, and then the focus knob of the collimator is adjusted slightly. After each collimator focus adjustment another image is taken. Adjusting the collimator has the effect of moving the image of the

pinhole on the *MOSES* detector in and out of focus. The difference between the eyepiece position at collimator focus and at *MOSES* focus gives the amount by which we must move the detector to place it at the *MOSES* focal length, according to the following equation:

$$\begin{aligned}\Delta a &= f_m - a \\ &= \left(\frac{f_m}{f_c}\right)^2 (X_{det} - X_{col})\end{aligned}\quad (3.1)$$

The focal lengths of the collimator and *MOSES* are given by  $f_c$  and  $f_m$ ;  $X_{col}$  and  $X_{det}$  are the collimator focus adjuster positions at collimation and at best detector focus;  $a$  is the distance from the primary mirror to the  $m = 0$  order detector with the blank shims;  $\Delta a$  is how far we need to move the detector. The sign convention has been chosen so that the quantity  $\Delta a$  represents the necessary change in focus spacer thickness.<sup>1</sup> This equation is valid close to collimator focus, compared to the focal length of the Plössl eyepiece.

The focus experiment was performed 2005 July 6 - 7. My role was to operate the payload, collect the images, and reduce and analyze the data. The intensity of the collimated beam was adjusted by the addition of neutral density filters between the laser and the pinhole, so that the focus spot would be bright compared to the dark current, but not saturated. 40 positions were used, with a 0.2 s exposure time at each location. Our best estimate of collimator focus was  $X_{col} = 0.5848$  in.

I dark-subtracted and fit the data with 2-D elliptical gaussian functions. Figures 3.5 and 3.6 show the through-focus series of spot images and fits. Figure 3.7 graphs

---

<sup>1</sup>We found it convenient to move the detectors, but one could also consider moving the primary or secondary mirror or a combination of all three;  $\Delta a$  is the required change in optical path length between the primary and the detector. In mirror terms,  $-\Delta a$  is the amount by which to move the primary (in the  $+X$  directions), or  $\Delta a/2$  is the amount by which to move the secondary.

spot size parameters against focus position. It is clear from the focus spots that the optics are not diffraction limited. See appendix C for a discussion of instrument aberrations.

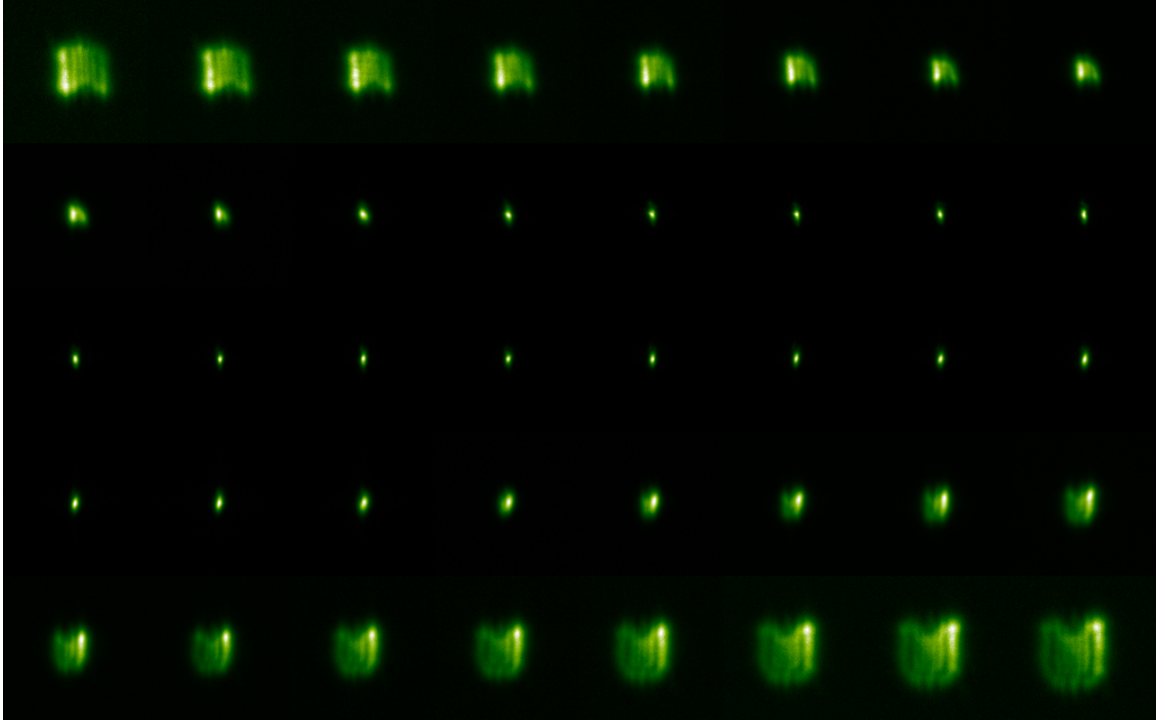


Figure 3.5: Focus spot series, through focus. The spot images are 128 pixel squares. Images have been normalized to the same peak intensity, else out-of-focus spots would not be visible. The appearance of a background in the out-of-focus spots is an indication of their peak brightness relative to the background. The image closest to our estimate of best focus is in the 1<sup>st</sup> column, 3<sup>rd</sup> row.

We use spot area (the product of semi-major and semi-minor axes) as a metric for determining best focus. Our estimate of best focus is obtained by bootstrapping – randomly resampling the data with replacement – 20,000 6<sup>th</sup> order polynomial fits to the (resampled) spot area data. This procedure generates a distribution of best focus estimates from which we calculate the median estimate and the 99% confidence interval. Our best focus estimate is  $X_{det} = 0.5647$  in with a 99% confidence interval

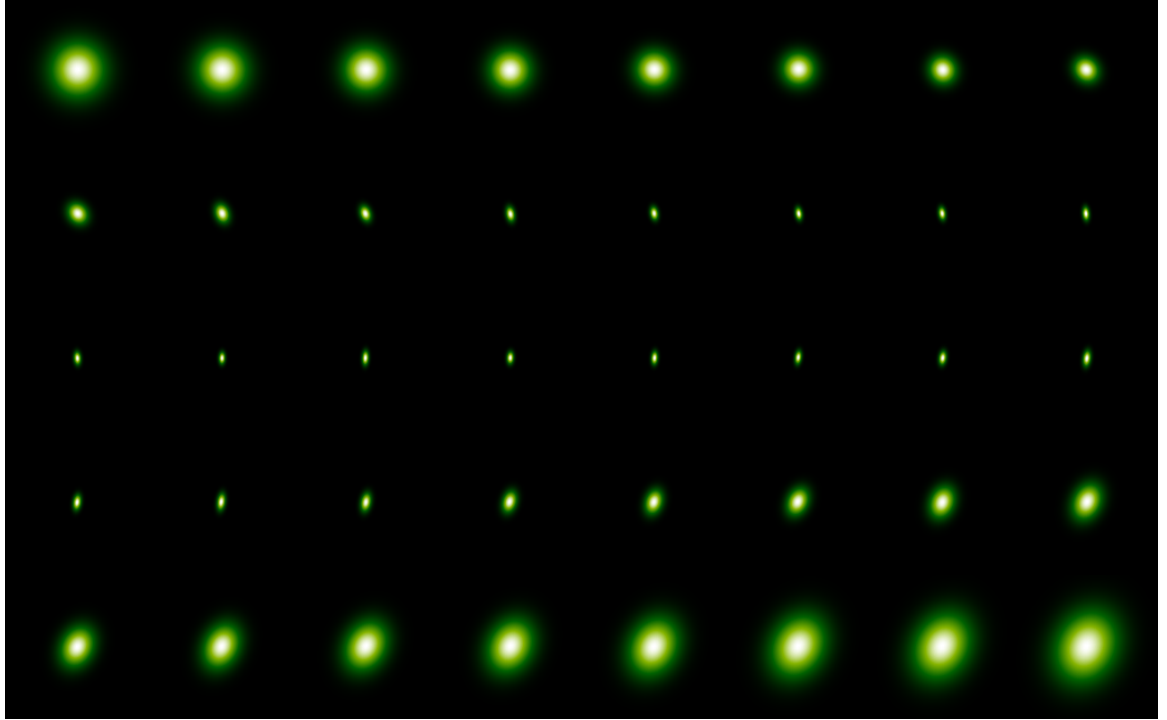


Figure 3.6: Focus spot series fits, through focus. The fit images have been processed in the same manner as in figure 3.5.

of  $0.56250 - 0.56752$  in. The analysis was redone independently by Charles Kankelborg, calculating spot area from the 2nd moment matrix instead of fitting elliptical gaussians. Bootstrapping yielded a best estimate of  $X_{det} = 0.5459$  in with a 99% confidence interval of  $0.56355 - 0.56657$  in. The 99% confidence intervals are 0.128 mm and 0.077 mm wide, respectively, well within the 0.8 mm depth-of-focus of the instrument. We took the average of the two best estimates as the final determination of the best focus position,  $X_{det} = 0.5648$  in. Applying equation 3.1 we find:

$$\Delta a = \left( \frac{4740 \text{ mm}}{1250 \text{ mm}} \right)^2 (0.5648 \text{ in} - 0.5848 \text{ in}) = -0.2876 \text{ in}$$

The focus shims were machined to new thicknesses based on this measurement.

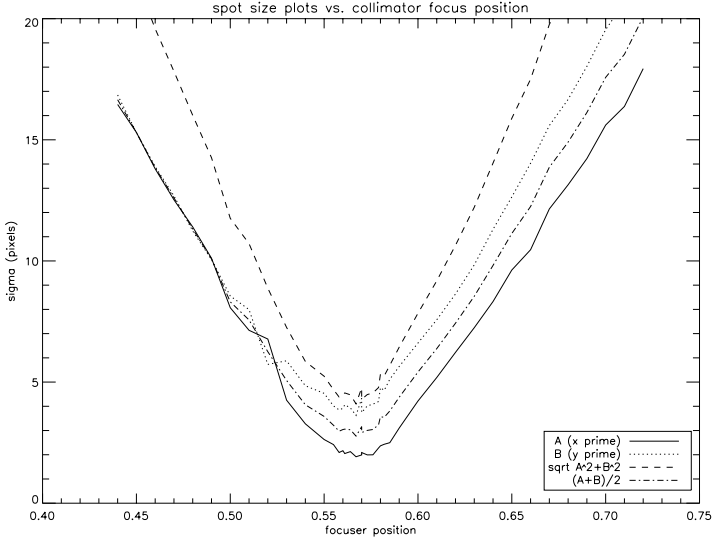


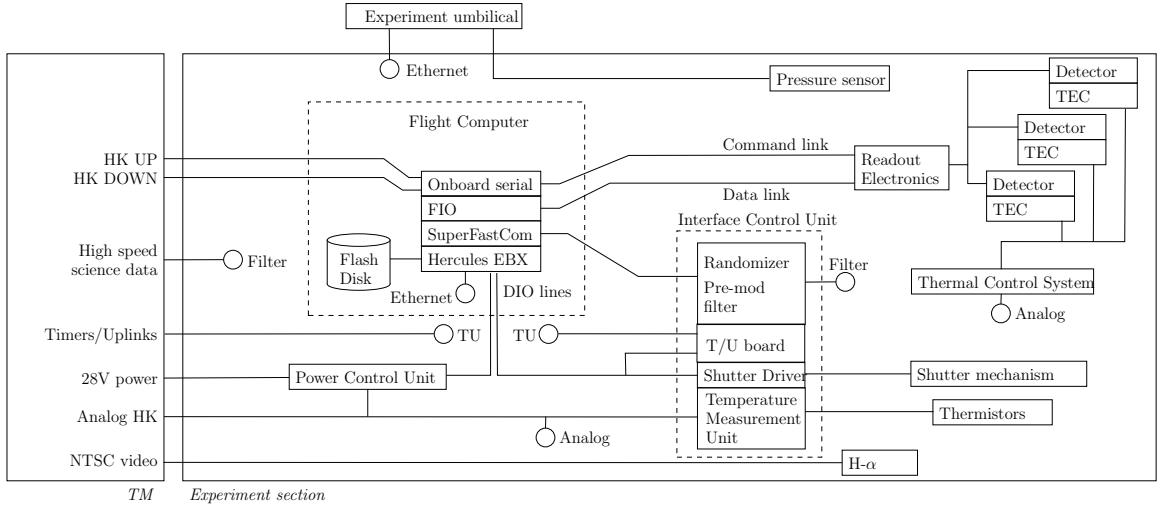
Figure 3.7: Spot size parameters vs. focus position.  $A$  and  $B$  are the gaussian parameters of the ellipse along the  $x$  and  $y$  axes in the rotated reference frame of the spot – equivalently the semi-major or semi-minor axes of the elliptical contour corresponding to  $1/\sqrt{e}$ . Multiply by 2.35 to get the FWHM of the spot. The other two curves, the average and quadrature sum of  $A$  and  $B$ , give a general measure of the overall size of the spots.

### 3.3 Electronics and Software

The electrical systems described in this section can be found labeled in figure 3.2, in the top half of that figure. The payload electronics are a combination of commercial off-the-shelf (COTS) parts and custom circuits and software, designed and built at MSU, by the members of the electronics and software subsystem team, led by the author. This subsystem team consisted, with the exception of the author, entirely of undergraduate students from Electrical Engineering, Computer Engineering, Physics, Mechanical Engineering, and Computer Science departments at Montana State Uni-

versity. Table 3.3 lists these team members and their principal contributions to the *MOSES* mission.

The *MOSES* electronics flight system is oriented around the needs of the ROE. Extensive isolation is employed in our electronics to ensure electrical noise does not contaminate data during the sensitive CCD read-out process. The ROE is grounded close to the CCDs and all electronics which interface to it are isolated to avoid creating ground loops. Both the ROE power supply (designed and built at MSSL) and the flight computer power supply are isolating DC-DC converters. The computer is almost completely isolated in all of its interfaces. The isolation barrier was violated only at the RS-232 serial communication ports, which allow communication between the computer and the ground during flight. It is likely that these connections are between high impedance serial transceivers, so current on the signal ground should be low. The *MOSES* overall electronics design is described graphically in the *MOSES* electrical block diagram, figure 3.8, and the grounding and isolation diagram, figure 3.9.



Date	Initials	Project:	MOSES Sounding Rocket
2005-12-26	CCK (drawn)	Title:	SIMPLIFIED ELECTRONICS BLOCK DIAGRAM
2011-03-11	JLF (updated)	Dwg no.:	MSU-MOSES2-0001 Rev B

Figure 3.8: Electronics system block diagram.

Table 3.3: Electronics and Software subsystem team members.

Lindsey Nussbaum	TCS
Avon Whitworth	TCS, Power input stage, VI sensing, Vacuum gauge
Sean Kirn	Premod filter
Hans Courier	H- $\alpha$ electronics, Electrical harness, Integration & Testing
Grant Turner	TCS, Lab electronics, EGSE, Electronics system design
Chris McIntosh	Power switching, TMU, Integration & Test
Rich Parker	Flight computer cooling, Vacuum gauge
Wayne Janssen	TCS, PCU cooling
Cameron Chen	Power converter stage, PCU cooling
Brandon Anderson	EGSE, Electrical harness
Colin Shirley	FPGA programming, TU interface board
Haeseon Yun	Shutter driver
Wesley Brooks	Flight Computer ROE interface
Reggie Mead	Flight software
Ehson Mosleh	EGSE software
Michael Tucker	Serial programming, Interface programming
Calvin Coopmans	Serial programming

### 3.3.1 Interfaces

My vantage as electronics subsystem lead resulted in my becoming the most knowledgeable person about the *MOSES* electrical system as a whole. Coupled with my duties as *MOSES* system engineer, I became the natural person to design, specify, and maintain all electrical interfaces, particularly those between our systems and NASA's. Some words about the structure of the NASA Sounding Rocket Program are in order here.

3.3.1.1 NASA Interface: The Sounding Rocket Program provides a platform for experimenters to test and fly their instruments with a minimum of complications. They provide launch and integration services as well as many of the spacecraft systems that all payloads need, such as attitude control, power, guidance, telemetry, and

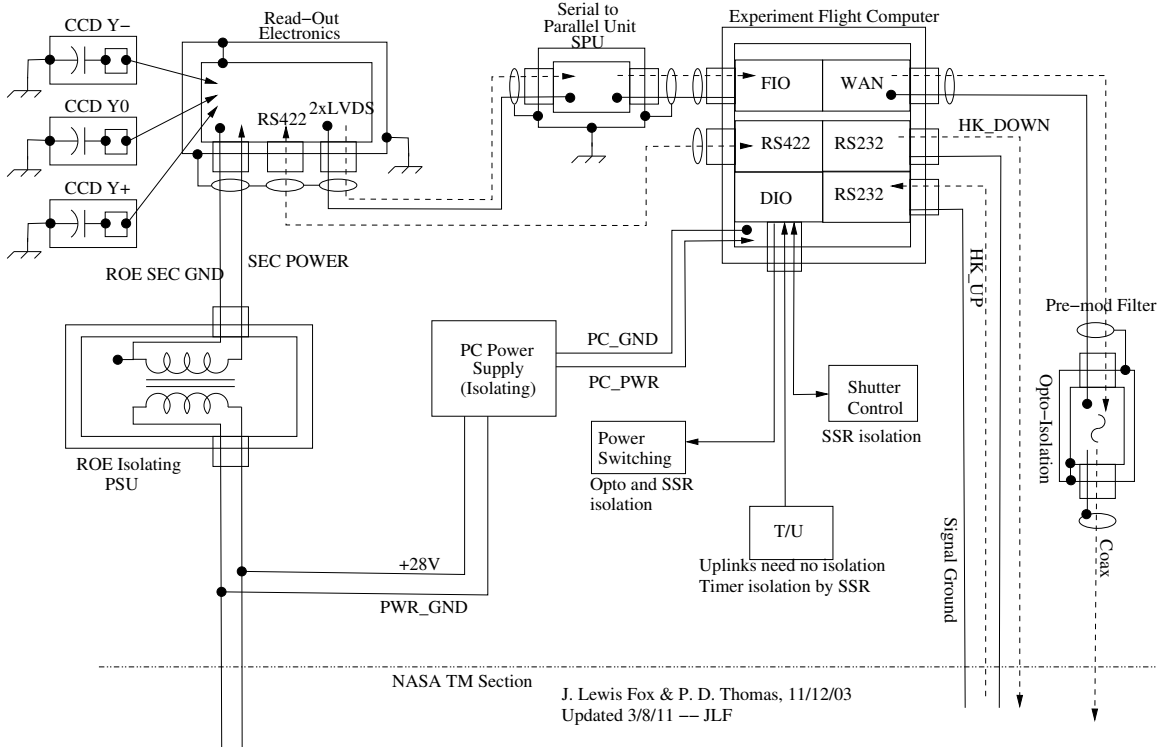


Figure 3.9: Grounding and isolation scheme. The ROE, CCD's, and flight computer are all behind an isolation barrier. Isolation is maintained by opto-isolation or solid state relays (SSRs) everywhere the computer interacts with the rest of the payload, except for the RS-232 HK links. Ellipses represent cable shields. Solid/dashed line pairs represent signal grounds and associated signals, respectively.

power. In the world of small satellite missions what they provide might be called the “system buss”. Doing this relieves the experimenters of the necessity of designing their own systems to provide these functions. NASA has designed, and maintains and upgrades, many standard modular systems that are available to experimenters on request. A sounding rocket payload is divided into functional blocks, or “sections” – Experiment section, Telemetry (TM) section, Guidance, Attitude Control System (ACS), recovery, etc. The Experiment section is provided by the scientist, and must interface to the NASA provided sections.

Working with NASA TM section electrical engineers John Aasen and Jim Diehl, I designed the *MOSES* electrical system interface, and specified it in a design document: the *Experiment Telemetry & Electrical Interface* section in the *Design Review Experimenter's Data Package*, included as a part of the *MOSES* Design Review Document. This document is included as supplemental material on the CD (see B.1).

The electrical interface specifies the components required in the TM section, the timing of digital and analog signals, the voltages and currents required, and the method for transferring them between sections. *MOSES* is housed in a self-contained vacuum chamber composed of the skin sections and is launched under vacuum for the safety of the instrument (which would otherwise depressurize rapidly during ascent), and to reduce the possibility of molecular and particulate contamination. The *MOSES* electronics systems are housed within the evacuated section, and pass electrical signals to the outside through 5 hermetic connectors, 4 located on the TM bulkhead in the skins beyond the spider, see figure 3.2 on page 21), and one configured as a pull-away umbilical, located on the upper skin section.

NASA provides power, transmitters and receivers, antennae, command uplinks, timers, digital uplink and downlink, MPEG compression, and analog-to-digital (ADC) conversion in their TM section. Solar pointing and attitude control is via the Solar Pointing Attitude Rocket Control System (SPARCS). The SPARCS system requires two NASA provided sun sensors located in the experiment section, these are labeled MASS/LISS in figure 3.2. The signals from these sensors, along with lines for controlling the payload door which opens the experiment to space, are passed back to NASA through the TM bulkhead.

**3.3.1.2 Wiring Harness:** The Flight Harness Specification, which I wrote and is included on the CD (see B.2), gives the pin-out of every connector in the experiment section, and the source and destination of every electrical signal. The flight harness is a major electromechanical component of the instrument. It is the largest and heaviest component *not* shown in figure 3.2 on page 21; cutouts, providing access to the harness, can be seen in the baffles on the electronics side of LOTS, at the top of the diagram, near the table.

### **3.3.2 Flight Computer**

Data handling and experiment control are through a single flight computer, a commercial off-the-shelf (COTS) Diamond Systems Hercules EBX CPU board running a minimal VectorLinux distribution. A PC/104+ stack on the CPU board contains COTS cards for camera data interface and high speed telemetry. The camera data interface is a flexible I/O (FIO) board, from RPA Electronics, interfacing an Altera FPGA to the computer PC/104+ buss. The FIO card received data from a serial-to-parallel unit (SPU), supplied by MSSL, which converts the ROE LVDS signals into a parallel data buss. We programmed the FPGA to interface to the MSSL SPU. All science data are stored onboard in a 1GB flash disk. During flight as much science data as possible are sent to the high speed science link (HSL), a  $10 \text{ Mbit s}^{-1}$  transmitter. The telemetry interface card is a Commtech Superfastcom WAN board. Serial uplink and downlink channels allow two-way communication with the experiment computer through onboard RS-232 ports. The computer controls the exposure sequence through a camera control RS-422 serial link to the MSSL supplied read-out electronics. Shutter control is via the computer's Digital Input/Output (DIO) port, which signals an isolating shutter control circuit (§3.3.4.2). The computer also uses the DIO port to control the power-up/power-down sequence through the power

switching board (§3.3.3), and responds on the DIO port to uplink relay and timer inputs from the Timer-Uplink (TU) interface board (§3.3.4).

### 3.3.3 Power Control Unit (PCU)

The PCU contains four custom boards: the power converter board, the power switching board, the analog voltage and current measurement unit (hereafter called the VI board), and the power input stage.

The power converter board contains three COTS DC-DC converter units and an input filter, all from Interpoint, along with the necessary circuitry to properly condition the devices. The converters are thermally coupled to a metal chassis containing a sealed phase change medium. The chassis and phase change material provide a thermal reservoir with sufficient capacity to cool the power converters during pre-flight and flight operations.

The power switching board provides isolated power switching capability to the computer. It responds to computer signals on the DIO port, isolates them via optocouplers or solid state relays, and performs the switching function for almost all experiment electronics. Only the flight computer, its 12 VDC power supply, and the power input stage are not controlled through this board. The flight computer has its own power switch, controlled through the TU system; the other systems are always on when connected to external power.

The VI board measures power currents and voltages and scales them to the 0–5 V range for NASA supplied Analog-Digital Converters (ADCs) in the TM section. It is part of the analog housekeeping subsystem, along with the Temperature Measurement Unit and the onboard housekeeping functions of the TCS unit. This subsystem permits monitoring of instrument status and health from the ground.

The power input stage provides over-current, over-voltage, and under-voltage protection, power filtering (in addition to the input filter in the power converter board), and an emergency power shut-off switch. When triggered, the over-current protection shuts off all experiment power for 100 ms and then attempts to turn it back on. If the over-current triggers again, the process repeats. Because all power switching board functions default to the “off” position on start-up, the system has a high degree of fault tolerance.

### 3.3.4 Interface Control Unit (ICU)

The ICU contains four custom circuits; they supply “interfaces” between our systems and the NASA telemetry (TM) section, or between the flight computer and something it must be isolated from (e.g. the shutter). These boards are: the pre-modulation filter (PMF), the temperature measurement unit (TMU), the timer/u-plink interface unit (TU), and the shutter driver.

The premodulation filter accepts digital telemetry data from the computer WAN card, and drives the HSL transmitter in the TM section. The PMF filters the square wave input before the data is used to modulate the carrier. This prevents the formation of harmonic sidebands, due to the high frequency content of a square wave signal, which could cause the transmitter to run afoul of bandwidth limits imposed in the launch area. The PMF isolates the digital TM signal through opto-isolation, and then processes it using active filters powered by non-isolating DC supplies which are grounded to the transmitter. It also implements a standard pseudo-randomizer circuit which ensures that any data stream presented to the PMF produces a filtered output which contains sufficient transition edges (from “1” to “0” or “0” to “1”) to allow telemetry bit synchronizers to “lock on” to the telemetry stream and reconstruct the HSL data.

The TMU board receives temperature data, measured by thermistors, from all over the *MOSES* payload. Many of the temperature signals monitor CCD cooling chain temperatures to validate TCS function (see §3.3.5). Others monitor the temperature of electrical components to watch for overheating while operating in vacuum. The TMU conditions and scales the temperature signals before sending them to the analog deck in the TM section where the signals are digitized and transmitted to the ground.

**3.3.4.1 Timers and Uplinks:** The TU interface board transforms timer and uplink inputs from the NASA TM section into output the flight computer can understand. The NASA timer deck connects the experiment battery voltage to the appropriate timer input line according to the predetermined timeline program. These signals alert the flight computer that it is time to perform the requested functions, such as beginning an exposure sequence. In order to maintain the computer isolation barrier, the timer signals from NASA are used to switch Solid State Relays (SSRs) which connect a 5 V computer supply voltage to ground through a pull-up resistor. The DIO port timer lines are held at 5 V through these pull-ups. A transition from a “1” to a “0” on a line activates the associated timer function. The NASA uplink inputs are simply the two contacts of an electromechanical relay; as such, the uplinks are isolated before they reach the TU board. The relay is activated upon receipt of an uplink command from the ground. The TU board interfaces these relay contacts to the DIO port so that they function identically to the timers. A transition from “1” to “0” triggers the appropriate uplink function. All timer signals are redundantly implemented as uplinks, in case of failure of the timer deck. Additional uplinks are used for functions needed during integration and test activities on the ground. The flight computer power switch is also connected to an uplink.

**3.3.4.2 Shutter:** The *MOSES* shutter is an aperture mounted, bi-stable, balanced, mechanical system, actuated by two rotary solenoids. The rotary solenoids draw power from the main experiment buss (28 V), and require large currents for a brief, 50 – 150 ms, period while the shutter changes state. The shutter driver circuit allows the computer to control this mechanism without violating the isolation barrier (see fig. 3.9). 28 VDC main power is switched through two SSRs; the relay control lines come from the computer’s DIO port. In addition an optical state sensor provides a digital signal indicating whether the shutter is open or closed. This sensor is powered by a 5 VDC, non-isolating power supply, and passes its output back to the computer’s DIO port through an opto-isolator on the shutter driver board.

### **3.3.5 Thermal Control System (TCS)**

The TCS encompasses all the mechanical and electrical parts which are necessary to operate the CCD detectors at a fixed low temperature of  $-30^{\circ}\text{C}$ . The cold fingers (see figure 3.3) remove heat from the detectors. Thermoelectric coolers pump that heat to backplates which are conductively coupled via copper braid straps to a thermal reservoir in the form of a multilayer-insulated aluminum block. The thermal block is plumbed by copper tubing which carries LN2, chilling the block to a very low temperature. During flight this reservoir continuously warms; the TCS electronics maintain the CCD setpoint temperature. The CCD temperatures are sensed by precision control loop thermistors in the junction between cold finger and Invar plate. The TCS electronics, including TECs, are fully bidirectional, and heat can be pumped in either direction.

The device labeled “TCS” in figure 3.2 is the electronics box which contains the control circuits. Each detector has an independent control circuit driving its TEC, each powered by the TCS power board, for a total of four boards in the unit. The

TCS power board contains a DC-DC converter and three Hall effect current sensors for monitoring the total current through the control circuits. The TCS control circuits are identical PID controllers with bidirectional, continuously variable drive current.

The TCS is fully instrumented. HK thermistors are located on the cold finger, the backplate, and on the thermal reservoir near the point where the conductive braid is attached. A set of cold finger, backplate, and block thermistors constitutes a cooling chain monitor; there are three sets. There is also a thermistor attached to the back of the thermal block farthest from the braid attachment points. Thermistors also monitor the temperatures of the current drivers and the box in the TCS unit. The voltages of both sides of each TEC are also monitored.

The TCS successfully maintained CCD temperatures below  $-30^{\circ}\text{C}$ , with a peak to peak variation of less than  $1^{\circ}\text{C}$ . The exact setpoint varied somewhat from detector to detector due to the precision of the sense thermistors, but all were below the nominal temperature.

### 3.3.6 Thermistor Vacuum Gauge

We use a thermistor vacuum gauge as a pressure sensor. This vacuum sensor is a thermal conductivity gauge, similar in concept to a thermocouple gauge or a Pirani gauge. The control circuit holds the thermistor at a fixed temperature. The voltage necessary to maintain this temperature is an indirect measure of the pressure in the payload skins. The gauge is usable in the range of 5 – 1000 mTorr. It was powered and read-out through the payload umbilical, and so does not provide data during flight. It was used to verify internal payload vacuum was in the safe range for the thin-film filters ( $< 1$  Torr). Precision, absolute accuracy, and response time are not critical in this application. We only require assurance that our vacuum pressure is

below the critical value for launch. After launch, measurement of internal vacuum pressure is unnecessary.

### 3.3.7 Electronic Ground Support Equipment (EGSE)

The *MOSES* experiment EGSE consists of two computers, a datalogger, two regulated, adjustable DC power supplies, one fixed 5 V regulated DC power supply, three decks simulating TM section components, an ethernet hub, two monitors, a keyboard, and a mouse. It is housed in a portable rack-mount cabinet. It was built and programmed by two undergraduate students and myself. It is used to operate the instrument and monitor its behavior. As the lone Test & Measurement engineer I upgraded, modified, and enhanced it through my experience working with it. I also constructed the harness connecting it to the experiment.

The EGSE harness has two pigtail adapters which connect the EGSE connectors to the TM bulkhead connectors and the experiment umbilical. The pigtails are removed when NASA connects their systems. NASA has their own EGSE which returns all the experiment signals in the same form as they are received from the Experiment section, and with the same connectors as those on the EGSE harness. The net result is the *MOSES* EGSE does not know or need to know whether it is connected directly to the instrument or via NASA's TM systems. Flight operation is identical to ground operation. Only the use of the pigtails changes between them.

### 3.3.8 Software

The flight software operates all experiment functions from the single flight computer. It powers on or off all electrical systems, controls the exposure sequence, and responds to mission events and commands delivered from the ground on either the uplink command deck or the uplink serial port. It communicates its status on the

downlink serial port. The EGSE software consists of two components, running on separate computers: The digital housekeeping and control software, which interacts with the flight software on the serial ports, and allows the operator to control the flight computer, and the analog housekeeping software which receives analog housekeeping data from the datalogger and reports it to the operator.

The EGSE digital HK/control software and the flight software must interact efficiently over two slow simplex serial links. The two main software engineers, Reggie Mead and Ehson Mosleh, and I, designed a packet protocol, the Housekeeping Link Protocol (HLP), for this purpose. Efficiency is achieved through packet specialization to *MOSES*. A simple optimal rectangle code (Patel & Hong, 1974) provides error detection (we do not use the single-bit error correction capability of this method). The HLP is documented in the supplemental material on the CD (see B.3).

### 3.4 Calibration

Three calibrations in EUV were performed on the *MOSES* instrument:

1. I measured the *MOSES* detector flat-fields in April 2004, with the help of Roger J. Thomas, Marvin Swartz, and their team at GSFC. The details of that work are given in chapter 4 on page 55.
2. The reflectivity curves of the grating and fold flat were measured at GSFC after multilayer coatings were applied to the optics. The results of those experiments are reported in Owens et al. (2005).
3. End-to-end photometric calibration was performed at Rutherford Appleton Laboratory, Abingdon, UK in March 2005. Results of that calibration will

be reported in detail in a paper, (Rust et al., in preparation), and in brief in this section.

The end-to-end calibration experiment occurred at RAL 2005 Feb 25 to 2005 Mar 18. The calibration was performed by Charles Kankelborg, Mike Chase, Roger J. Thomas, and myself, with assistance from the RAL team, the CDS team, and the support of Physikalisch-Technische Bundesanstalt (PTB – the German equivalent of NIST) who built the calibrated EUV light source. This calibration allows us to convert our detector signal from DN to  $\text{erg}/\text{cm}^2 \cdot \text{sec} \cdot \text{sr}$  entering the aperture, or any other radiometric unit of choice. Performing the calibration before launch allowed us to tune our exposure sequence prior to flight based on realistic expected detector counts, making it more likely our exposure times would be well chosen.

The preliminary results of the absolute radiometric calibration, used to determine flight exposure sequences, have been superseded as of 2009 Dec 23, by a provisional result due to Roger J. Thomas of

$$\begin{aligned} G_{-1} &= 16.02 \pm 1.59 \frac{\text{erg}}{\text{cm}^2\text{sr}} / \text{DN} \\ G_0 &= 34.96 \pm 3.93 \frac{\text{erg}}{\text{cm}^2\text{sr}} / \text{DN} \\ G_{+1} &= 18.27 \pm 2.13 \frac{\text{erg}}{\text{cm}^2\text{sr}} / \text{DN} \end{aligned}$$

These numbers are the most up-to-date available at this time. Multiplying the detected DN by the appropriate  $G$  factor and dividing by the exposure time gives the incident solar intensity in the *MOSES* passband.

One other noteworthy result of the calibration was our discovery that our initial choice of thin-film filter, a tellurium filter sandwiched between a small amount of aluminum for protection, is a great absorber of He II 304 Å light! The design choice for this filter was informed by data from Lawrence-Berkeley Lab's Center for X-Ray

Optics (CXRO), suggesting that tellurium has a strong absorption feature beginning at  $\sim 300\text{ \AA}$  that we anticipated would help reduce contamination of our spectrum by the nearby  $284\text{ \AA}$  line of Fe XV. For many days after we arrived at RAL we could not get the expected signal to our detectors, based on piecewise calibration measurements performed previously. Our signal levels were very low, and were (and still are) making absolute radiometric calibration difficult. While checking and re-checking every aspect of the process we discovered a paper, Schumacher & Hunter (1977), stating that tellurium filters have been used to suppress the He II  $304\text{ \AA}$  line. We removed the filter from the  $m = +1$  order, and replaced it with an aluminum filter and got orders of magnitude more signal. It appears that the calibration of the wavelength scale at CXRO is not precise enough for the purpose we attempted to put it to. The tellurium absorption edge actually begins redward of  $304\text{ \AA}$ .

### 3.5 Range Operations

We first took the *MOSES* instrument to the NASA launch facility at White Sands Missile Range (WSMR) on 2005 July 27, with an initial launch date of 2005 August 23. A variety of difficulties occurred with the instrument, the most serious of which was the destruction of the flight computer mainboard due to short which developed in the power switching board. The root cause of the short was a microscopic copper whisker, a remnant of a board manufacturing defect, which had remained vertical until conformal coating caused it to lie flat and short two traces together. The short caused a 28 V power line to the H- $\alpha$  filter to become connected to the computer DIO port. Turning on the H- $\alpha$  filter, in time, burned out the DIO port, the input side of the power switching board, and the FPGA chip used by the computer to run its boot sequence.



Figure 3.10: The author operating the payload during I&T.

These two boards were replaced (the computer engineering model was used for flight) at the range, but we were unable to make our launch, and returned to MSU, with the instrument, 2005 Aug 29. At MSU a large number of improvements were made, and I accomplished a lot of system level testing. We returned to WSMR 2005 Nov 6, with a launch scheduled 2005 Nov 30. Integration and testing proceeded with fewer problems. By 2005 Nov 27 we had completed shake tests, however our launch slipped due to an anomaly in the SPARCS ACS system during shake. We returned to MSU 2005 Dec 8, but left the experiment section in good working order at the range.



Figure 3.11: Team member with the rocket. From left to right are: Charles C. Kankelborg, Hans Courrier, Rich Parker, the author, Roger J. Thomas, and *MOSES*.

Figure 3.10 shows the EGSE rack with operator at the range. In the background is the console used to point the payload during flight and the uplink command console.

We returned to the range Jan 2006. We actually made it to a launch date, 2006 Jan 31, which was scrubbed during the countdown due to a cooling issue. The issue was resolved a week later, and our next launch attempt, 2006 Feb 8, was a success. Figure 3.11 shows team members with the assembled rocket at the launch rail. The rail is in its horizontal position. One of the building rails and a wheel is visible at lower left. The pad structure rolls away to allow the launch rail to elevate.

I wrote a record of the issues we faced during I & T at the range and their resolutions for the experimenter's package for the Mission Readiness Review, held 2006 Jan 19. It is included on the supplemental CD (see B.4).

### 3.6 Launch and Mission Data

*MOSES* launched from White Sands Missile Range, New Mexico 2006 February 8 at 18:44:01 UT. Approximately 5 minutes of observing time above 160 km resulted in 27 exposures taken in the interval 18:45:54 - 18:50:50 UT. The  $10' \times 20'$  field of view extends from above the East limb to just past disk center.

A movie of the launch is included on the CD (see B.5). Figure 3.12 shows the moment of launch. Both boosters are visible, a Terrier first stage, and a Black Brant VC second stage; together they are referred to as a Black Brant IX.

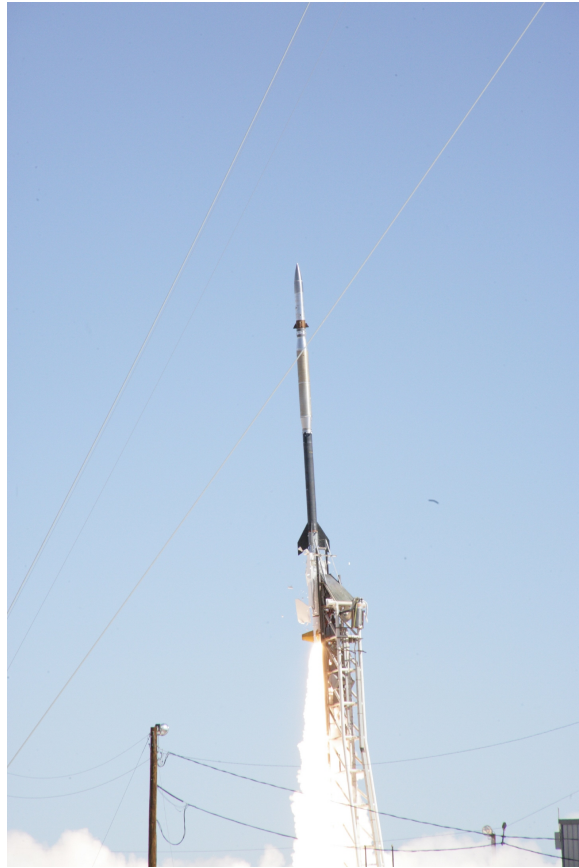


Figure 3.12: *MOSES* leaves the launch rail.

The final payload weight was 1180.2 lbs, including all NASA systems. With a payload length of 322.52 in and a total length (including boosters) of 714.33 in, *MOSES* was the longest payload launched by the Sounding Rocket Program on this vehicle (Black Brant IX), to that date. Predicted apogee was 262.9 km. Actual apogee as modeled by Roger J. Thomas from radar data was 262.84 km.

Table 3.4 is a reproduction of the flight exposure catalog created by Hans Courier from measurements of flight strip chart records of the ROE current. The altitude ranges for each exposure are taken from the analysis of radar data by Roger J. Thomas. There are three dark exposures missing from the end. The last dark sequence was intended to be a 7 exposure sequence. The computer commanded the read-out of the 4th exposure, but stopped responding or sending any data after that. Radar data show that sometime between the end of the 3rd exposure and the end of the 4th, very high acceleration loads were experienced by the payload; this was the beginning of re-entry. Evidently something happened to the electronics during re-entry that prevented the computer from returning from that exposure and continuing with the sequence. After recovery the computer was undamaged, and all flight data were intact. We do not know what caused the anomaly.

### 3.6.1 Data

Solar activity on the day of launch was very low. All of our data are essentially quiet Sun. A Geostationary Operational Environmental Satellite (GOES) A-class flare (A8) occurred just after our flight. With even moderate levels of solar activity A-class flares do not appear in GOES X-ray data because they are below the background. The GOES X-ray flux for 7 hours around our flight is shown in figure 3.13(a), and for the 1 hour around the A8 flare in figure 3.13(b). The remarkably low solar activity during our flight is evident.

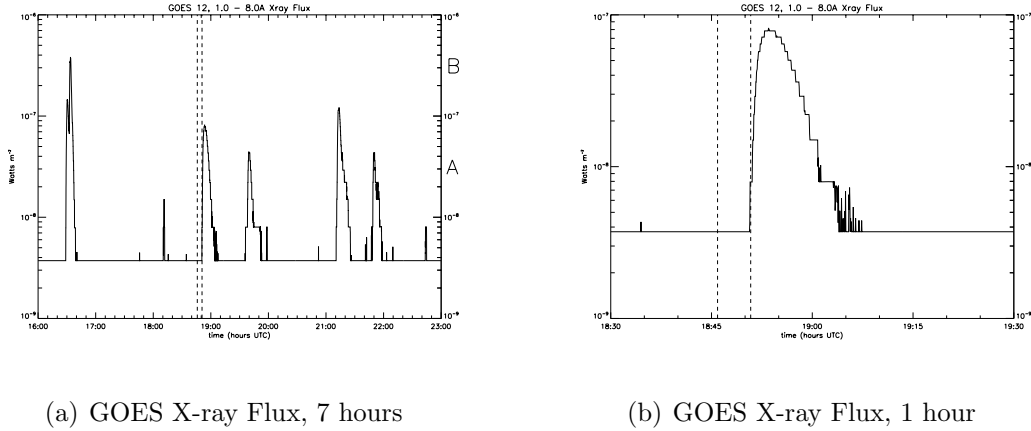


Figure 3.13: GOES X-ray flux in the  $1 - 8 \text{ \AA}$  band for the day of launch. Plot (a) shows a 7 hour time series. Plot (b) shows a 1 hour time series about an A8 flare that began just as our data sequence was ending. In both plots, vertical dashed bars show the begin and end time of the *MOSES* flight sequence.

Displayed in figures 3.14 to 3.21 are examples of flight data that have been normalized and coaligned (see §5.2). Figure 3.14 shows the three spectral orders in one view. Figures 3.15 - 3.21 each show a different exposure length example of  $m = 0$  data. The figures are ordered by exposure time from longest to shortest. One example of each exposure time in the flight sequence is shown. Refer to table 3.4 for information about each frame. A movie of the data frames is on the CD (see B.6). During flight there was a slight pointing drift. The coalignment procedure (§5.2.1) automatically removes it. Bands of pixels on the top or bottom edges with no data are due to this drift.

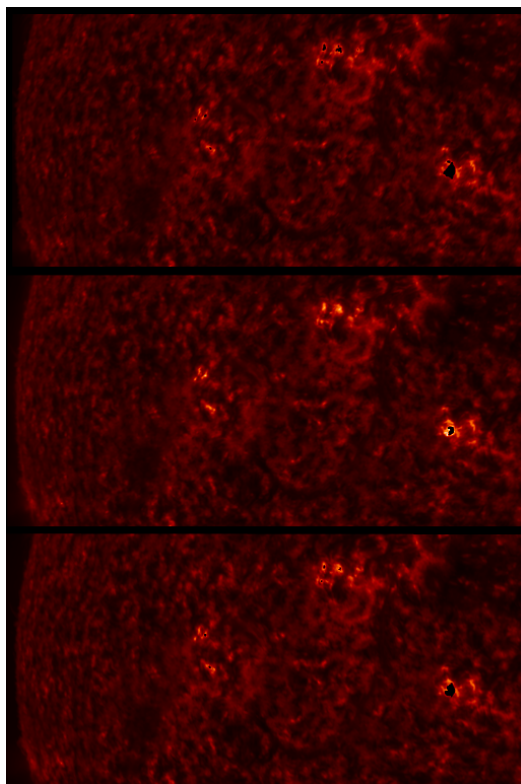


Figure 3.14: Flight data, all three orders. This is a 6 sec image from frame 23. Top is  $m = -1$ , middle is  $m = 0$ , bottom is  $m = +1$ . Regions of zero intensity in this and following figures indicate bad data, either by saturated pixels or pointing drift.

Table 3.4: Catalog of flight exposures. From Hans Courrier and Roger J. Thomas. Exposure start and end times are from strip chart records, and are accurate to  $\pm 0.05$  sec. Heights are from analysis of radar data, accurate to  $\pm 50$  m. Exposure durations are from the on-disk flight computer log.

	Frame #	Start time (UT)	End time (UT)	Length (sec)	Altitude (km)
Dark 1	0	18:05:41.20	18:05:41.45	0.25000	
	1	18:05:47.55	18:05:48.30	0.75000	
	2	18:05:54.30	18:05:55.80	1.50000	
	3	18:06:01.90	18:06:04.96	3.05996	
	4	18:06:10.95	18:06:16.99	6.03978	
	5	18:06:23.50	18:06:35.50	12.00000	
	6	18:06:42.10	18:07:06.10	24.00000	
Dark 2	0	18:45:17.15	18:45:17.40	0.25000	105.21 - 105.64
	1	18:45:23.15	18:45:45.18	22.02993	131.32 - 153.03
Data	0	18:45:54.00	18:45:54.25	0.25000	161.80 - 162.14
	1	18:46:00.30	18:46:01.05	0.75000	170.32 - 171.30
	2	18:46:07.00	18:46:08.50	1.50000	178.84 - 180.69
	3	18:46:14.55	18:46:20.55	6.00000	187.87 - 194.73
	4	18:46:26.70	18:46:38.70	12.00000	201.46 - 213.49
	5	18:46:44.95	18:47:08.99	24.03969	219.19 - 237.97
	6	18:47:15.15	18:47:18.22	3.06981	241.99 - 243.84
	7	18:47:24.40	18:47:27.48	3.07972	247.26 - 248.85
	8	18:47:33.65	18:47:36.75	3.09981	251.76 - 253.11
	9	18:47:42.95	18:47:46.03	3.07982	255.53 - 256.61
	10	18:47:52.20	18:47:55.27	3.06970	258.52 - 259.34
	11	18:48:01.45	18:48:04.45	3.00000	260.71 - 261.26
	12	18:48:10.70	18:48:13.77	3.06974	262.14 - 262.44
	13	18:48:19.95	18:48:23.04	3.08979	262.79 - 262.84
	14	18:48:29.20	18:48:32.28	3.07981	262.67 - 262.46
	15	18:48:38.60	18:48:41.60	3.00000	261.76 - 261.30
	16	18:48:47.85	18:48:50.85	3.00000	260.07 - 259.35
	17	18:48:57.05	18:48:00.14	3.08983	257.65 - 256.66
	18	18:49:06.30	18:49:09.36	3.05984	254.42 - 253.18
	19	18:49:15.50	18:49:18.58	3.07980	250.44 - 248.94
	20	18:49:24.75	18:49:27.84	3.08983	245.70 - 243.94
	21	18:49:34.10	18:49:58.19	24.08973	240.06 - 221.94
	22	18:50:04.35	18:50:16.35	12.00000	216.50 - 204.83
	23	18:50:22.65	18:50:28.65	6.00000	198.06 - 191.37
	24	18:50:35.00	18:50:36.56	1.55980	183.99 - 182.11
	25	18:50:42.75	18:50:43.50	0.75000	174.35 - 173.39
	26	18:50:49.70	18:50:49.95	0.25000	165.34 - 165.01
Dark 3	0	18:51:04.15	18:51:04.40	0.25000	149.65 - 149.28
	1	18:51:10.20	18:51:22.24	12.03986	140.07 - 121.36
Dark 4	0	18:51:30.10	18:51:30.35	0.25000	108.47 - 108.00
	1	18:51:36.15	18:51:36.90	0.75015	97.99 - 96.84
	2	18:51:42.70	18:51:44.20	1.50000	86.44 - 83.71
	3	18:51:50.00	18:51:53.00	3.00000	

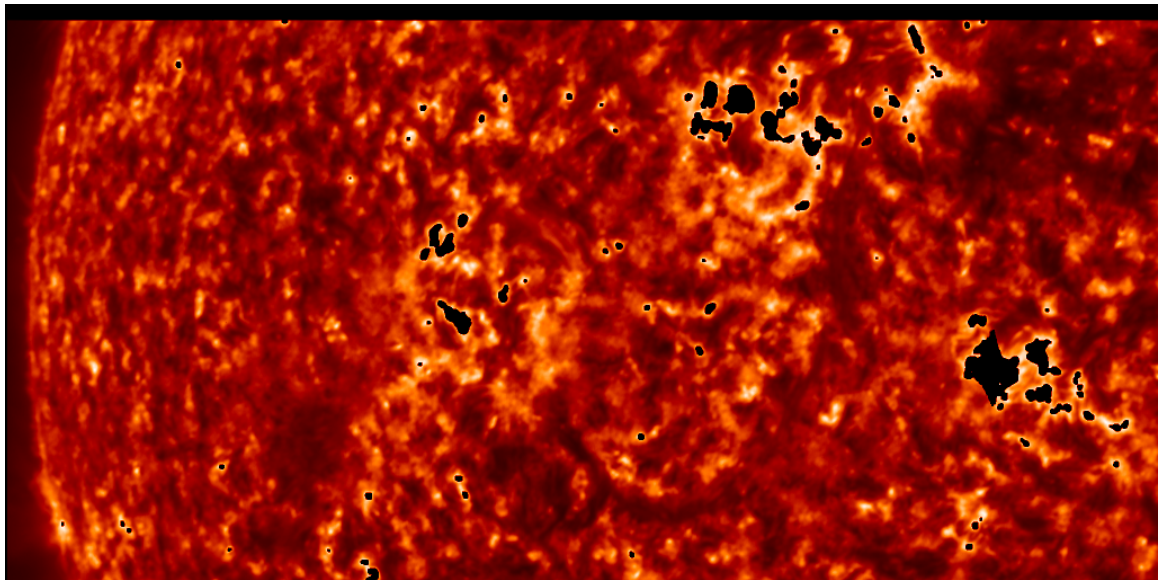


Figure 3.15: Flight data, frame 21.

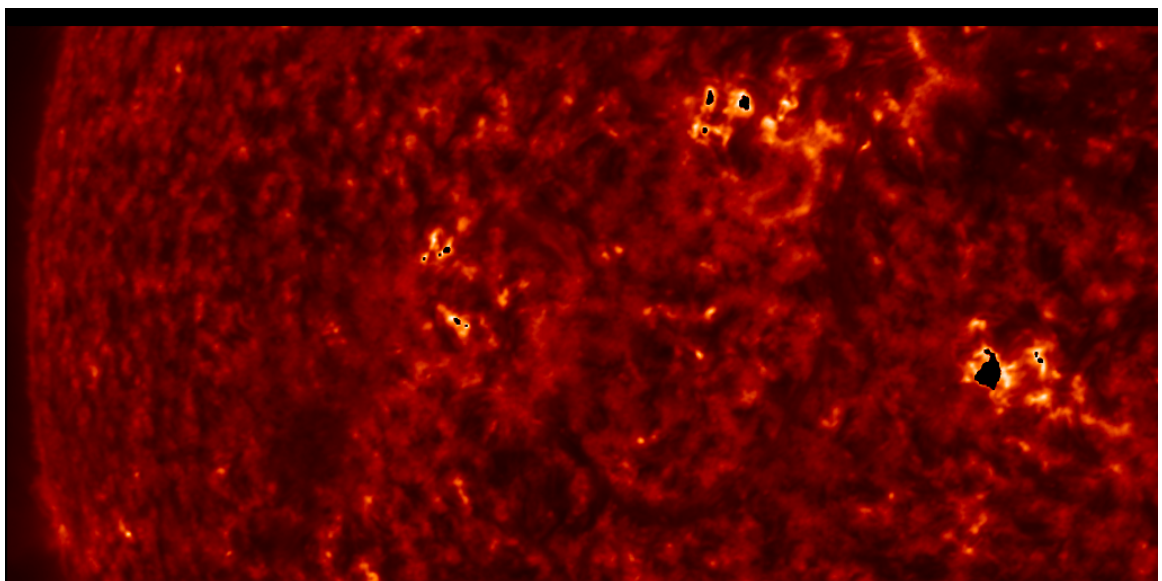


Figure 3.16: Flight data, frame 22.

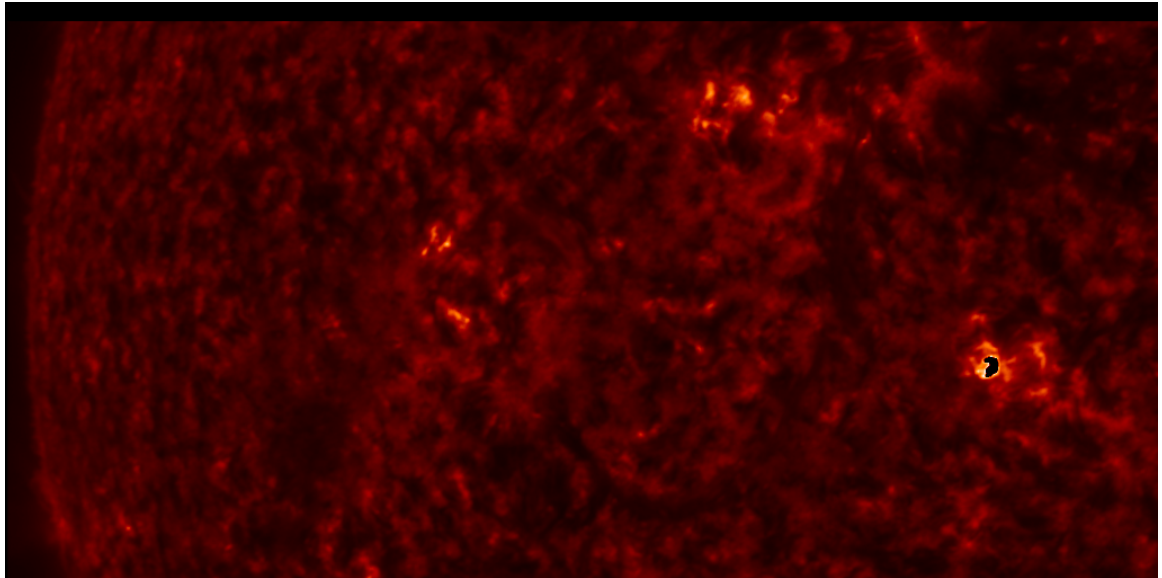


Figure 3.17: Flight data, frame 23.

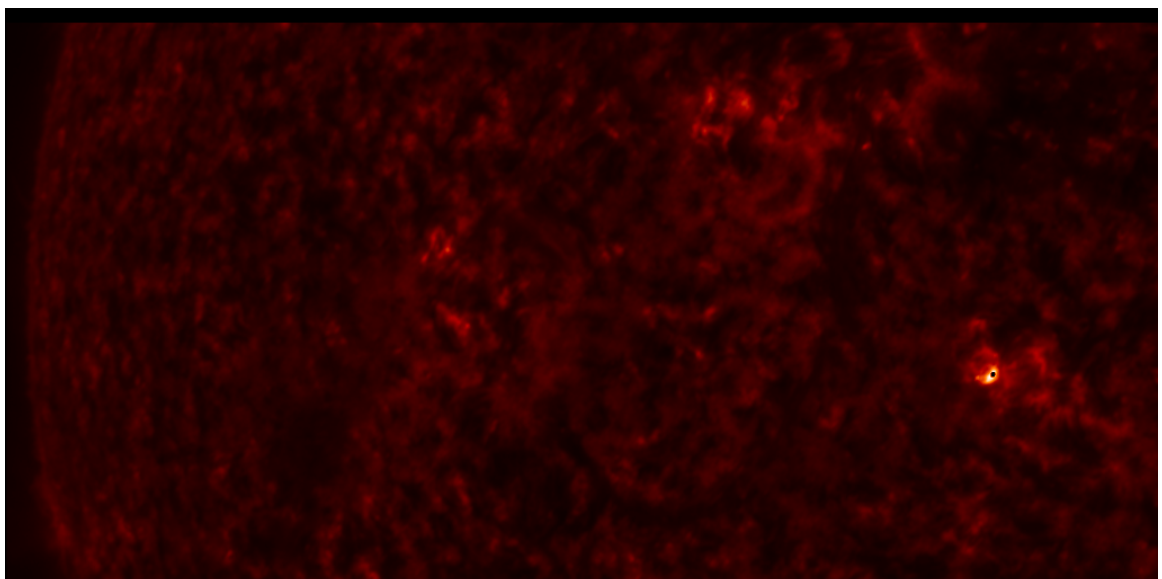


Figure 3.18: Flight data, frame 20.

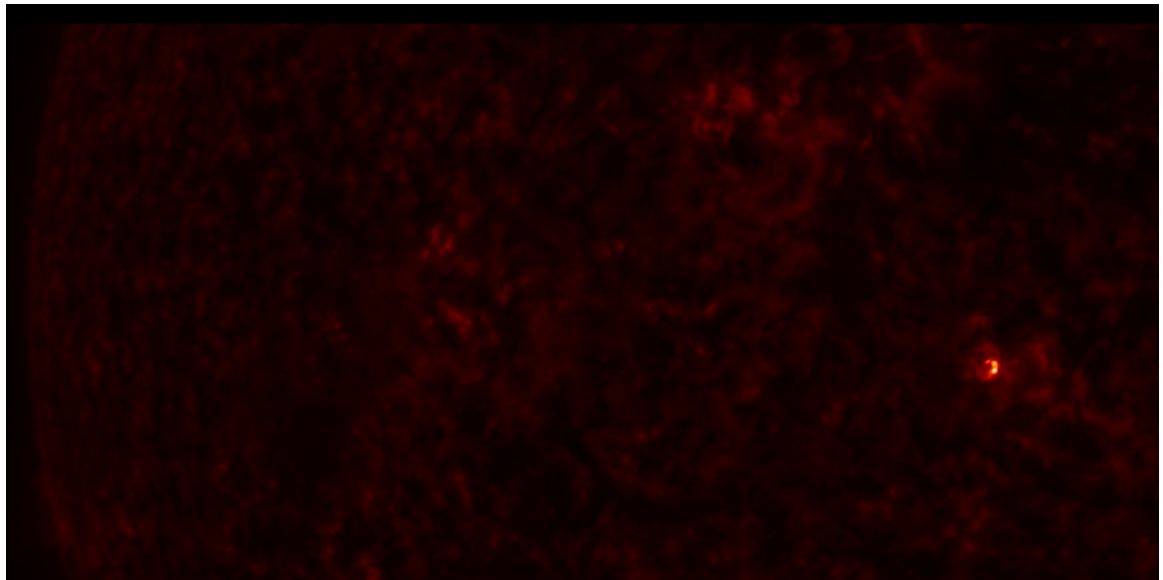


Figure 3.19: Flight data, frame 24.

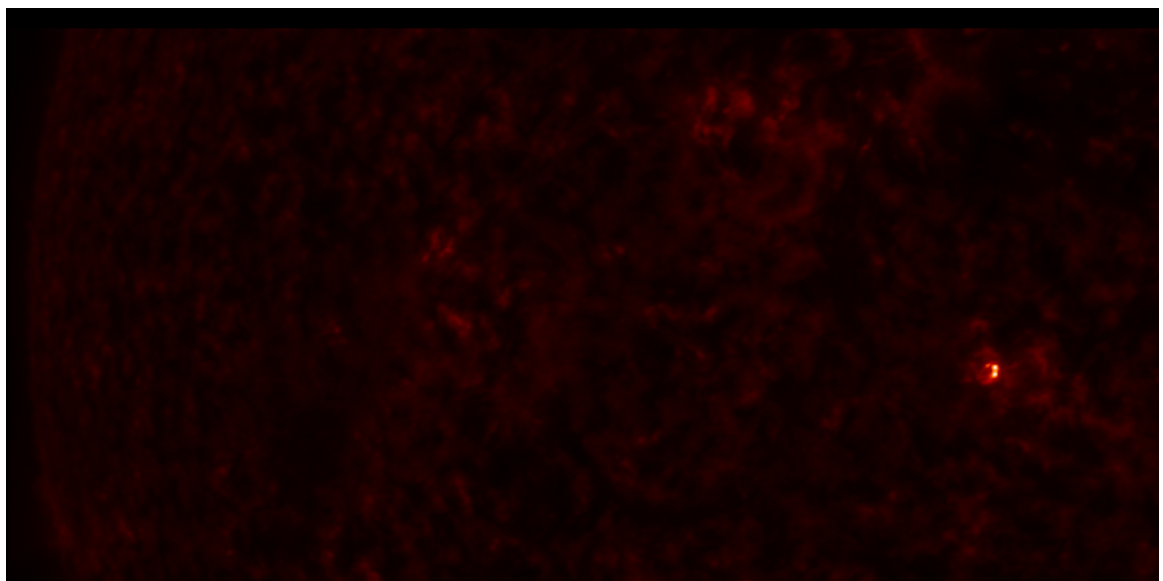


Figure 3.20: Flight data, frame 25.

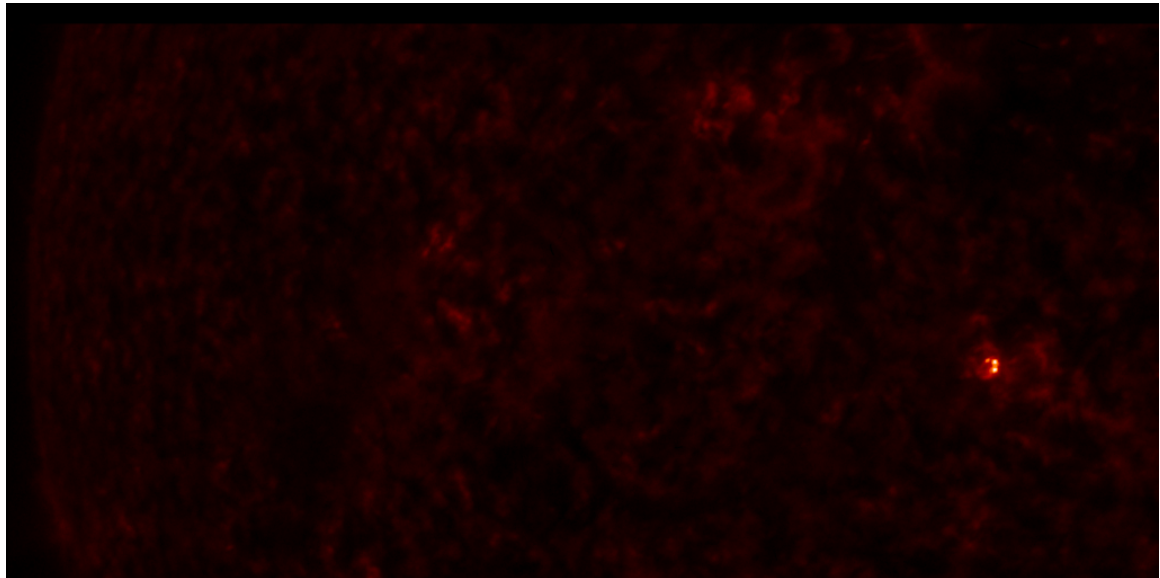


Figure 3.21: Flight data, frame 26.

## CHAPTER 4

## OBTAINING INSTRUMENT FLAT-FIELD FROM A NON-UNIFORM SOURCE

Every scientific instrument must deal with instrumentation issues that affect the quality of the resulting data. For imaging instruments one of these concerns is the instrument’s flat-field, which is a measure of the non-uniformity of instrument response across the field of view. For *MOSES* this issue is doubly important because differences between spectral order data are used to infer spectral line moments. We must have a correction for differences in response that are unrelated to differences in spectrum from pixel to pixel.

This type of correction is normally assumed to be trivial. However without a uniform source of illumination the problem is non-trivial. In this chapter I give a solution to the problem of flat-fielding a CCD detector in an unvignetted optical system in the Extreme UltraViolet (EUV) region of the spectrum, where uniform sources of illumination are rarely available.

4.1 Flat-fielding

Imaging instruments all have non-uniform instrument response to a fixed source of radiation from pixel to pixel. This variation in response is diagnosed and corrected using a “flat field” – conceptually (and often in practice) the image of a “flat” source, having uniform intensity. This image will not be flat and will contain imperfections in the instrument (e.g. scratches on lenses, dust on detectors, etc.) as well as vignetting – a gradual reduction in image intensity toward the periphery of the image common in optical instruments. If the flat-field is properly normalized any image can be

“flattened” by dividing it by the flat-field, thus removing the non-uniformity in pixel response.

Obtaining a flat-field is normally accomplished by shining a uniform intensity beam into the instrument. For optical telescopes operating in or near the visible regime, the flat source is ordinarily a trivial piece of calibration equipment. It can take many forms, a white target (see figure 4.1), a Lambertian source purchased from an optics catalog, or a bedsheet. I have even flat-fielded telescopes by pointing them at a jar of milk. Normally flat-fields taken in this way introduce a diffuser into the optical train to further smooth the source illumination. More robust methods use the sky as a flat source, either at twilight or blank night sky. Even when the sky is “contaminated” with stars it can often still be used to create a flat-field. See Tyson (1986) for further discussion. It must be noted that techniques for making flats from star-fields cannot be used on “crowded fields” or extended sources.



Interior of the Mayall Telescope

Figure 4.1: The Mayall telescope at Kitt Peak National Observatory. The flat-fielding target is beyond the telescope upper-right of center, hanging on the side of the dome. This type of flat-field is sometimes called a “dome flat”.

## 4.2 In EUV

Sources of uniform illumination are not easily obtained in the EUV. We are often lucky to have a source of any kind. EUV sources include a synchrotron beamline or a high-voltage hollow cathode lamp. A hollow-cathode source has recently been commissioned at MSU in our lab, but was not available for the first MOSES flat-field. The light obtained from such sources is not uniform. We thus face the problem of creating a flat-field from a non-uniform source; moreover, the shape of the source beam is not predictable from first principles.

This problem has been solved before. Every EUV space telescope with CCD detectors has faced it. Surprisingly little is written about the problem in the literature. It would appear research groups are “reinventing the wheel” based on private communications with other researchers or previous experience. At the time we performed the flat-field experiment we knew of no papers on the subject; I have since found a few. Our solution to the problem represents our own independent implementation of a common method, some variation of which has been used often, for example by the SOHO team (Potts & Diver, 2008, uses it to flat-field MDI, on orbit, from solar data), and most recently by SDO (Wachter et al., 2011). The foundational paper on the subject appears to be Kuhn et al. (1991), but we had no knowledge of their algorithm when we created our flat-fields. The experimental procedure was communicated to us by Roger J. Thomas our GSFC collaborator, and optical designer, who is also involved in the SERTS and EUNIS sounding rockets. The algorithm for extracting the flat-field from the raw data is our own.

### 4.3 The Flat-field Experiment

The Solar Physics Laboratory at Goddard Space Flight Center has a hollow cathode source with a vacuum chamber they use as a line source for wavelength calibration of spectrographs (SERTS/EUNIS). It is radiometrically uncalibrated, with an unknown beam structure which is unlikely to remain constant from one experiment to the next, but it produces light at the wavelength of the *MOSES* experiment. The SERTS/EUNIS team graciously made it available to us and provided support for our experiment.

The opening of the hollow cathode lamp is connected to a vacuum chamber under high-vacuum,  $10^{-5} - 10^{-6}$  Torr. The hollow cathode source operates in mechanical vacuum by passing gas under low pressure ( $\approx 1$  Torr) through a hollow metal cathode, with a turbopump on the section between the lamp and the chamber to minimize the streaming of gas particles into the experiment chamber. The potential difference between cathode and anode is several thousand volts. The voltage ionizes the gas and the resulting continuous plasma discharge excites the ions resulting in the production of an emission line spectrum characteristic of the gas in use. We used helium, in conjunction with a multi-layer coated slide (a recycled witness slide created by the GSFC Optics Branch), to obtain the He II 304 Å line that we would observe in flight (detector flat-fields are wavelength dependent). Our response to Si XI 303.3 Å is essentially identical, so tunability is not required. This flat “mirror” redirects the beam path toward the back of the experiment chamber. An aluminum thin-film filter placed over the entrance to the experiment chamber prevents copious amounts of visible light, produced in the lamp, from reaching the slide. Similar filters are used in the *MOSES* optics over the detector housings (see § 3.1.2 on page 21). This beam is our source for the flat-field experiment. As we shall see it contains many

beam features, some of which are traceable to parts of the apparatus unique to this particular experiment. Scratches, and other imperfections in the slide show up in the beam structure. The filter support mesh also forms a shadow on the detector.

Figures 4.2 - 4.4 are photographs showing the experimental setup. Figure 4.2 shows the witness slide used as a folding flat mirror and He II 304 Å wavelength selector, along with its “mount”. The slide is mounted to the inside of one of the vacuum chamber doors. Repeatability in beam positioning is clearly not supplied by this mounting scheme, nor is it essential, so long as the vacuum chamber is not disturbed during data runs. Our analysis algorithm is designed to produce a flat-field independent of either beam features, or beam position.



Figure 4.2: The witness slide.

We put only the detectors with housings into the beam. At the time of this experiment (April 2004) the mirrors had not yet been produced by the manufacturer, so it was not possible to use the full telescope. This produces a usable flat-field because the pixel-to-pixel response variation is due primarily to the detector. Our instrument is unvignetted (by design) and uses no image intensifiers. It has uniform response multi-layer coatings which are used over a small range of incidence angle. The mirrors are far enough from focus that scratches, dust, or other surface imperfections are unimportant, and the flight filters are carefully positioned so that the mesh forms no shadow (see §3.1.2). The filters are assumed to conform to the uniformity specification ( $\pm 1\%$ ) published by Luxel.

We translated each detector within the beam horizontally and took exposures at seven positions. All data for each of the seven positions were taken without removing and replacing the vacuum door. We chose to use constant 200 pixel shifts, a translation of  $2700 \mu\text{m}$  between beam positions. We thus had beam positions  $[-8100, -5400, -2700, 0, +2700, +5400, +8100] \mu\text{m}$ . The origin was chosen arbitrarily; it is merely a position midway in the range of the translation stage. The full width of the beam sampled is 3248 horizontal pixels, 2048 pixels detector width  $+200 \times 6$ .

At each beam location we took 9 images of 3 sec duration, as well as dark images with the source off (true darks), and dark images with the source on, but the shutter closed (what we call “greys”), verifying that there was minimal light leakage around the shutter/filter assembly. Exposure control is achieved using a pupil shutter controlled by a signal from our experiment computer. The 3 sec exposure time was chosen after some trial and error as a balance between deep exposures with many counts even in dim regions without saturating in bright areas. The exposures were taken with the detectors operating at flight temperatures ( $-30^\circ\text{C}$ ), using the flight thermal control circuits and a non-flight thermal reservoir, cooled via liquid nitrogen

supplied through vacuum feedthroughs. The exception to this procedure was detector 5 (a non-flight engineering unit) whose temperature control failed due to a broken control thermistor. Detector 5 was chilled to below  $-30^{\circ}\text{C}$  using passive cooling via the thermal reservoir block and the temperature was allowed to vary, but kept below  $-30^{\circ}\text{C}$ . We believe this has a negligible impact on the flat-field as our detectors have little dark current left below  $-20^{\circ}\text{C}$ .

Figure 4.3 shows a view through the rear of the vacuum chamber. The rear chamber door has been removed. This view shows the position of the fold-flat witness slide from the direction of the detector mount. The light from the source enters through an aperture on the back wall of the chamber off-camera to the left. Also visible are the LN2 feedthroughs, and various electrical harness and feedthroughs.

Figure 4.4 shows the view through the front chamber door. The silver ring to the right of center is the frame of the thin-film aluminum filter, affixed over the shutter on the source entrance aperture. To the right, near center, is a detector housing mounted in a ring. The mounting ring is attached to the translation stage. To the left of the detector housing are the thermal reservoir block and conductive thermal straps. The translation stage, detector, mount, and reservoir, along with the flight unit read-out electronics (ROE, not visible mounted on the back) are attached to a mounting table whose purpose is to raise the detector up into the beam.

#### 4.4 Flat-field Experiment Data

Upon examining the signal levels in our exposures it became clear that the 3 sec exposure time was not tightly controlled. Figure 4.5 shows this. Clearly some exposures are very far from the 3 sec nominal exposure time. The majority lie in a band, but even these do not have tight exposure control. The flat-field exposures were poorly



Figure 4.3: View through the rear chamber door.

controlled due to inadequate software control of the port activating the shutter. We do not know the actual exposure time of any data frame because no timing information was recorded. Absolute knowledge of exposure time is not required using our method, but the images must be corrected to the same effective exposure time.

I cleaned the data by first calculating, for each detector position, the median average signal level for the 9 exposures and then scaling each exposure to that average signal level. This procedure failed for one position on detector 3 which had so many

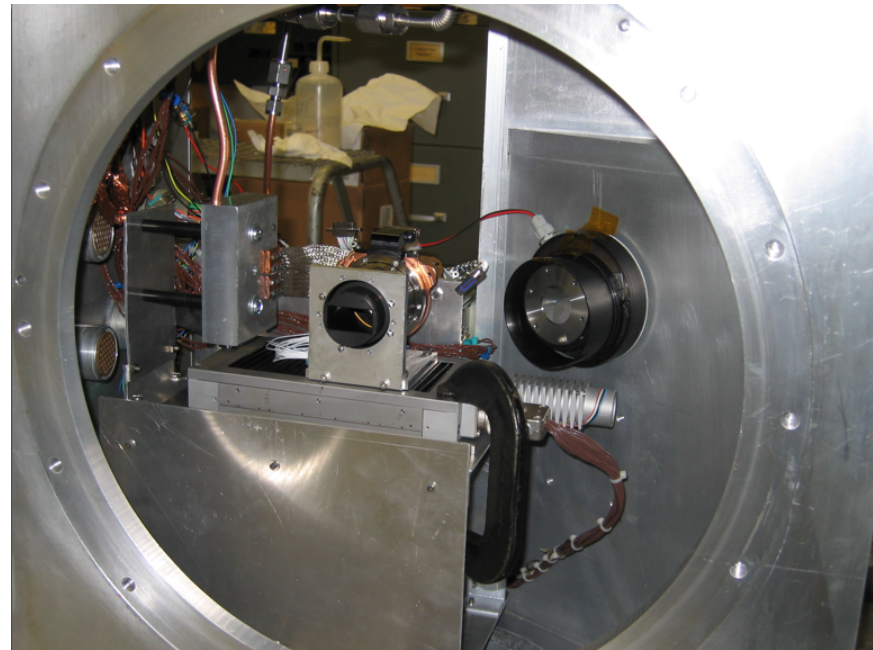


Figure 4.4: View through the front chamber door.

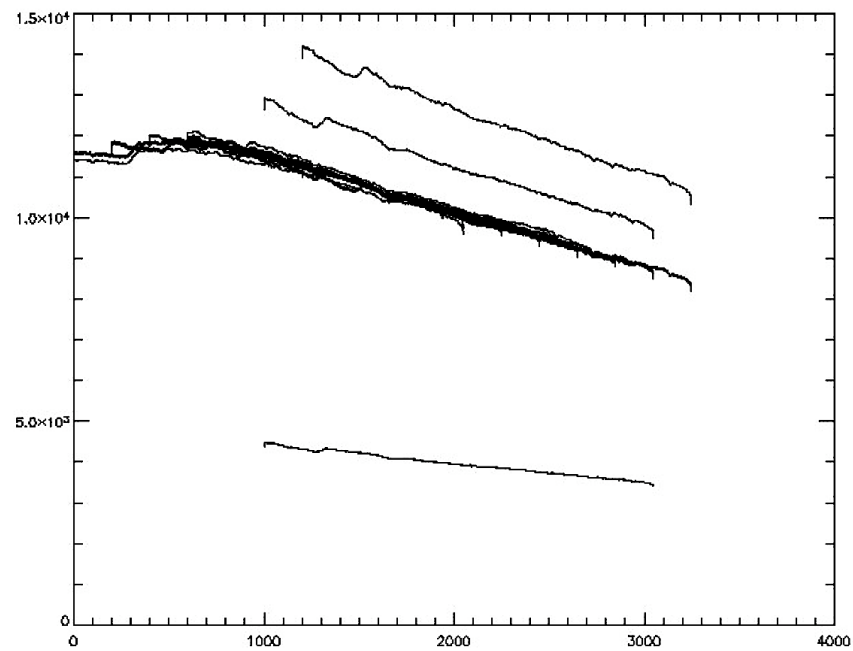


Figure 4.5: Column averages of detector signal in DN for each position and each exposure for detector 5. 16383 DN is the saturation level.

widely varying exposure times (only 2 of 9 appeared at all close to the 3 sec nominal) that the median signal level was not useful in getting an effective exposure time close to 3 sec. For this detector at this position I simply chose the average of the 2 “good” frames as the reference signal level.

This effectively forces a consistent (but unknown) exposure time for each set of 9 exposures. I then form one image from the average of these 9, and an error frame by calculating the standard deviation of the mean for each pixel.

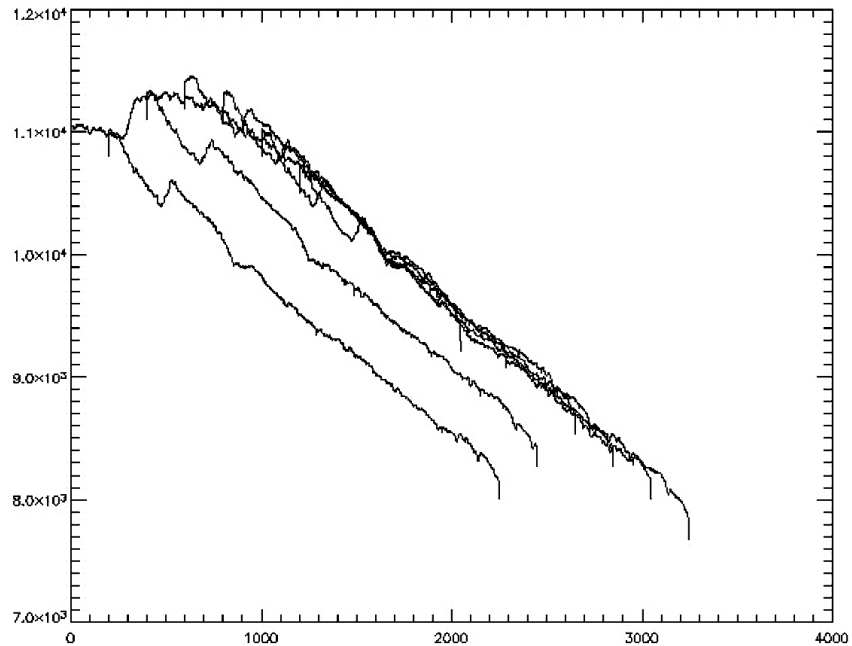


Figure 4.6: Column averages of detector signal in DN for each position. The different positions do not overlap as they should.

See figure 4.6. This figure shows that the effective exposure time chosen in the previous step is not consistent from one detector position to the next. To ameliorate this error we choose the unknown exposure time of the first detector position as a reference and adjust the total intensity of each image to scale with it and each succeeding image in regions where they overlap. Each position has 1848 pixels of

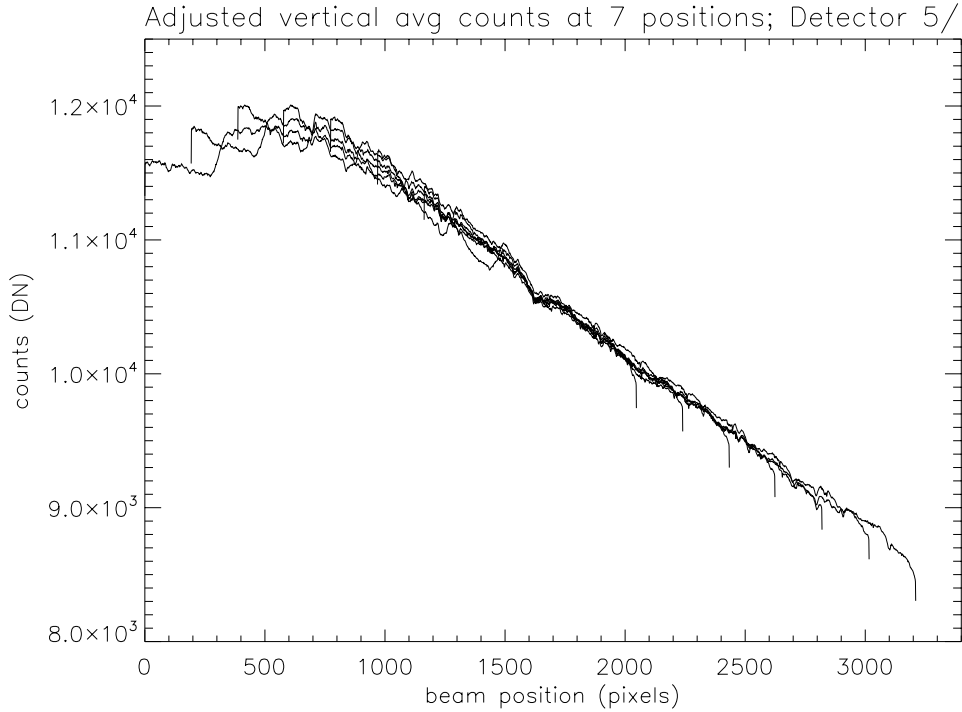


Figure 4.7: Column averages in DN for each position as before. Data shown are for Detector 5. Note how much tighter the overlap between adjacent positions has become.

beam overlap with the next one. Although these overlapping regions are on different portions of the CCD and thus subject to differences in the flat-field, these differences will have a minor effect on the average of  $1848 \times 1024$  pixels.

The result of performing this averaging procedure is shown in figure 4.7. Now we have a set of seven images for each detector with the same effective exposure time, which we call the “clean data frames”. These are the input data used to derive the flat-field.

#### 4.5 The Algorithm

The series of images contains features that don't move (the flat-field) multiplied by features that do move (the beam). Figure 4.8 shows images from three adjacent positions. Glancing between them the eye can readily distinguish beam features from flat-field.

The  $n^{\text{th}}$  clean image is a product of the flat-field and a section of the beam (plus some noise, here denoted  $\eta_n$ ):  $I_n = B_n Q + \eta_n$  with

$$B_n(x, y) = \begin{cases} B(x + \tau_n, y) & 0 \leq x < \Delta \\ 0 & \text{otherwise} \end{cases}$$

The symbol  $\tau_n$  is the displacement of the  $n^{\text{th}}$  detector position in beam image space, and  $\Delta$  is the width of the detector, 2048 pixels.  $B(x, y)$  is the beam and  $Q$  is the flat-field. The detector positions come in 200 pixel increments,  $\tau_n = [0, 200, 400, 600, 800, 1000, 1200]$ . The values of  $y$  run from 0 to 1023, and it is presumed there is no shift in the  $y$  direction. The  $B_n$  have substantial regions of overlap. Each pixel in the beam is sampled from 1 to 7 times.

1. Start with a uniform flat-field  $Q$ . In our case we simply start with an image having the uniform value 1.0.
2. Let  $B_n = \frac{I_n}{Q}$ . Because the flat-field is incorrect these  $n$  samples of the beam,  $B_n$ , do not match in the regions of overlap.
3. Combine the  $B_n$  into one continuous beam by averaging over the overlapping regions. Let  $w(x)$  be such that

$$w(x) = \begin{cases} 1 & 0 \leq x < \Delta \\ 0 & \text{otherwise} \end{cases}$$

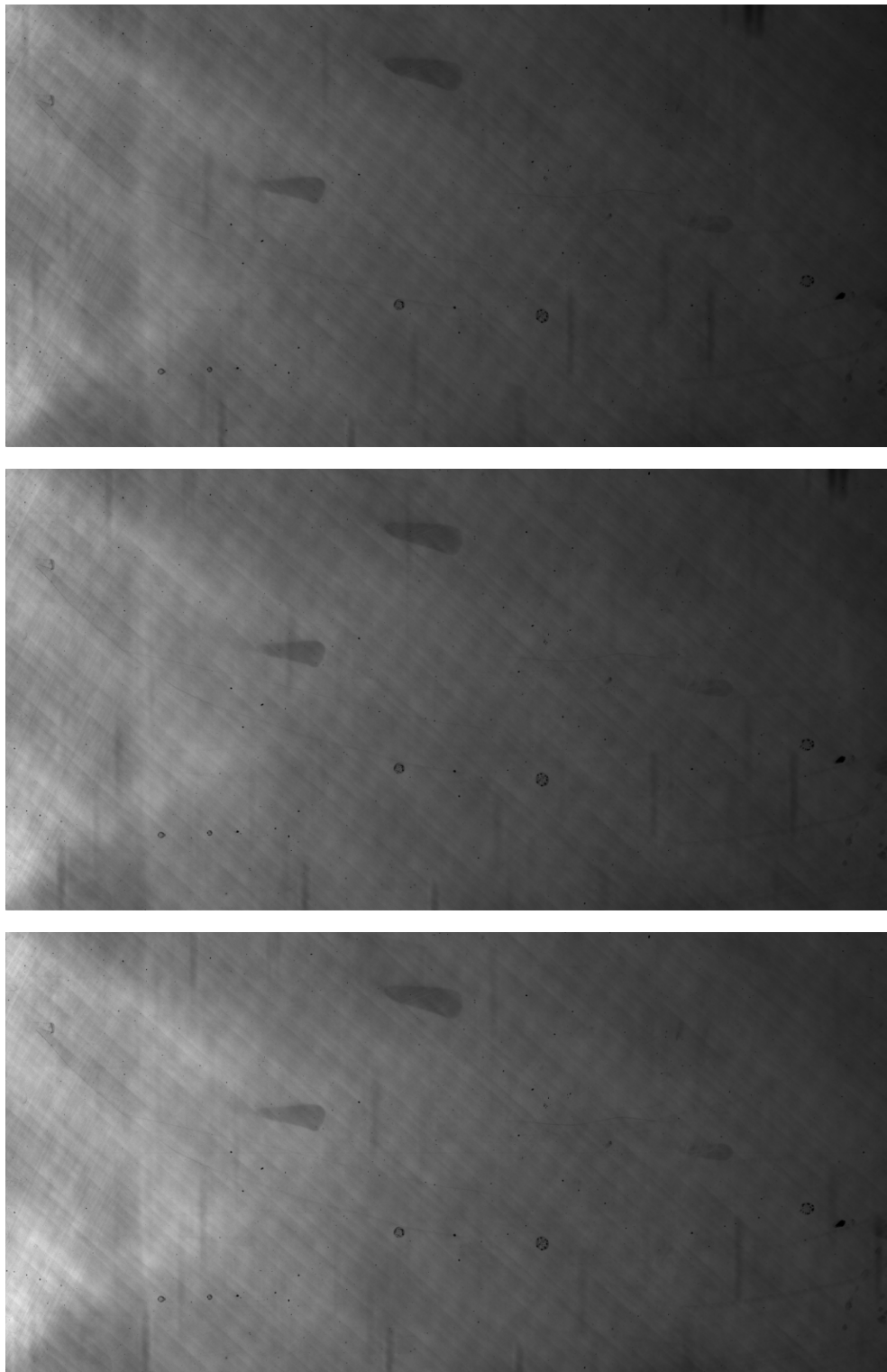


Figure 4.8: Three clean data frames from adjacent detector positions. The cross-hatch pattern is the shadow of the mesh. Vertical dark linear features are imperfections on the slide.

then

$$B(x, y) = \frac{\sum_n B_n(x - \tau_n, y)}{\sum_n w_n(x - \tau_n)}.$$

The accumulator function  $A(x) = \sum_n w_n$ , stores the number of overlaps, from 1 to 7. Its central 848 columns contain 7's. On each side of the center are bands, 200 columns wide, which descend stepwise from 6 to 1. It only needs to be calculated once.

4. Smooth  $B$  with a gaussian fourier domain windowing function of width  $\sigma_i = \sigma_{i-1}\chi_{i-1}^2$ , where

$$\chi_{i-1}^2 = \left\langle \frac{1}{2048 \times 1024} \sum_{x,y} \frac{(B_n Q - I_n)^2}{\eta_n^2} \right\rangle$$

represents the average reduced chi-squared statistic from the previous iteration of the algorithm. The error frames (see §4.4) are used for  $\eta_n$ . Mathematically the smoothing is performed by

$$B^* = \mathcal{F}^{-1} \left[ \tilde{B} \exp \left( \frac{-\mathbf{k} \cdot \mathbf{k}}{2\sigma_i^2} \right) \right],$$

where  $\mathcal{F}$  is the Fast Fourier Transform (FFT), and  $\tilde{B} = \mathcal{F}(B)$ . This is a low-pass filter, damping out high spatial frequencies in  $B$ . This step depends on the inherent smoothness of beam features. The emission region in the lamp is large and there is no pinhole or other optical element to make it a point source, so the beam is a fuzzy blob with unfocused filter and mirror features superimposed, whereas the flat-field is on the CCD, in as sharp a “focus” as can be. We do not know *a priori* what smoothing width,  $\sigma$ , will neatly separate the beam from the flat-field so in the initial step we choose, by trial-and-error, an arbitrary smoothing width much smoother than the size-scale of any flat-field features. As the algorithm iterates,  $\chi^2$  tunes the smoothing into the correct

regime. When the smoothing is too aggressive  $\chi^2$  will be large, and the size of the smoothing kernel (in fourier space) will increase in the next iteration. Likewise, if the smoothing is not sufficient,  $\chi^2$  can become less than one and the smoothing kernel will be smaller in the next iteration.

In practice this step requires finesse. The beam is generally not going to be a periodic structure with continuous derivatives at the boundary, so artifacts will be introduced by the FFT (see figure 4.9). To fix that I first removed the overall linear trend from the beam. Define detrending as:

$$\mathcal{D} : \mathcal{D}[B] = B_d, \quad \text{where}$$

$$B_d = B(x, y) - T(x), \quad \text{with}$$

$$T(x) = \bar{B}(0) - \frac{\bar{B}(0) - \bar{B}(3248)}{3248}x$$

The average,  $\bar{B}$ , is carried out over  $y$ . Then I appended an antisymmetric (about  $x$ ) copy ( $B_d^{[\text{AS}]}(-x, y) = -B_d(x, y)$ ) on the end to form a reasonably periodic function with nearly continuous derivatives across the boundary.

$$\mathcal{AS} : \mathcal{AS}[B_d] = B_{\mathcal{F}} \quad \text{where}$$

$$B_{\mathcal{F}} = B_d(x, y) + B_d^{[\text{AS}]}(x - 3248 \times 2, y)$$

The function,  $B_{\mathcal{F}}$  is then transformed, smoothed, and inverse transformed, and then finally the antisymmetric copy is thrown away by multiplying by zero only for  $x > 3248$  and the linear trend added back to obtain a smoothed beam sans fourier artifacts.

5. Let  $Q_n = \frac{I_n}{B_n^*}$ , where  $B^*$  is the smoothed beam. This will give multiple incompatible flat-fields.
6. Average the multiple expressions of the flat-field:  $Q = \langle Q_n \rangle$ .

7. Repeat for a fixed number of iterations. I used 100.

The IDL code which implements this algorithm is on the CD (see B.7).

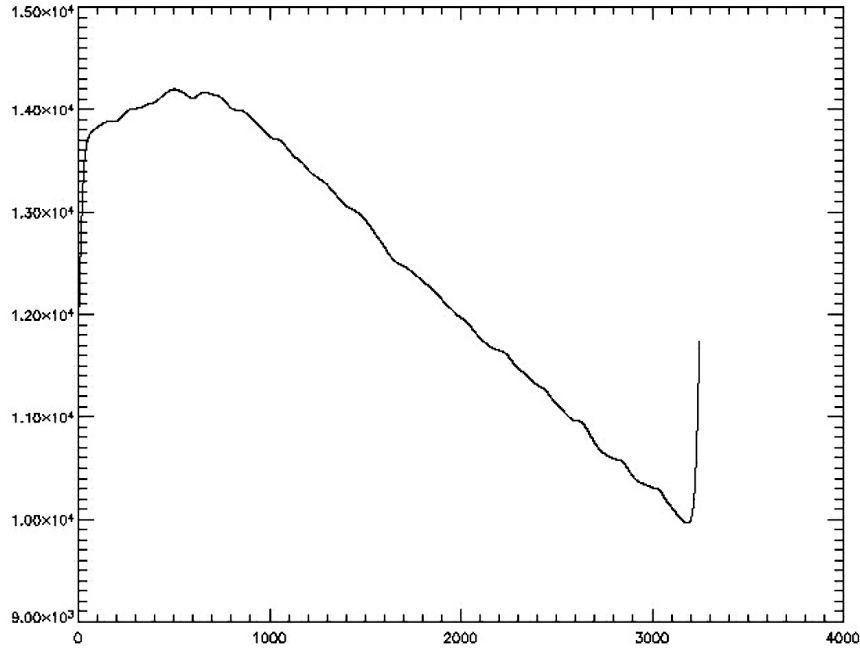


Figure 4.9: Another column averaged DN plot. The result of a “naive” fourier smoothing operation. The artifacts at the edges are the result of the much different signal levels and derivatives of the beam at the edges. The FFT forces the beam to become a periodic function.

#### 4.6 The First Pass

I applied the algorithm described in §4.5 to the clean data frames, starting with detector 5. The resulting flat-field and beam are shown in figures 4.10 and 4.11. The results are encouraging. We see that both the beam and the flat-field contain subtle features which our algorithm is picking up.

The flat-field contains sharp features, such as the small dark “coffee rings” in the lower-center. It also has some “smudge-like” features. The subtle diagonal lines

extending downward from left to right are real and can be seen in visible light microscope images. They have a ready explanation in the back-thinning process that created our rear-illuminated CCD's – these are machining marks from the polishing process which removed the substrate from the back of the silicon.

Looking at the beam, we see its overall broad elliptical shape, but superimposed on that is a periodic cross-hatch pattern. This is the out-of-focus shadow of the nickel wire mesh onto which the thin-film aluminum filter was bonded. The shadow has a variation between mesh cell center and edge of 4 – 5 parts per thousand. I believe many of the vertical bar features are due to blemishes on the multi-layer slide. Witness slides are mainly used to verify the proper wavelength response of the multi-layer and analyze the performance of the deposition chamber at different points within. They are not meant to be used as optics. The slide has many scratches and even gloveprints on it, as can be verified by examination of figure 4.2, and though out-of-focus they will have some effect on the beam.

Examining more closely we see that some artifact of the beam, an echo of the wedge-shaped structure on the left side, remains in the flat-field. It may be that this artifact remains because the left side is the first detector position and the 200 left-most pixels of it are not sampled by any other detector position, so it may be difficult to suppress the strong beam structure here. However examining the residuals,  $B_n Q - I_n$  (figure 4.12), reveals an even more troubling problem. These residuals are not signal uncorrelated. To the contrary there appears to be a bipolar structure ordered bright to dark. It is especially obvious when looking at the vertical bar beam features. The shift is not the constant 200 pixels it was supposed to be: this is the signature of using the wrong detector positions. The stepper controller for the translation stage has 1 micron steps (significantly less than a pixel width), but did not provide accuracy to 1 micron. We attempted to get 200 pixel increments between positions, but the actual

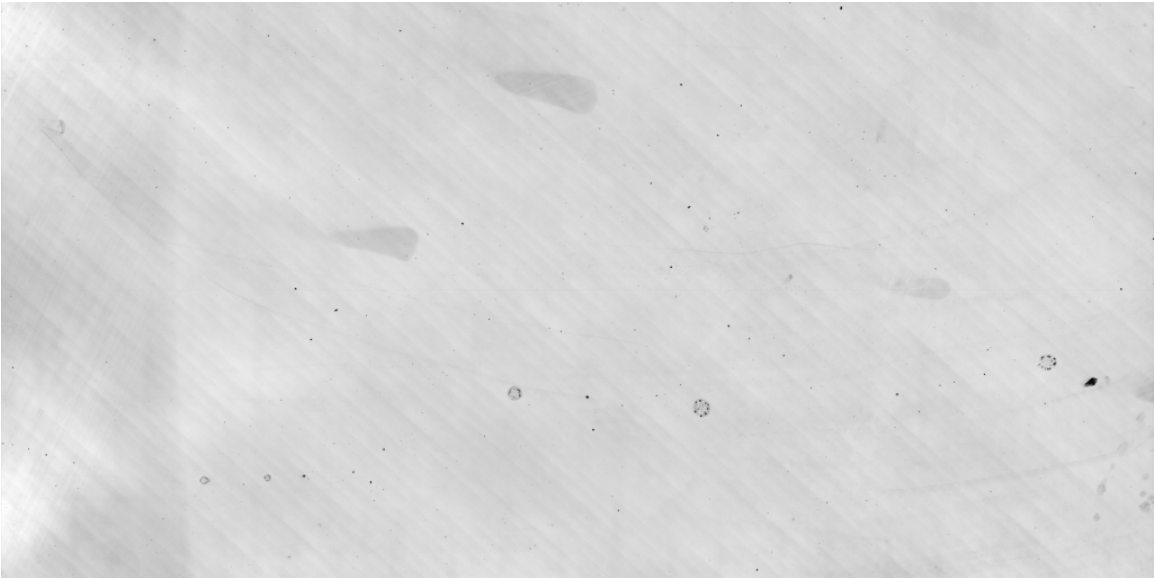


Figure 4.10: The first pass flat-field for detector 5. This and all images taken from a detector are oriented as though looking down onto the photosensitive surface of the CCD.



Figure 4.11: The first pass beam for detector 5.

increments turn out to be somewhat less than 200 and are inconsistent, by more than a pixel width, from one position to the next. We must infer the correct detector positions from the data.

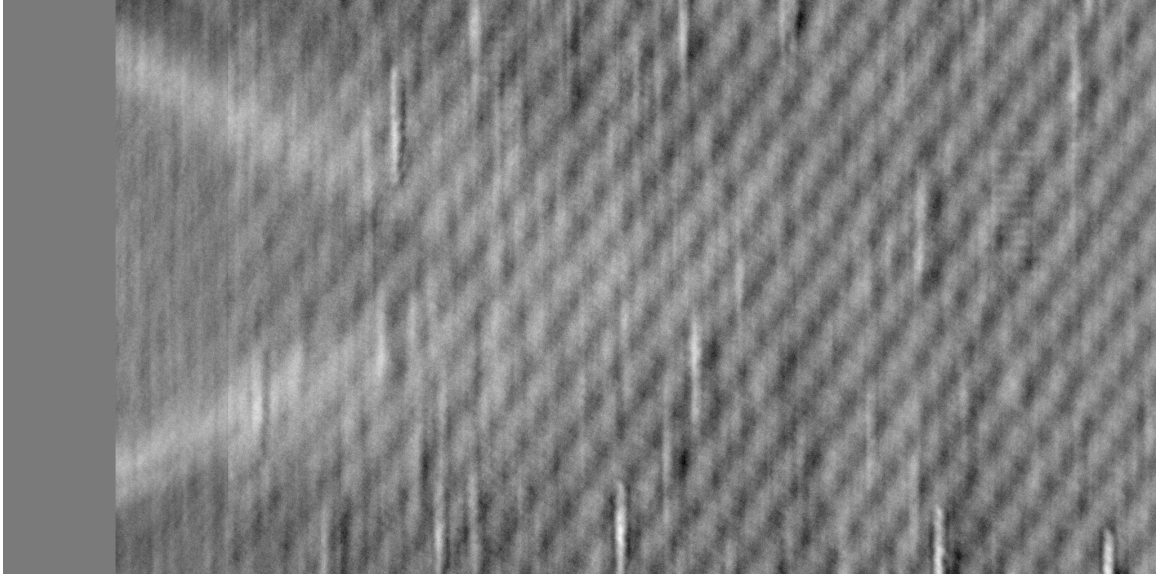


Figure 4.12: The residuals for the 1st detector position of detector 5. Note the correlation with the beam signal.

#### 4.7 Cross-correlation

To determine the detector positions accurately we cross-correlate one beam sample,  $B_n$ , with the next one and see where the correlation peaks are.

$$B_n \star B_{n+1}(\mathcal{L}) = \sum_{i,j=-\infty}^{\infty} B^{[n]}(i,j)B^{[n+1]}(\mathcal{L} + i, j)$$

where  $\mathcal{L}$  is the lag. The flat-field features are always in the same place, so it is important to determine  $B_n$  from the clean data flat-fielded with the first-pass flat-field,  $B_n = I_n/Q$ . Then I detrend the  $B_n$ , otherwise a large correlation peak at a lag of zero will dominate:

Figure 4.13 shows an example of this procedure. The oscillatory behavior comes from the mesh shadow in the beam. A correlation peak appears each time we shift by enough to make the mesh shadows line up again. The peaks near 200 are the ones we want, but they do not yet stand out. Both the mesh shadow and the detector

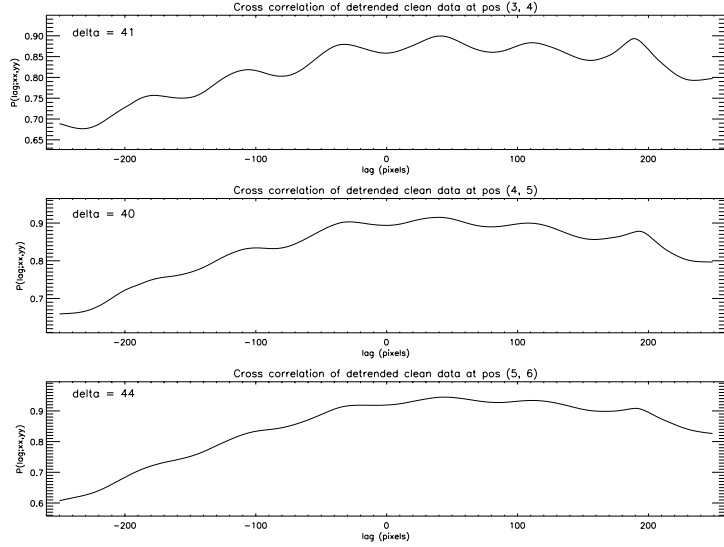


Figure 4.13: Cross-correlations for 3 position pairs from detector 5 data.

shift are dominated by the broad “mountain” on which they are sitting which is due to the very broad elliptical shape of the overall beam.

We can use our fourier filtering technique to remove the large scale beam features by making it a high-pass instead of a low-pass filter. Instead of multiplying in fourier space by a gaussian multiply by one minus a gaussian.

$$\mathcal{HP} \left[ B_{\mathcal{F}}^{[n]} \right] = \mathcal{F}^{-1} \left[ \tilde{B}_{\mathcal{F}}^{[n]} \left\{ 1 - \exp \left( \frac{-\mathbf{k} \cdot \mathbf{k}}{2\sigma^2} \right) \right\} \right]$$

Putting the result of this high pass filter back into the cross-correlation step, adjusting  $\sigma$  with some trial-and-error to arrive at a reasonable choice, gives good results. The right smoothing parameter removes the broad shape of the beam, but leaves the mesh shadow and the vertical bars. Without the imperfections in the witness slide we would have found it difficult to determine the correct detector positions from the data. We find the tallest correlation peak where all these beam features line up. Figure 4.14

gives an example of the resulting correlation plots. The position of the tallest peak in each plot is given by “delta” in the upper-left plot corner, to the nearest pixel. The actual detector shifts were several pixels less than the nominal value of 200. It is also clear that the translation stage could not provide precision to better than a few pixels.

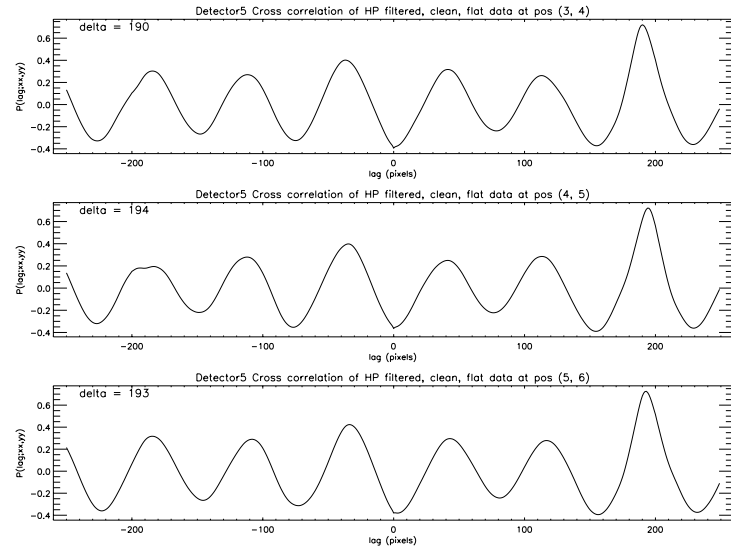


Figure 4.14: Correlation plots for the same position pairs after high-pass filtering. The tallest peaks give the correct detector shifts.

#### 4.8 The Second Pass

We used the new detector shifts to redo the analysis beginning with the flat-field from the first pass as an initial guess. The results of the second pass are shown in figures 4.15 - 4.16.



Figure 4.15: The flat-field for detector 5, second pass.



Figure 4.16: The beam for detector 5, second pass.

The residuals,  $B_n Q - I_n$ , still show signal correlation (figure 4.17). There is still the obvious wedge artifact creeping into the flat-field, for example. There is also some of the mesh shadow texture, and possibly some remaining incorrect detector shift as shown by bipolar features. The second pass residuals are a great improvement over the first however. More improvement might be obtained by redoing the analysis in a third pass, allowing for non-integer detector positions (in pixel units). There is no reason to believe that the translation stage happened to give us whole pixel shifts. It

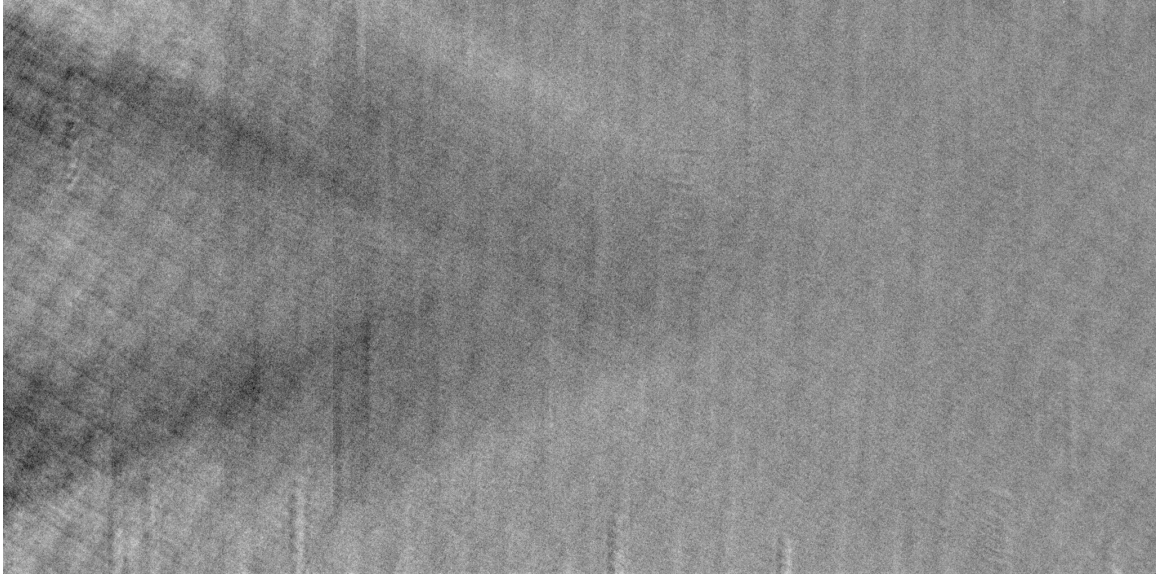
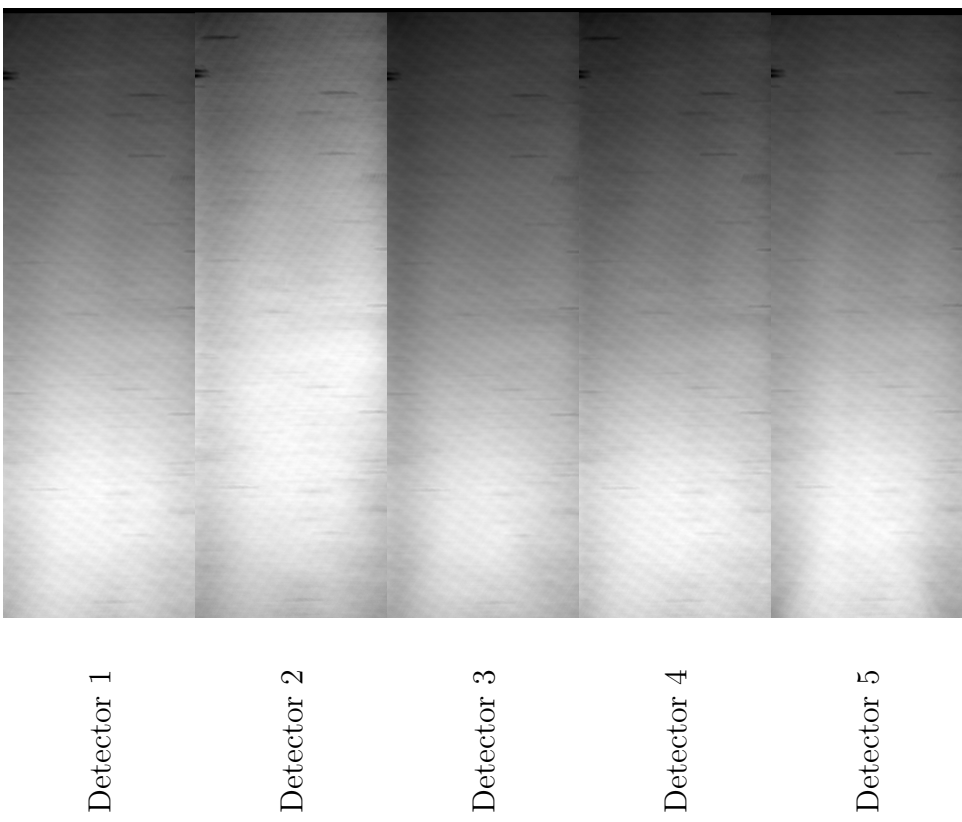


Figure 4.17: Residuals for detector 5, position 3.

is also possible that there is a small  $y$ -axis pixel shift as well. The translation stage and detector  $x$ -axis were intended to be aligned, but no special effort was taken to ensure that this would be so to sub-pixel accuracy.

To the present time no efforts have been made to implement such further refinements. The second pass flat-fields are the current best-effort and are the ones used in analysis of *MOSES* flight data. The magnitude of the second pass residuals in DN is  $\bar{R} = -4.54$  with a standard deviation of  $\sigma_R = 24.1$ . For comparison the mean signal in the clean data is  $\bar{I} = 10,700$  with  $\sigma_I = 820$  so our flat-fields are accurate to 0.04%. The variance in the residuals is 0.09% the variance in the data. Therefore, the accuracy of the final flat-fields is dominated by the thin-film aluminum filters used in flight, which are only uniform to 1%. Figure 4.18 shows all the final flat-fields with their associated beams.

B



Q

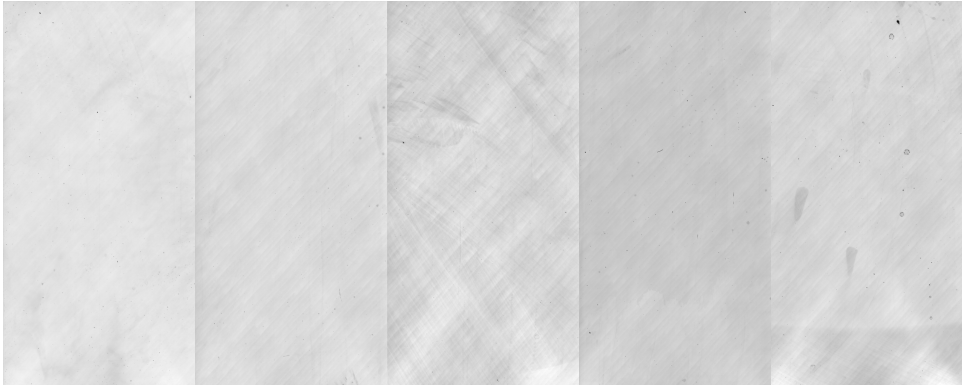


Figure 4.18: Flat-fields and beams for all five detectors. Detectors 1, 2, and 3 were chosen as flight units, partially on the basis of the quality of their measured flat-fields.

#### 4.9 Acknowledgements

I would like to express heartfelt thanks to the whole SERTS/EUNIS team and especially Roger J. Thomas, Marvin Swartz, and Chuck Condor for letting me use their facility, and making it work. I couldn't have done anything without them.

## CHAPTER 5

A TRANSITION REGION EXPLOSIVE EVENT OBSERVED IN HE II WITH  
THE *MOSES* SOUNDING ROCKET.

5.1 Introduction

Transition region Explosive Events (EEs) have been widely observed with spectrographs such as the High Resolution Telescope and Spectrograph (*HRTS*) (Brueckner & Bartoe, 1983; Cook & Brueckner, 1991), and *SUMER* (Innes et al., 1997, and references therein). With *HRTS* they were most typically observed in C IV 1548 Å, 1550 Å. In *SUMER* Si IV 1393 Å, 1402 Å are used. Both line doublets are formed at temperatures of  $\sim$ 100,000 K (100,000 K and 63,000 K respectively according to Arnaud & Rothenflug 1985). EEs can be observed across a temperature range from 20,000 K in C II to 250,000 K in O V (Moses et al., 1994). EEs are characterized by large non-thermal doppler broadenings. Values typically given are  $100 \text{ km s}^{-1}$  to the red and blue (Dere, 1994). EEs divide between those which are broadened to both sides of line center and those predominantly broadened to one side of line center (Cook & Brueckner, 1991; Dere et al., 1989). Events with dominant blue wings are more common than those with dominant red wings (Cook & Brueckner, 1991; Dere et al., 1989). They are typically small, 1500 km in length (Dere, 1994; Dere et al., 1989, 1991; Cook & Brueckner, 1991). The two wings may be displaced from each other by 1000 - 2000 km (Dere et al., 1989; Dere, 1994), although displacements up to 6000 km have been seen (Innes et al., 1997). The typical lifetime of an event is 60 - 90 s (Moses et al., 1994; Dere, 1994; Dere et al., 1991). Considerable variation from “typical” properties is seen from one EE to another (Dere et al., 1989). Events are seen with velocities up to  $400 \text{ km s}^{-1}$  (Moses et al., 1994; Dere et al., 1989), sizes up

to 4000 - 5000 km (Innes et al., 1997; Cook & Brueckner, 1991), and lifetimes up to 4 - 5 min (ibid). One extremely large event has been seen with a length of  $\sim$ 20,000 km (Brueckner et al., 1988).

EEs in active regions coincide with emerging flux, while EEs in the quiet sun concentrate in or near the quiet sun network above regions of cancelling flux (Dere et al., 1991). They are typically located along a magnetic neutral line (ibid). These features suggest EEs are a signature of magnetic reconnection in the transition region. It has been postulated that reconnection processes producing bipolar jets are responsible for EEs (see for example the cartoon in figure 2 of Dere et al. 1991). The red and blue wing velocities are identified with the Alfvén speed at the reconnection site. Innes et al. (1997) report three events in which raster scanning of the *SUMER* slit clearly shows the bi-directional jet structure. They found that the doppler shifts change sign from red to blue within 2-3000 km, the wings move away from the region where the sign change occurs, and the brightest emission is found at the sign change.

This chapter concerns a He II 304 Å EE observed during the 2006 February 8 flight of the *MOSES* instrument (see §3.6). We will demonstrate what can be learned about the event from imaging data alone and show the magnetic context of our EE, which has two cancelling dipoles under it. We use an indirect spectral analysis technique we call “parallax analysis”, described in section 5.5, to infer the doppler shifts, and line width along the N-S axis of the event, perpendicular to the dispersion direction of *MOSES*. The He II 304 Å event we report here is a bi-directional jet from sky-plane motion as well as doppler shift. We will show that its properties fit within the envelope found by previous authors and it may properly be identified as a transition region explosive event. We believe this to be the first He II 304 Å explosive event reported in the literature (an explosive event in He II at 256 Å was reported by Dere

et al., 2007). However, contrary to previous models we find that the structure is not collinear, and that the jets are not anti-parallel.

## 5.2 Data Reduction

In this chapter we analyze only data from the  $m = 0$  and  $m = +1$  spectral orders. Data have been dark-subtracted and flat-fielded. We have co-aligned the two orders, and removed optical distortion (see 5.2.1). The data preparation uses the IDL code in `coregisterate.pro`, `moses_prep.pro`, `moses_align_final.pro`, and `drift_compensate2.pro` (to remove the pointing drift). These code files are included on the supplemental CD (see B.8). Data frames have been normalized so that different frames have the same mean  $\text{DN s}^{-1}$  as the exposure closest to apogee. The following equations describe the normalization process:

$$I_0'^j = \frac{\langle I_0^a \rangle}{\langle I_0^j \rangle} I_0^j \quad (5.1)$$

$$I_{\pm 1}'^j = \frac{\langle I_0^a \rangle}{\langle I_{\pm 1}^a \rangle} \frac{\langle I_0^a \rangle}{\langle I_0^j \rangle} I_{\pm 1}^j \quad (5.2)$$

with superscript  $j$  indexing exposure number, 0 - 26, and superscript  $a$  indicating the exposure closest to apogee, frame 13. This procedure corrects for the different throughput in each channel and the variance in effective exposure time due to atmospheric absorption over the flight. The first factor in eq. 5.2 is the non-time-varying relative response of the orders. The second factor (which also appears in eq. 5.1) removes the effect of time varying atmospheric absorption without model-dependent assumptions. The renormalization procedure has been implemented in `renormalize2.pro`. The resulting normalization constants are stored in `renormalize2.sav`. Both of these files are on the CD.

### 5.2.1 Alignment

After dark subtraction the images from the three spectral orders must be coaligned as accurately as possible. All spectral measurements depend on this step. We use a low-order polynomial coordinate transformation for coregistration, allowing for the slight distortion that is present in the outboard ( $m = \pm 1$ ) images:

$$x' = \sum_{i=0}^1 \sum_{j=0}^1 a_{ij} x^i y^j, \quad (5.3)$$

$$y' = \sum_{i=0}^1 \sum_{j=0}^1 b_{ij} x^i y^j. \quad (5.4)$$

The images were deemed aligned when the sum of the square of the residuals, normalized by intensity (in the manner of  $\chi_R^2$ ) was minimized as a function of the polynomial warping coefficients  $a_{ij}$  and  $b_{ij}$ .<sup>1</sup> By aligning the three orders, we effectively assume a zero mean doppler shift over the FOV; the measurement of nonzero mean doppler shift would require calibration of the instrument with an extremely well-collimated EUV line source, which was not available to us. The alignments of the three spectral orders were repeatable from exposure to exposure, to better than 0.2 pixel RMS. No measurable relative movement of the detectors should occur in flight, so the median alignment across all of the exposures was taken as the alignment for the entire sequence.

## 5.3 Zero Order Data and Magnetic Context

The  $m = 0$  channel is equivalent to a narrow-band 304 Å imager. On the solar disk, the passband is dominated by the He II line, which we expect to account for

---

<sup>1</sup>In this application, the most consistent results are found when  $\chi_R^2$  is normalized by the number of *overlapping* pixels, which is itself a function of the alignment parameters.

more than 95% of the detected photons (Thomas & Neupert, 1994; Brosius et al., 1998; Vernazza & Reeves, 1978). Figure 5.1 shows an  $m = 0$  image from frame 23, a 6 s exposure taken at  $\sim 18:50:22$  UT. The area in the box is displayed in figure 5.2. The explosive event, at  $\sim 100''$  E,  $180''$  N of disk center, consists of a bright core and two jets. A movie of *MOSES* frames (available on the supplemental CD as an extension of figure 5.2, see B.9) shows brightening of the core followed by the two jets shooting out from the opposite corners of the core. The event is visible for  $\sim 150$  s and was still in progress when the *MOSES* exposure sequence ended.

Figure 5.3 shows light curves calculated from data, without background subtraction, for each of the three regions, core, NW jet, and SE jet, along with the total light curve for all three regions. The light curves are the total intensity within the appropriate box shown in figure 5.4 for all 27 science exposures. Time is indexed from the beginning of the first exposure. The light curves show the core energizing before the jets. The event is not “winding down” at the time *MOSES* ceased data-taking. Indeed, it is not possible to say whether we observed even the middle of it. The uptick in total intensity in the last frame could indicate the beginning of a new phase in the event. The event time of 150 s must be taken as a lower bound.

Figure 5.5 shows a larger context around the event, with magnetic poles derived from MDI data and the position of a filament near the edge of the event. The “axis” of the event, as defined by the direction of the jets, appears roughly parallel to the filament. The sky-plane velocities shown in fig. 5.5 were calculated from centered differencing of the position of the center of each jet in frames 22 and 24 as shown in figure 5.6. The resulting sky-plane velocities are:  $v_{NW} = (12, 80)$  km s $^{-1}$ , and  $v_{SE} = (17, -70)$  km s $^{-1}$ . The  $+x$  axis is aligned with solar W and the  $+y$  axis with solar N. Also displayed in figure 5.5 is the MDI magnetogram closest in time to our launch,  $\approx 8$  minutes before the event starts. The magnetic poles labeled N47 and

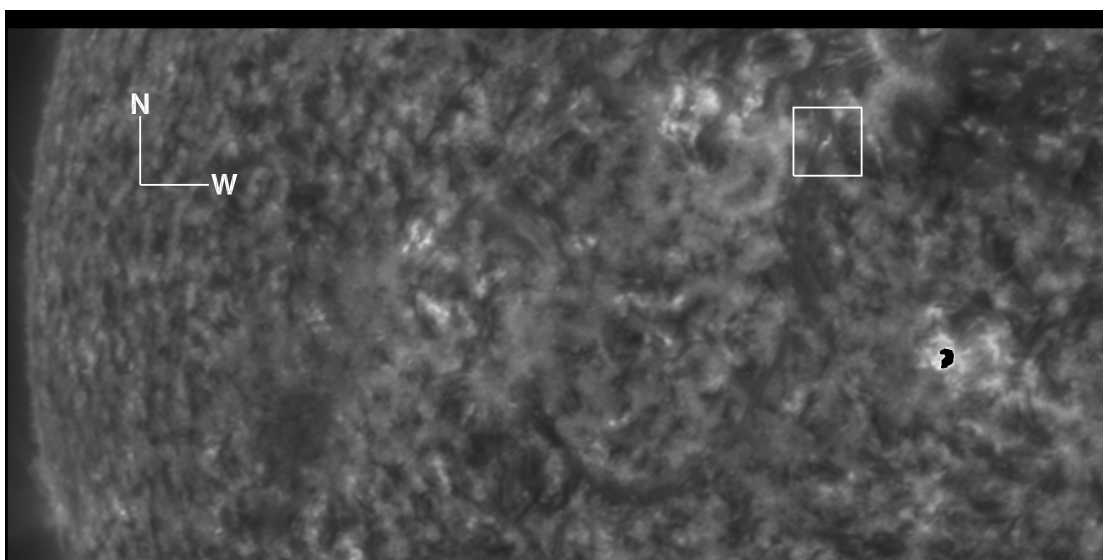


Figure 5.1: 6 s *MOSES*  $m = 0$  order image, taken 18:50:22 UT. The indicated area is shown expanded in figure 5.2. A bright feature near the SW corner of the image is saturated.

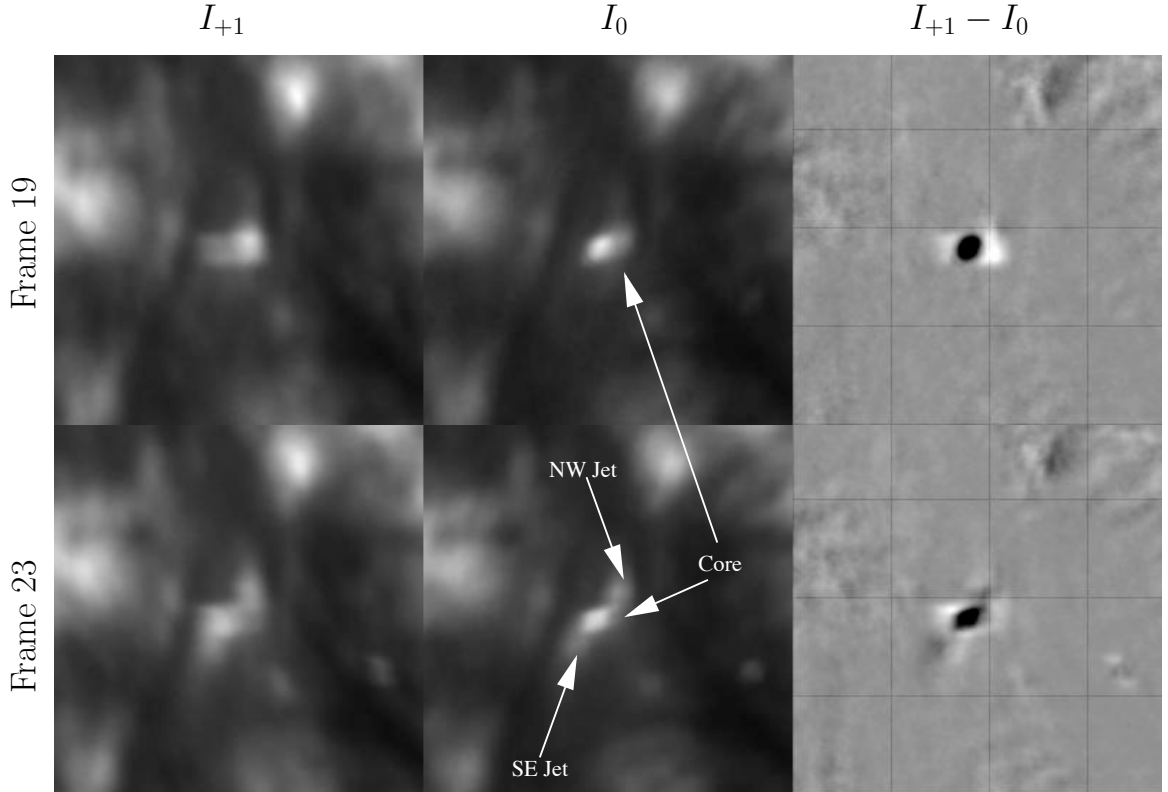


Figure 5.2:  $m = +1$  data at left,  $m = 0$  at center, difference image  $I_{+1} - I_0$  at right. The grid lines in the 3rd (difference) panel are  $20''$  apart. In the difference image white is positive, black is negative, and gray is near zero. The top frame is from  $\sim 18:49:15$  UT (3 s exposure) before the jets begin to emerge from the core. The bottom frame is from  $\sim 18:50:22$  UT (6 s exposure). At this point the jets are well-defined. This is the exposure analyzed in the rest of the chapter. These two image triples are from a movie of such triples, available on the supplemental CD, covering the entire flight data sequence from 18:45:54 UT to 18:50:50 UT. Orange pixels in the movie represent bad data.

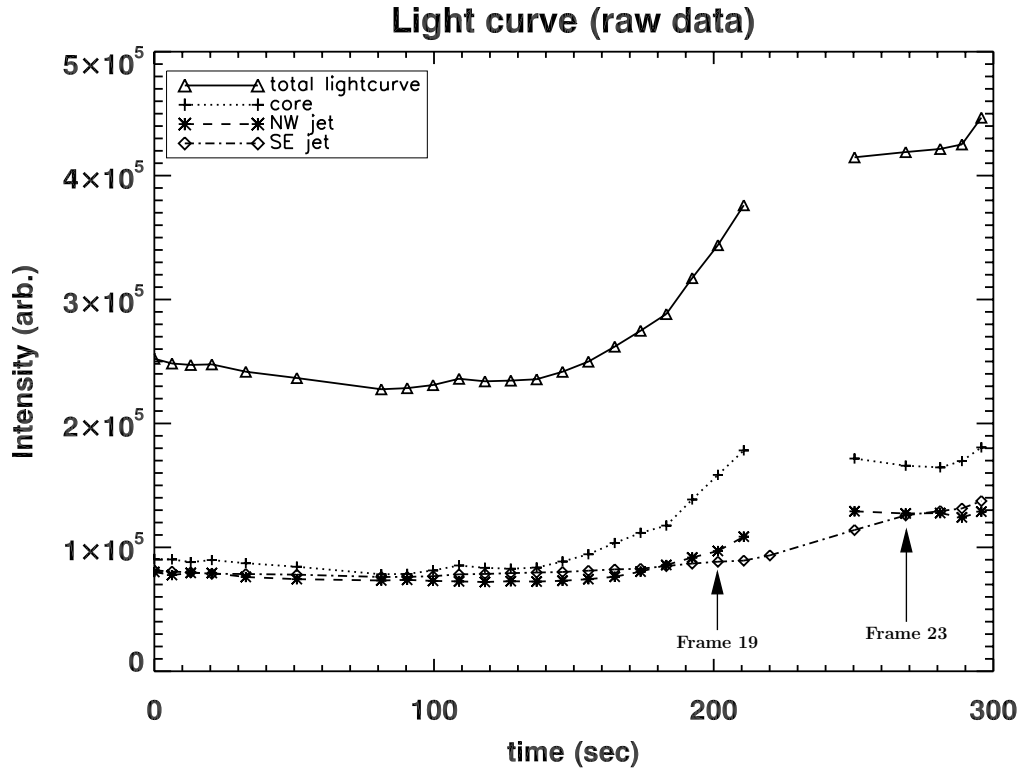


Figure 5.3: Light curve of the explosive event for the whole *MOSES-06* flight. Time is measured in seconds from the beginning of the first science exposure. The intensities for each exposure are assigned to the time at which that exposure began. The curves are calculated from data without background subtraction. The regions corresponding to NW jet, Core, and SE jet are shown in fig. 5.4. The missing point in the “total”, “core”, and “NW jet” curves (a 24 s exposure) is due to saturated pixels in the core and NW jet regions. Saturated pixels are marked as bad data and the sum is ignored when such pixels fall inside the regions-of-interest.

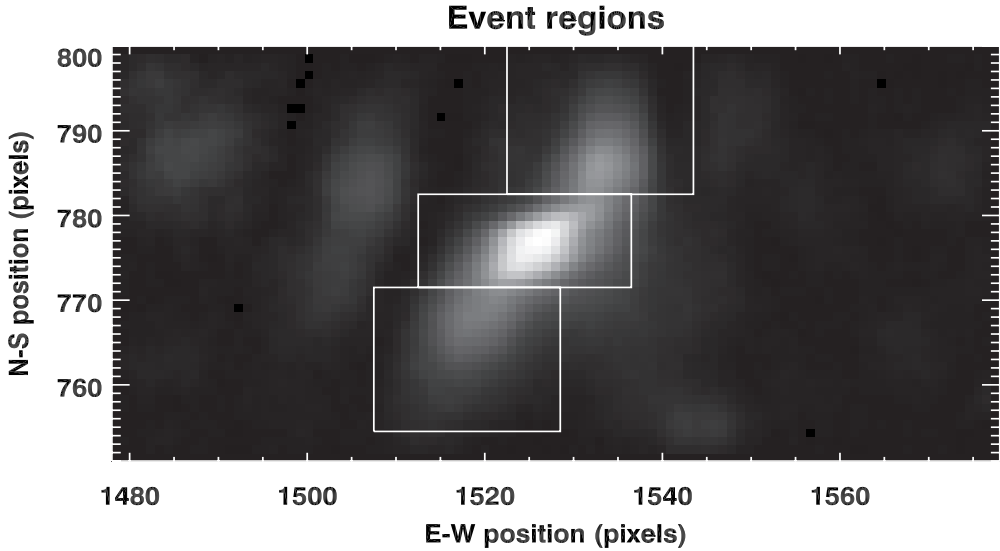


Figure 5.4: The regions-of-interest over which intensity totals were calculated for fig. 5.3. The regions are given by the boxes. The grayscale intensity is the  $m = 0$  order image from  $\sim 18:50:22$  UT with background subtracted to increase the contrast around the event for visual clarity. The light curves were calculated from unbackgrounded data. The three regions are contiguous.

P18 underly the explosive event. MDI magnetogram movies from the day of launch show that the poles are converging and canceling.

#### 5.4 Difference Images

The spectrally interesting features of the explosive event can be visualized quickly with a simple difference image. Figure 5.2 shows in the three lower panels the  $m = +1$  order data,  $m = 0$  order data, and the difference  $I_{+1} - I_0$  for the region immediately around the explosive event at  $\sim 18:50:22$  UT. From the difference image it is clear that the central bright feature of the explosive event is broadened, the SE jet is blue shifted, and the NW jet is slightly red shifted. The top set of panels in figure 5.2 shows the same field for an earlier time. No jets are yet visible, although the core

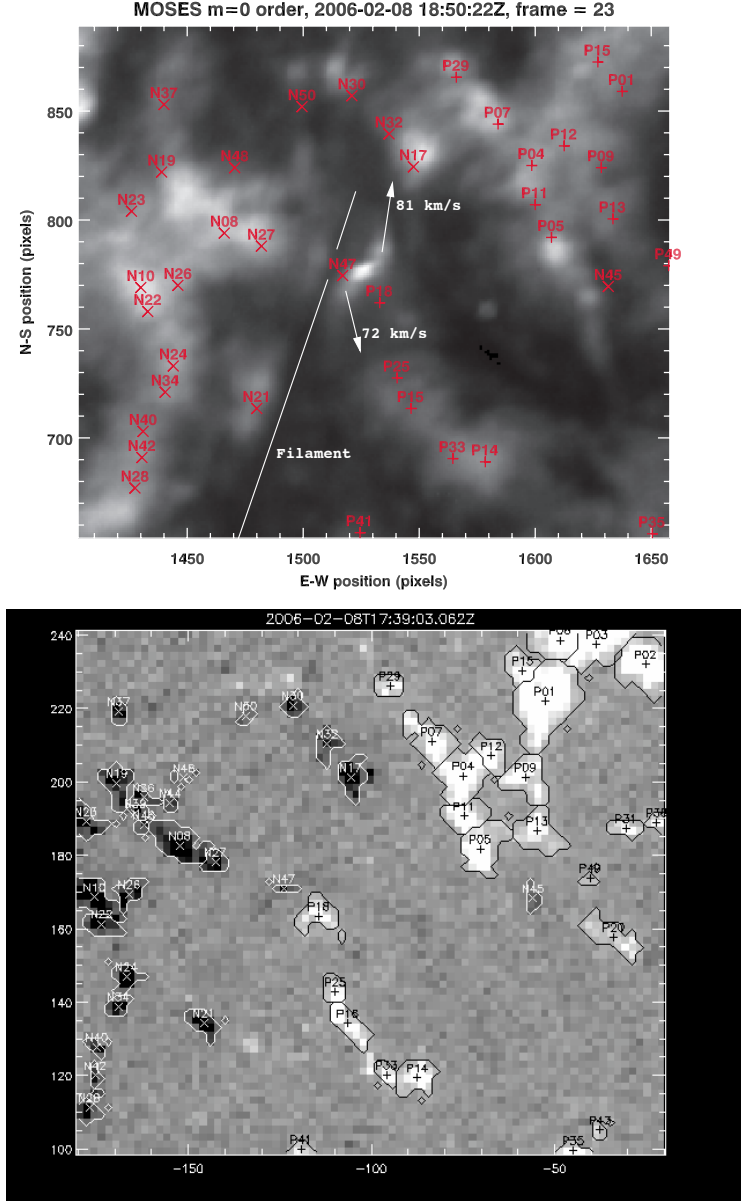


Figure 5.5: *MOSES* order  $m = 0$  on top, MDI magnetogram on bottom. Downhill gradients have been used to label flux concentrations. The magnetic centroids indicated in the MDI figure are shown on the  $m = 0$  image with their positions adjusted for the time difference between the images. The axes on the MDI figure are arcsec W and N of disk center. The image coordinates in this and following figures displaying *MOSES* data are pixel units ( $0.^{\prime\prime}6$ ) counted from the SE corner of the  $2048 \times 1024$  detector. Arrows on the *MOSES* image indicate the sky-plane flow directions of the two emerging jets. Note that they are roughly parallel to the nearby filament axis, but clearly are not collinear nor even anti-parallel to one another.

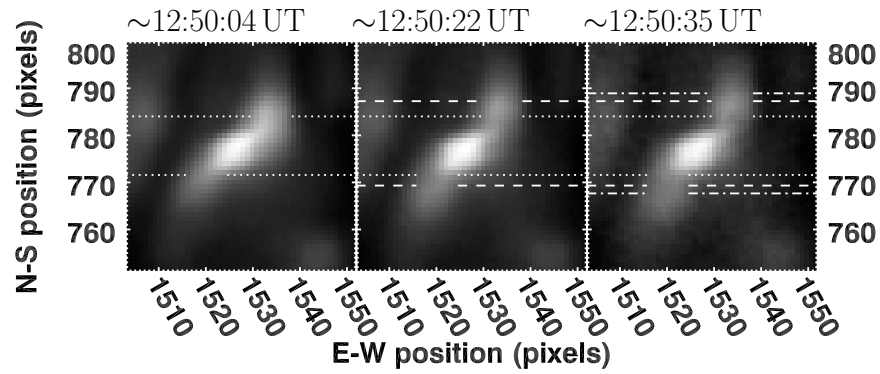


Figure 5.6: Three sequential  $m = 0$  images. 18:50:04 UT is a 12 s exposure; :22, 6 s; :35, 1.5 s. The image sequence shows the skyplane development of the two jets. These images were used to compute the skyplane velocities quoted in figure 5.5, from the centered difference of the jet positions shown by the dotted and dash-dotted lines. The dashed line shows the jet position in the central image analyzed in this chapter.

brightening and broadening is clear. These two sets of panels are extracted from a movie, showing the time evolution of the EE, which is available on the supplemental CD. It is also clear from the difference image that the event is visible in the He II line and is not a Si XI feature. The difference between He II and Si XI line centers amounts to a shift of  $\sim 17$  *MOSES* pixels between  $m = +1$  and  $m = 0$  orders. Such a large shift would be unmistakeable in the difference image.

## 5.5 Parallax Analysis

Because *MOSES* has no slit, spectral line information is inferred from differences between orders rather than observed directly. We expect full inversions of the *MOSES* data to provide line profile information for every pixel. Preliminary work along these lines has been encouraging and is reported elsewhere (Fox & Kankelborg, 2002; Fox et al., 2003; Kankelborg & Fox, 2004). Chapter 6 discusses the topic of inversions in detail. In this chapter, we perform a more direct analysis, which we call “parallax analysis”, that generates results independent of inversions. This type of analysis provides a check on future inversions and also generates a target list for such inversions.

As demonstrated schematically in figure 5.7, a compact bright source which is shifted in wavelength (blue and red dots) jumps in position relative to a background at fixed wavelength when viewed in  $m = +1$  or  $m = -1$  orders. This is directly analogous to parallax. Compact sources which exhibit parallax when comparing two spectral orders (viewing angles) imply a doppler shift. The displacement of a bright source from one order to another can be measured to infer the doppler shift. In a similar fashion spectral line broadening (oblong white dot in figure 5.7) results in an elongation in the dispersion direction in any non-zero order image.

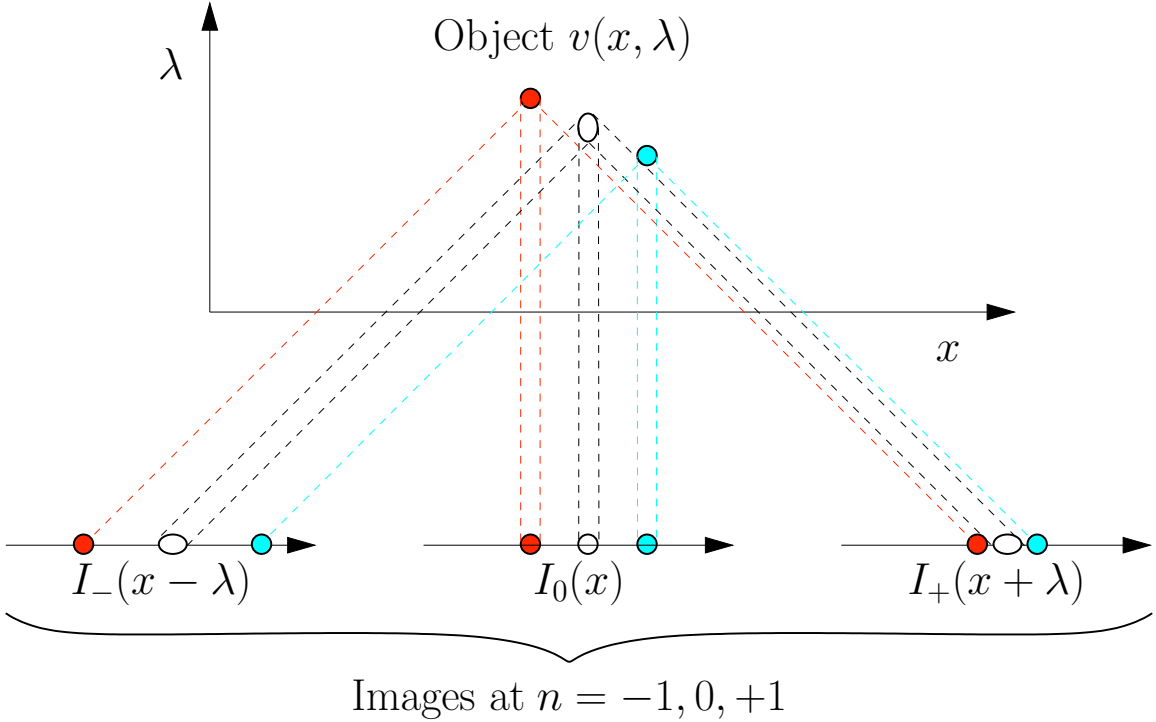


Figure 5.7: A revisit of the diagram from figure 2.2 on page 13 schematically representing parallax analysis. The orders are indicated as well as the FOV and Passband domains  $F$  and  $B$ . Several bright compact sources are shown, demonstrating the appearance in both the hyper-spectral cube and the various data orders of a redshift, blueshift, and a broadening. For coaligned data the expected location in  $m = \pm 1$  of a source at the central wavelength would be the same as the position of the bright source in the  $m = 0$  image. The parallax between  $m = 0$  and  $m = \pm 1$  orders gives the magnitude and direction of the shift.

### 5.5.1 Procedure

During its 2006 flight the *MOSES* dispersion direction was closely aligned to solar E-W. We refer to this as the “ $x$  axis”. Solar N-S is called the “ $y$  axis”. Figures 5.8 - 5.13 illustrate our procedure for computing the inferred doppler shifts, which is as follows:

1. Subtract a “soap-bubble” background from the data, so-called because it mimics the behavior of a soap-bubble: it solves Laplace’s equation within some

boundary which is held fixed. This background is derived from a modified point-relaxation method, first described and used in Kankelborg et al. (1996) and Kankelborg et al. (1997). The data are pre-filtered using a sigma filter. The boundary pixels are held fixed and at each relaxation step any pixel values which *increased* due to relaxation are reset to their original (sigma-filtered) values (note Kankelborg et al., 1997, appendix D states that interior pixels are only allowed to relax upward; this statement is in error). This has the effect of fixing interior local minima as well as the boundary, as though the data have “weight” and are resting on the surface of the bubble, holding it down where they touch. We use this method on the  $m = 0$  order data and subtract the resulting background from both  $m = 0, +1$ . The backgrounds for three sample  $y$  values are shown in figures 5.8, 5.10, and 5.12, along with the raw  $m = 0, +1$  data. From these examples it is clear that the  $m = 0$  background is sufficient for both orders.

2. Fit slices of constant  $y$  with up to 4 gaussians. One gaussian may not provide a sufficiently close fit to the explosive event data in either order. Figures 5.9, 5.11, and 5.13 show examples of background subtracted data and gaussian fits for the same three  $y$  axis values. We used the Levenberg-Marquardt method of least-squares parameter estimation as implemented by William Thompson in the routine lstsq.pro from *SolarSoft* (Freeland & Handy, 1998). A detailed description of the Levenberg-Marquardt method may be found in “Numerical Recipes in C” (Press et al., 1992).
3. Interpret changes in a feature’s position between  $m = +1$  and  $m = 0$  images as a doppler shift of magnitude equal to the position difference multiplied by

the *MOSES* reciprocal dispersion of  $29 \text{ km s}^{-1} \text{ pixel}^{-1}$ . Similarly differences in feature width between images imply doppler broadening.

4. Generate composite positions (centroids) and composite widths for purposes of comparison between orders using the formulas

$$\mu_T = \frac{\sum_i \mu_i I_i}{\sum_i I_i}, \quad (5.5)$$

$$\sigma_T^2 = \frac{\sum_i I_i [(\mu_i - \mu_T)^2 + \sigma_i^2]}{\sum_i I_i}. \quad (5.6)$$

The integrated intensity of the  $i$ th gaussian is denoted by  $I_i$ , the mean by  $\mu_i$ , and the variance by  $\sigma_i^2$ .

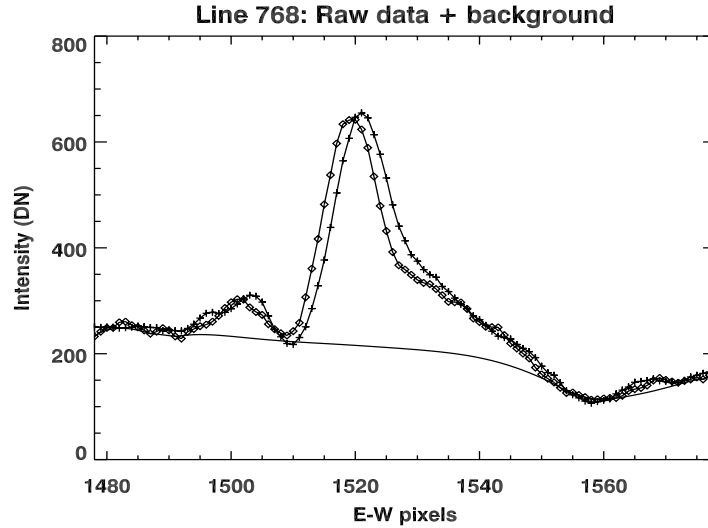


Figure 5.8: Raw data for  $m = 0$  (diamonds) and  $m = +1$  orders (pluses), line 768, with background shown by the unbroken line. These data are from the SE jet.

IDL code which implements this procedure is included on the supplemental CD (see B.10).

The interpretation of the data is often complicated. Single gaussian peaks in  $m = 0$  order can split into two resolved peaks in  $m = +1$  order, one to red and one to blue.

A good fit to the  $m = 0$  order data for the explosive event may require two or more gaussians. These gaussians may change in completely separate ways in  $m = +1$  order. A fit to the explosive event may blur at the boundary with a weak, but wide gaussian fit to some intensity which is not part of the event. Our best judgment has been used in determining which gaussians belong to the event and how to treat the various parallax phenomena we see in the data. Our decisions are based on the overall appearance of the event, the spatial smoothness of the fits along the  $y$  axis (across slices), the confidence level of the fits, and the temporal variation of the data. We calculate, for each order, the squared-sum of the residuals  $R^2 = \sum(I_{fit} - I)^2$  and compare it to the total variance of the data  $V = \sum I^2$ . Here  $I$  denotes the background-subtracted data and  $I_{fit}$  is the total fit (the “model”, including all fitted gaussians). The sums are performed over all image pixels in a given row. We do not use any fits which have  $R^2/V > 0.05$ . Nearly all fits are well below this threshold. None of the accepted fits were close to the 5% level. The fits which do not meet this threshold are located on the north and south edges of the event region. Visual inspection clearly establishes that they are bad fits, and the data in those areas are not well described by gaussian functions. Therefore the analysis is not sensitive to the choice of 5% as a maximum residual level. Dividing  $R^2$  by the number of degrees of freedom,  $N_{pixels} - N_{parameters}$ , gives an estimate of the error  $\sigma_I^2$  in the pixel intensity (note that this presumes a good fit, with  $\chi^2 = 1$ ). This value of  $\sigma_I$  (a constant for each slice) should be an over-estimate. Feeding it to the Levenberg-Marquardt routine allows the calculation of the errors in the fit parameters, which should likewise be over-estimates (see the discussion in Press et al., 1992). The “confidence level of the fit”, as we have used that term here, means the confidence with which we exclude the zero intensity null hypothesis. Each gaussian fit produces, among other parameters, the total integrated intensity in the gaussian,  $G_{total} \pm \sigma$ . When  $G_{total} < 3\sigma$  we cannot conclude with high

confidence that adding that gaussian to the fit is better than leaving it out (i.e. the total integrated intensity in that gaussian is not significantly different from zero). In such cases we revert to a fit with a smaller number of gaussians. For a few fits we have accepted confidence levels slightly less than  $3\sigma$  when doing so seemed justified by the spatial relationship to more confidently fitted Gaussians in adjacent  $y$  slices.

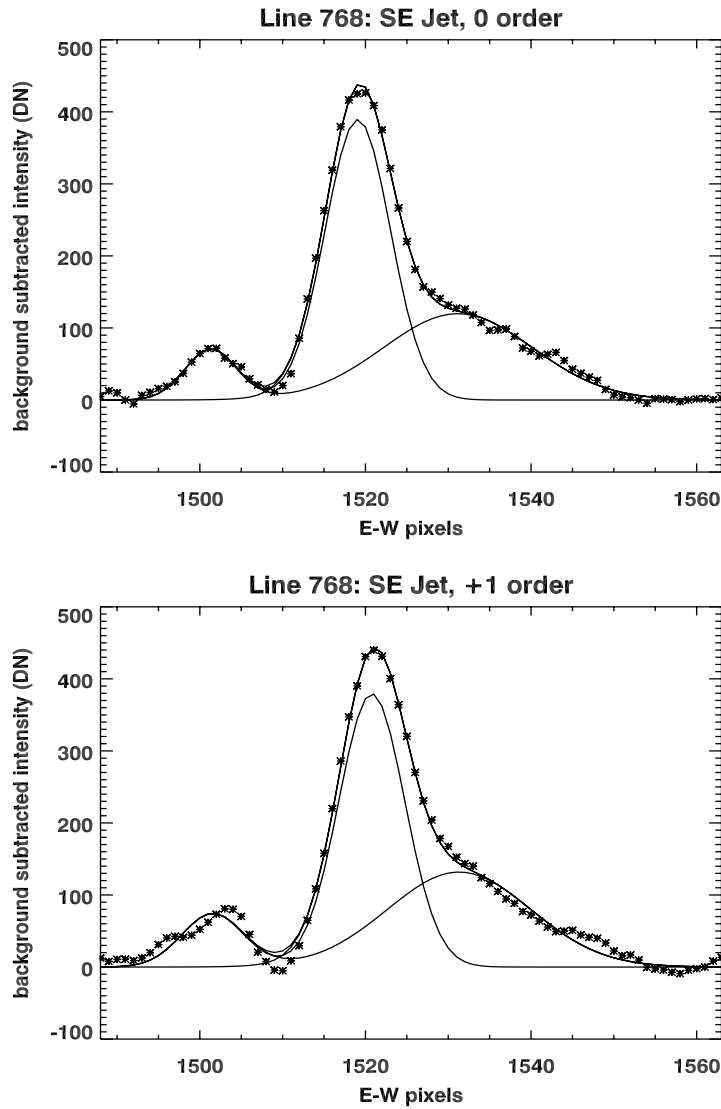


Figure 5.9: Background subtracted data for line 768 with Gaussian fits overlaid for  $m = 0$  order (top) and  $m = +1$  order (bottom). The strongest Gaussian peaks indicate a blueshift.

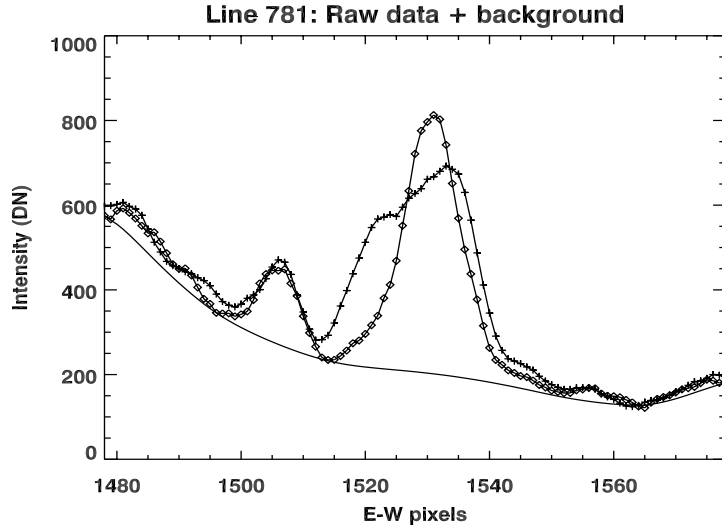


Figure 5.10: Raw data for  $m = 0$  (diamonds) and  $m = +1$  orders (pluses), line 781, with background shown by the unbroken line. These data are from the event core.

## 5.6 Results

The explosive event analyzed here exhibits 3 distinct regions: a bright core with non-thermal broadening (characterized by separate blue-shifted and red-shifted components), a blue-shifted jet to the SE of the core, and a red-shifted jet to the NW. Representative slices perpendicular to the  $y$  axis have been taken from each of these three regions and are displayed in figures 5.8 - 5.13. Each slice shown in figures 5.8, 5.10, and 5.12 gives the sense of the doppler behavior of each corresponding region by directly comparing raw  $m = +1$  and  $m = 0$  data. The background found for the  $m = 0$  order from the modified point-relaxation method described in section 5.5.1 is also shown. Associated with each raw data plot are plots (figs. 5.9, 5.11, and 5.13) showing the background subtracted data and the gaussian fits. Full details of all fit parameters are listed in table 5.1. The statistical confidence in excluding the zero intensity null hypothesis for the fits is also given in table 5.1. The confidence

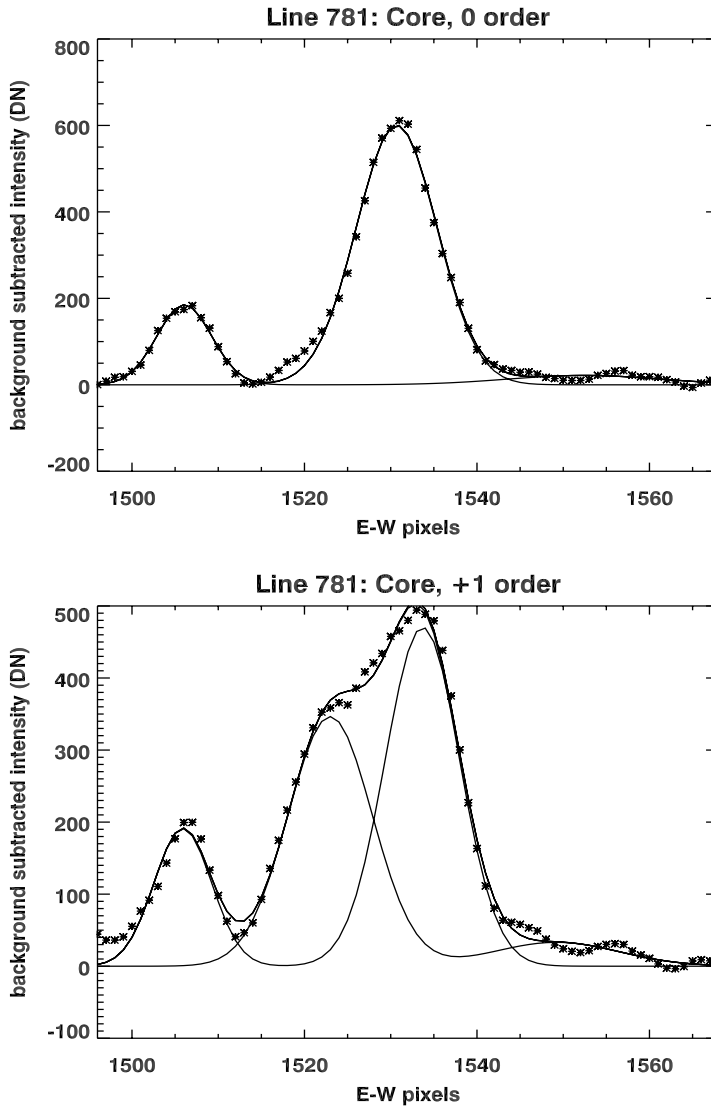


Figure 5.11: Background subtracted data for line 781 with Gaussian fits overlaid for  $m = 0$  order (top) and  $m = +1$  order (bottom). The strongest Gaussian peak in  $m = 0$  is in the core. In the  $m = +1$  order this single peak appears to split into clearly resolved double peaks, one to the red, and one to the blue. We take this splitting to indicate the non-thermal broadening in the core of this event is due to a two-component doppler shift with both a blue and red component.

in excluding the zero doppler shift null hypothesis is not given explicitly but can be estimated from the fit positions and associated errors.

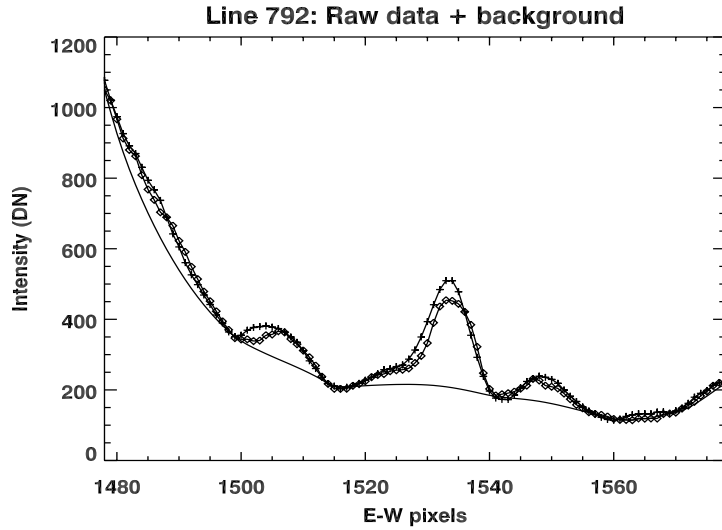


Figure 5.12: Raw data for  $m = 0$  (diamonds) and  $m = +1$  orders (pluses), line 792, with background shown by the unbroken line. These data are from the NW jet.

Figure 5.14 shows a  $60'' \times 30''$  region around the event from the same frame as figure 5.5 with  $m = 0$  order displayed in grayscale and gaussian fit parameters overlayed in color. Fits were only made to data that fell between the solid (dotted) white lines for  $m = 0$  ( $m = +1$ ). These lines are called “fit limits” in the figure legend. The symbols mark the centroid position of each fit. Offsets between  $+$  and  $\diamond$  symbols are doppler shifts, with a 1 pixel =  $29 \text{ km s}^{-1}$  scale. The colored lines show the FWHM of each gaussian. The color of the symbols and lines gives the peak gaussian intensity. Widths and shifts are largely consistent from each  $y$ -slice to the next. It is possible from this analysis to form a coherent picture of the event in position and velocity space.

Figure 5.15 graphs the inferred doppler shift derived from gaussian fits whose centroids fell between the dashed bars in fig. 5.14 (called “centroid limits” in the legend

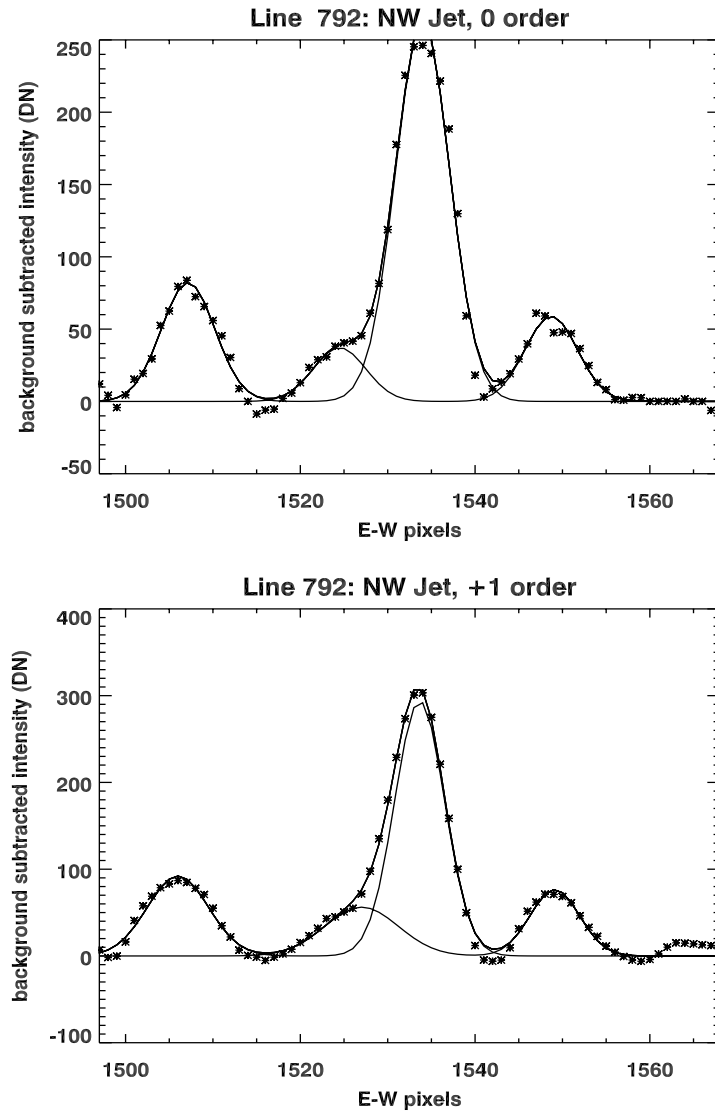


Figure 5.13: Background subtracted data for line 792 with Gaussian fits overlaid for  $m = 0$  order (top) and  $m = +1$  order (bottom). The strongest Gaussian peaks are located in the NW jet and show a slight, but significant redshift.

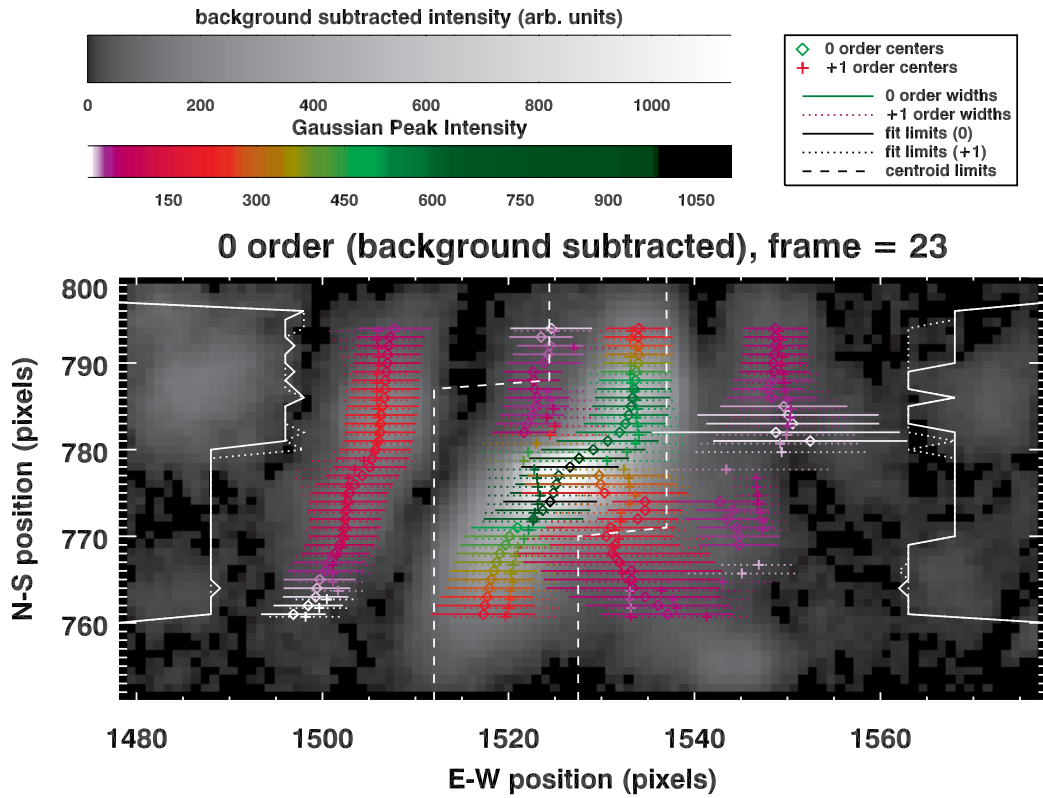


Figure 5.14: *MOSES* 6 s exposure, frame 23, taken at 18:50:22 UT,  $m = 0$  in grayscale with gaussian parameters indicated by the colored symbols and bars. As before, diamonds are for  $m = 0$  order, pluses for  $m = +1$  order. The position of a symbol shows the location of the associated gaussian fit. The symbol color gives the peak intensity of the gaussian. The colored line is the FWHM. Solid lines are FWHM for  $m = 0$  order, dashed lines are for  $m = +1$  order, and are slightly offset downward for clarity. Dispersion is  $29 \text{ km s}^{-1}$  per pixel. Plate scale is 440 km per pixel.

Table 5.1: Fit data for the three cases shown in figs. 5.8 - 5.13. Gaussian centers and widths are given in pixel units. Intensity in this context means the total integrated area under the gaussian curve. The term “null confidence” refers to the zero intensity null hypothesis and is defined in the text.

		Center (pix.)	Width (pix.)	Intensity ( $\text{DN s}^{-1}$ )	Null Conf. ( $\sigma$ )
Line 768 (SE Jet)	$m = 0$	$1501.34 \pm 0.20$	$7.33 \pm 0.47$	$554 \pm 46.0$	12.0
		$1519.08 \pm 0.05$	$9.28 \pm 0.21$	$3860 \pm 143$	27.0
		$1531.17 \pm 0.82$	$21.1 \pm 1.34$	$2700 \pm 187$	14.5
	$m = +1$	$1501.57 \pm 0.34$	$8.80 \pm 0.80$	$698 \pm 81.2$	8.6
		$1520.77 \pm 0.08$	$9.39 \pm 0.41$	$3810 \pm 301$	12.6
		$1531.3 \pm 1.5$	$20.4 \pm 2.2$	$2870 \pm 354$	8.1
Line 781 (Core)	$m = 0$	$1506.07 \pm 0.14$	$7.48 \pm 0.33$	$1480 \pm 86.6$	17.1
		$1530.68 \pm 0.07$	$11.0 \pm 0.15$	$7040 \pm 120$	58.6
		$1552.5 \pm 2.5$	$20.9 \pm 7.2$	$484 \pm 196$	2.5
	$m = +1$	$1505.90 \pm 0.16$	$7.84 \pm 0.38$	$1600 \pm 99$	16.2
		$1522.97 \pm 0.49$	$11.5 \pm 0.79$	$4240 \pm 340$	12.6
		$1533.65 \pm 0.29$	$10.2 \pm 0.60$	$5080 \pm 380$	13.3
		$1549.2 \pm 2.8$	$17.1 \pm 6.0$	$607 \pm 233$	2.6
		$1507.16 \pm 0.18$	$7.23 \pm 0.42$	$635 \pm 49.1$	12.9
Line 792 (NW Jet)	$m = 0$	$1524.48 \pm 0.58$	$7.09 \pm 1.37$	$281 \pm 63.0$	4.5
		$1534.00 \pm 0.08$	$7.29 \pm 0.20$	$2050 \pm 65.1$	31.5
		$1548.72 \pm 0.25$	$7.08 \pm 0.59$	$445 \pm 49.0$	9.1
		$1505.99 \pm 0.16$	$8.27 \pm 0.37$	$813 \pm 47.7$	17.1
	$m = +1$	$1527.0 \pm 2.0$	$9.9 \pm 2.7$	$596 \pm 197$	3.0
		$1533.66 \pm 0.17$	$6.74 \pm 0.26$	$2120 \pm 201$	10.5
		$1549.12 \pm 0.17$	$6.68 \pm 0.40$	$545 \pm 42.6$	12.8

for figure 5.14). The dashed bars were chosen so as to exclude from consideration fits to intensity that are clearly not part of the event, such as the linear object extending from  $1490 < x < 1510$  and  $760 < y < 795$  on the other side of the filament channel from the EE, or the weak intensity from 1540 to 1560, while still including fits that might reasonably be associated with the event. The solid line in fig. 5.15 shows the composite doppler shifts in the event core from  $y = 775$  to  $y = 781$  using intensity-weighted centroids found by means of eq. 5.5. The figure also shows doppler velocities calculated by interpreting the gaussian splitting as separate blue-ward and red-ward velocity components. Two fit behaviors are seen in this region. The first behavior,

what I call [1, 2] component fits, the  $m = 0$  intensity is well-fit by a single gaussian, while the  $m = +1$  intensity has two resolved gaussians, one to each side of the  $m = 0$  fit. See fig. 5.11 for an example of this behavior. The two doppler velocities are calculated by subtracting the  $m = 0$  centroid from each  $m = +1$  centroid. The second fit behavior, called [2, 2] component fits, are characterized by  $m = 0$  intensity requiring two gaussians for a good fit. In  $m = +1$  these two gaussians are seen to spread apart from one another relative to their  $m = 0$  positions. These doppler velocities are calculated by subtracting the nearest  $m = 0$  centroid from each  $m = +1$  centroid. These fit behaviors show the non-thermal nature of the line broadening in the core. Thermal broadening could not cause a single gaussian to split into two in the  $m = +1$  order. The  $m = +1$  fit would contain a single gaussian with a larger width than the  $m = 0$  gaussian. Refer to figure 5.7. Likewise in [2, 2] component fits, the  $m = +1$  order fits would be wider than the  $m = 0$  order fits (and both by the same amount at that), but they would not be shifted in opposite directions. The error bars in figure 5.15 are derived from the first moment fit errors and represent  $1-\sigma$  errors. Like the errors in the fit parameters they are over-estimates, particularly since the normal quadrature summation used in error propagation is only valid for statistically independent variables, and our fit parameters are likely anti-correlated. The large jumps in the size of errors seen in the figure indicate where the dashed bars (fig. 5.14) pick up (or drop) multiple gaussians. Compositing multiple gaussians greatly amplifies the fit errors.

Figure 5.16 shows the inferred doppler broadening calculated by subtracting the  $m = 0$  composite width (from eq. 5.6) from the  $m = +1$  composite width in quadrature. Both widths are scaled by a factor of 2.3548 for comparison to FWHM linewidths. As in figure 5.15 the composite widths are calculated only for fits with centers falling between the dashed bars in fig. 5.14. The doppler width in the core

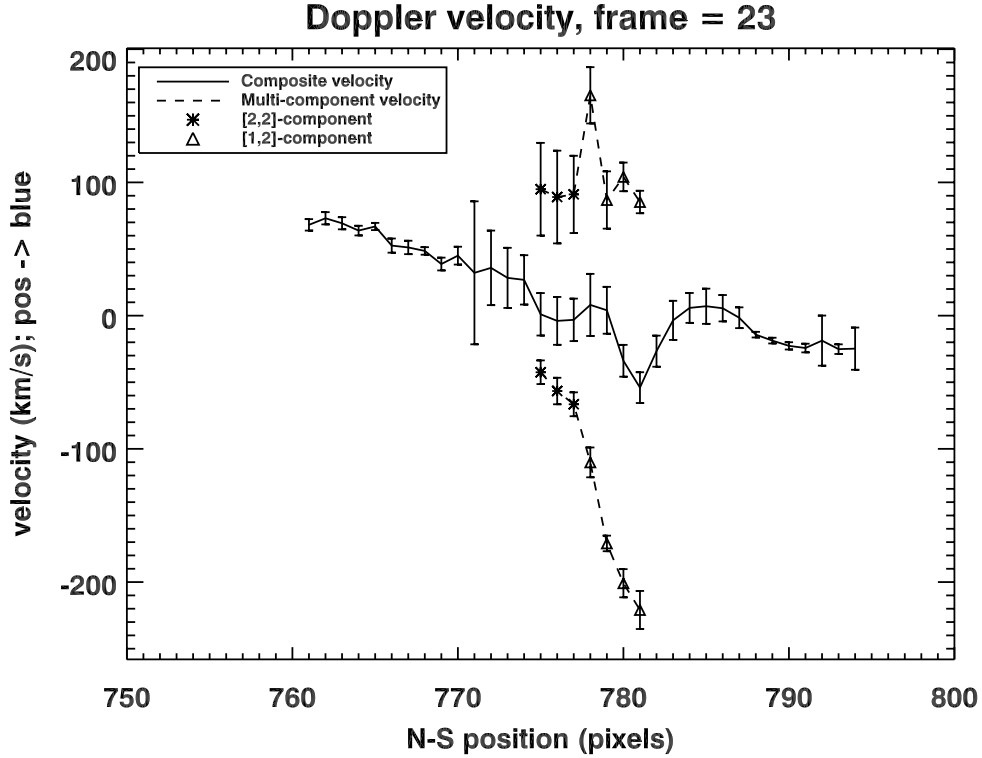


Figure 5.15: Doppler shift as a function of  $y$  axis position. Composite centroids of the event core are calculated using eq. 5.5. Multi-component shifts are calculated in the explosive region where the  $m = +1$  order broadening can be resolved into separate gaussians. [1,2]-component shifts show single-fit to double-fit shifts; that is, splitting of a single  $m = 0$  gaussian into two oppositely directed gaussians in  $m = +1$ . [2,2]-component shifts have two-gaussian fits in  $m = 0$  which spread apart when viewed in  $m = +1$ .

is non-thermal. Our instrumental linewidth has not been measured, however the  $\sim 50 \text{ km s}^{-1}$  median width seen in the jets is an upper bound. The maximum doppler width is  $380 \text{ km s}^{-1}$  FWHM at pixel location (1527, 779) close to the peak intensity in the event. This width, and the other widths in the core well in excess of  $100 \text{ km s}^{-1}$ , are much too large to be thermally derived, given the He II thermal width of  $30 \text{ km s}^{-1}$  FWHM (Andretta et al., 2000). As in figure 5.15 the error bars are calculated from the fit parameter errors. Some of the errors are (very obviously) spuriously large.

These again occur at the places where the centroid limits (dashed bars in fig. 5.14) first pick up multiple gaussians. These new gaussians are far from the gaussians in the main body of the EE, with weaker intensity, and large fit errors, contributing to a high error estimate. Points which appear without error bars are identically zero, and show where we have fits in  $m = 0$  order which are slightly *wider* than the corresponding  $m = +1$  order fits, giving an imaginary inferred doppler width.

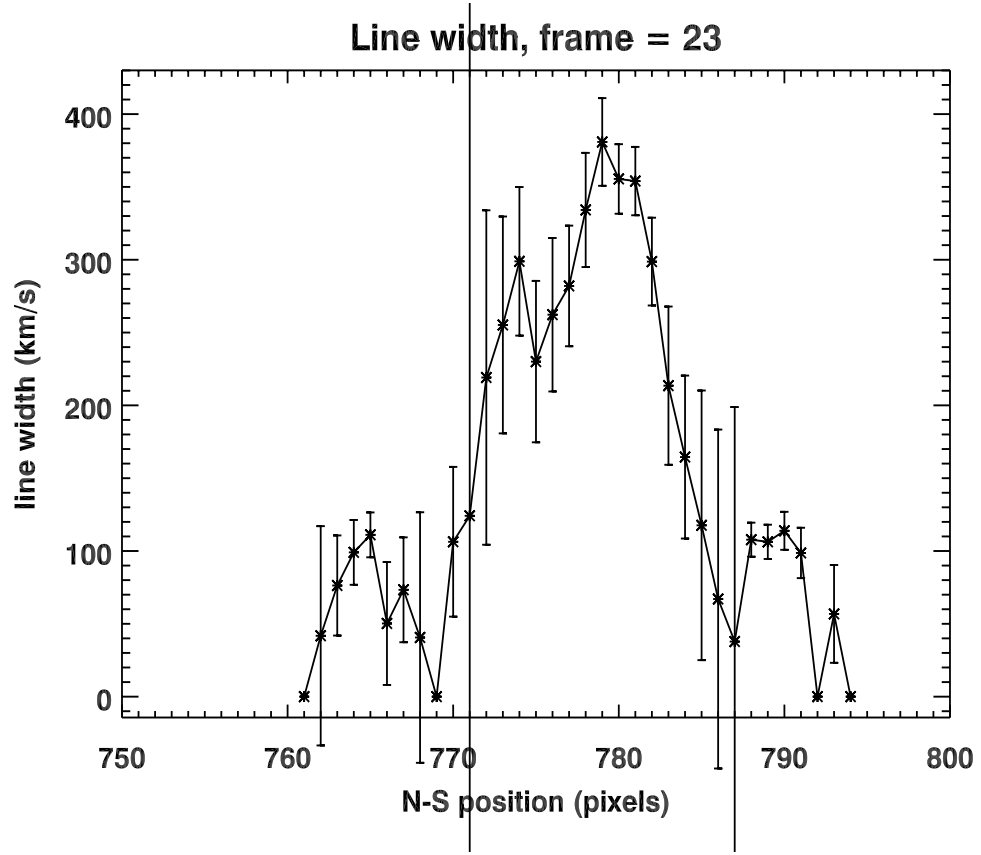


Figure 5.16: Inferred line width calculated from the quadrature difference of composite width from  $m = 0$  to  $m = +1$  as a function of  $y$  axis position. Composite widths are defined and calculated in a standard-deviation sense in eq. 5.6 but are scaled to FWHM in the figure and as quoted in text.

Between these three figures we can identify the major components of the event as follows:

- The core, approximately 4000 km E-W by 4800 km N-S, extends across pixels  $1523 < x < 1532$  and  $772 < y < 783$ . It is characterized by an increased doppler broadening as shown in fig. 5.16 and a clearly resolved bi-directional doppler shift shown in fig. 5.15. The locations of maximum blue- and redshift components are offset 1300 km in the  $y$  direction and 1800 km in the  $x$  direction.
- The jets, each  $\approx 6000$  km in length, by contrast have little or no broadening and show only a one-sided doppler shift. They are offset from each other in the E-W direction about  $\approx 5700$  km.
- The SE jet has a large blue doppler shift, peaking at  $70\text{-}80 \text{ km s}^{-1}$ , comparable to its skyplane velocity (see sec. 5.3). Taken together these measurements imply a total velocity of  $\approx 104 \text{ km s}^{-1}$  at an angle to the plane-of-the-sky of  $46^\circ$ .
- The NW jet red-shift is smaller, at about  $20\text{-}30 \text{ km s}^{-1}$ . However, its sky-plane velocity is somewhat larger. The total velocity is  $\approx 86 \text{ km s}^{-1}$  at an angle with respect to the sky of  $20^\circ$ .
- “Crossover points”, locations where the sign of the jet doppler shift appears to change, can be seen in fig. 5.14 at  $(1523, 772)$  and  $(1533, 786)$  where the jets merge with the core.
- The 3-D velocity vectors in the jets are,

$$v_{NW} = (12 \pm 10.2, 80 \pm 13.8, -25 \pm 5) \text{ km s}^{-1}$$

$$v_{SE} = (17 \pm 10.3, -70 \pm 10.6, 75 \pm 5) \text{ km s}^{-1},$$

giving an angle of  $145.7^\circ \pm 6.9^\circ$  between the jets. The  $+x$  direction is solar W,  $+y$  is solar N, and  $+z$  is toward the observer. The velocity errors for the line-of-sight component are taken from figure 5.15. Those for the components

transverse to the line-of-sight are estimated from our visual estimate of the sky-plane jet positions, which was repeated three times using different image scaling. The quoted errors correspond to somewhat more than 0.5 pixel deviations in sky-plane position in each of the exposures used to compute the center-difference sky-plane velocity (see sec. 5.3, figs. 5.5, 5.6). The error in the angle between the jets is calculated from the velocity component errors via monte-carlo simulation. The jet-angle histogram resulting from the simulation is nearly gaussian, so the “ $\pm$ ” notation has the usual meaning. We also use monte-carlo simulation to calculate the confidence in excluding the anti-parallel jets null hypothesis. This is done by adjusting the jet velocities to force a  $180^\circ$  angle while holding the magnitudes constant and, applying the same velocity errors as above, asking the question “what fraction of simulated velocity measurements yield an angle of  $145.7^\circ$  or less?” The geometry of this null hypothesis can be constructed in a variety of ways, but in each of 13 cases tested the confidence is about 99.9%, therefore we conclude the data are not consistent with antiparallel jets.

### 5.7 Discussion and Conclusions

The He II event observed by *MOSES*-06 has all the features of a transition region explosive event, and is within the upper range of EE parameters, such as size, lifetime, doppler velocity, maximum broadening, etc., found in previous observations of EEs, as cited extensively in section 5.1. It lies above a pair of converging, canceling magnetic poles. This suggests reconnection as a mechanism. The jets are expelled from the core with velocities of the order of transition region Alfvén velocities, a further suggestion of reconnection. The doppler shifts derived in sec. 5.6 show that the material is actually moving and rules out the hypothesis that the sky-plane velocities are only

the apparent motion of plasma heating/cooling progressively outward through the He II band. EEs have been previously explained by a 2-D *X*-point reconnection model (see for example Innes et al., 1997, fig. 2b). That model predicts opposing collinear outflow jets. We see non-collinear jets, offset by 5700 km, which corresponds to the entire width of the core. Furthermore, the jets are not anti-parallel, with an angle of 146° between their flow directions.

Reconnection is a localized phenomenon. The velocities of reconnection jets need not be anti-parallel (although the cartoons are usually drawn that way) but they should have a common origin. We should be able to trace them back to an intersection where the reconnection which produced them occurred. We cannot do that here. We do not know what kind of reconnection process can produce jets which appear to be so far apart. One hypothesis is that the jets we see are not the jets of a single reconnection but are produced by separate reconnection events. We might interpret the noted crossover points as the source of each reconnection. In that case, the following questions occur: Where is the other half of each jet? Why are the velocities heading into the core (presumably a region of higher density and temperature) higher than the velocities heading away from the core? What processes associate the reconnections with each other? Does one reconnection “trigger” the other? The Alfvén crossing time of the core is  $\approx 60$  s yet the two jets appear simultaneously in our observations. Are both jets triggered by a preceding reconnection event in the core? What physical property provides the time coincidence of the jets? These considerations lead us to prefer the simpler idea of a single reconnection event, though a self-consistent interpretation has so far proved elusive.

It is also hard to see how a “near” potential field configuration could give rise to this kind of geometry (compare Longcope, 1998). The presence of a filament nearby has been noted in figure 5.5. We suspect this filament strongly influences the structure

of the EE analyzed here. Filaments are associated with highly non-potential fields. One of the underlying magnetic poles (N47) is also coming from the region of the filament (see fig. 5.5 on page 89). Furthermore, N47 is a minority polarity as it is on the positive side of the filament.

Our observation of this event's 3-D structure and dynamics is only possible because of the simultaneous imaging and spectroscopy provided by *MOSES*. With only an imager we would not know this is a transition region explosive event. With a slit spectrometer we would have missed pieces of the full event, perhaps only seeing one of the jets, or only the core, depending on slit alignment, and would not have observed the peculiar, non-collinear geometry of the jets.

We gratefully acknowledge the assistance of Dana Longcope in obtaining and understanding the magnetic context data.

CHAPTER 6  
 DATA INVERSION FOR THE MULTI-ORDER SOLAR EXTREME  
 ULTRAVIOLET SPECTROGRAPH

To recover the source spectrum from *MOSES* data an ill-posed inversion must be performed. I have explored several techniques by which this may be accomplished, using them to invert simulated data (where the true spectrum is known before-hand). Two of those, Fourier backprojection and Pixon reconstruction, constrained by the spatially integrated spectrum of the Sun, will be described in this chapter. Both methods produce good results, including doppler shifts measured to  $\frac{1}{3}$ -pixel accuracy. The Pixon code better reproduces the line widths.

I will also describe similar results achieved with the Smooth Multiplicative Algebraic Reconstruction Technique (SMART), invented by Charles Kankelborg. I have used the SMART technique to invert a section of flight data, including the explosive event analyzed in chapter 5. With the results of chapter 5 as a baseline we can compare the performance of the SMART algorithm on real data to what we already know about this source.

In the following sections I will give a description of two of the inversion techniques I studied, Fourier backprojection (§6.1.1) and Pixon reconstruction (§6.1.2), and the results of trial inversions performed on test data from the *SERTS-95* experiment (Brosius et al., 1998, 1999). §6.1.3 describes the SMART algorithm and compares it to the other two algorithms. SMART was ultimately used to invert a section of *MOSES* flight data. That inversion is shown in §6.3. The results are qualitatively and quantitatively commensurate with what we find in chapter 5 except for systematic velocity underestimation in the SMART reconstruction. Such systematic error is common to tomographic reconstruction methods.

### 6.1 Inversion of Simulated Data

We have studied several inversion methods on simulated test data, where we can compare our reconstructed cube to the real one to determine how accurately we recover it by a given technique. We use data from the *SERTS-95* sounding rocket mission, provided by Roger J. Thomas for our test cube. The *SERTS* mission is a slit spectrograph of high spectral resolution which uses image intensifier tubes to amplify the EUV signal. We have extracted a sample of *SERTS* data in a narrow region similar to the *MOSES* passband, and scaled the data to the expected count rate for *MOSES*. This results in a 2-D cube, with the  $x$  axis corresponding to distance along the *SERTS* slit, and 1-D simulated data functions. The data functions are produced using the projection equation eq:projections. After projection the correct amount of poisson noise is added.

For the purposes of study of simulated spectra we have used the *actual*  $\infty$  order from *SERTS-95* test data. The  $\infty$  order data have noise added with the same statistical character as the “observed” data before passing to the inversion procedure. We plan to investigate systematically the sensitivity of the inversion to the  $\infty$  order in the future.

Other common heuristics have been used in addition to our infinite order heuristic. Local smoothness has been used in the SMART algorithm, §6.1.3; Maximum Entropy and local smoothness are inherent in the Pixon method, §6.1.2. All methods use positivity, either implicitly or explicitly. We can also construct heuristic functions encapsulating the physics of line formation if we wish (Fox & Kankelborg, 2002). In the present implementation we have chosen not to add this layer of complexity.

I have performed trial inversions using a variety of methods, including:

- simulated annealing (using the Metropolis algorithm Press et al., 1992, p. 444),
- parametric inversion, where the spectrum at each  $(x, y)$  position is parameterized as two gaussians with given intensities, widths, and line centers (Fox & Kankelborg, 2002),
- Fourier backprojection (described herein),
- Pixon reconstruction (described herein),
- Singular Value Decomposition (SVD Press et al., 1992, p. 59),
- and Smooth Multiplicative Algebraic Reconstruction Technique (SMART, described herein).

The most mature of these methods, Fourier backprojection, Pixon reconstruction, and SMART, will be detailed in their own sections below. These methods advanced to the point of quantitative comparisons and achieved some success in inversion of simulated data. I will only touch upon the other methods briefly.

Parametric inversion and simulated annealing were never formulated to include the infinite order projection heuristic, although in principle this could be done. Their performance in trial inversions suffered due to the lack of this heuristic. Both are promising avenues for further exploration with the addition of the infinite order projection (especially parametric inversion). SVD produced results qualitatively like Fourier backprojection, but was not as successful quantitatively (and is also slower); it is principally useful as a toy for visualizing the nullspace.

### 6.1.1 Fourier Backprojection

The Fourier backprojection method treats the inversion as a traditional tomography problem. All measurements during the inversion are in pixel units and there

is no indication at any point that one axis is a  $\lambda$  axis rather than a  $y$  axis. The reconstruction makes use of the Fourier slice theorem (Kak & Slaney, 1988) and a positivity constraint.

Backprojection is the standard method of inverting a Radon transform. The values of the Radon transform at various angles are projected back along the integration line of their origin. The inverse is constructed from the intersections of the various backprojections. Frequently this process is implemented in Fourier space through the Fourier slice theorem.

The Fourier slice theorem states:

$$\mathcal{F}[R_f(\alpha, s)] = \tilde{f}(s \cos \alpha, s \sin \alpha) \quad (6.1)$$

In words, the 1-D Fourier transform (carried out over the parameter  $s$ ) of the Radon transform of a 2-D function  $f$  is equal to a slice at an angle  $\alpha$  of the 2-D Fourier transform of  $f$ ; the Fourier transforms of the data functions are slices of the Fourier transform of the cube (see figure 6.1). This theorem may be used to recover the function  $f$  from its Radon transform by populating the 2-D Fourier space with the Fourier transforms of the various angles  $\alpha$ , interpolating onto a square (from a radial) grid, if necessary, and applying the inverse transform. The first use of this theorem in an astronomical context (specifically radio astronomy) appears to be Bracewell (1956).

In the real world the Radon transform is sampled at discrete angles. Error in the reconstruction results from the undersampling of the Fourier transform at high frequency, where the projection slices are farther apart, and oversampling at low frequency where they are closer together. This is ameliorated with a ramp filter, weighting high frequency data more, relative to low frequency data. This is called filtered back projection.

Direct application of filtered back projection to *MOSES* data does not result in usable reconstructions. The typical number of slices required for good fidelity begins at about 60. Medical CT scans frequently employ over 300 slices. By comparison we have four, including the heuristic infinite order. We have added a positivity constraint, implemented iteratively, to our method. We proceed as follows: The data are transformed and placed in their slices in a blank Fourier transform (the  $\infty$  order is padded with zeros to make the transform square). This is inverse transformed back to real space. Because the Fourier transform was undersampled this results in many negative pixels in the resulting image. Negative pixels are zeroed in coordinate space and the non-negative image is transformed back into Fourier space. The new transform has non-zero elements in the wedges (see figure 6.1) that previously were not populated by data. It also has altered values for the data functions. These slices are reloaded with the correct (measured) values. We now transform back to real space and iterate this procedure until the resulting image in real space has negligible negative intensity (negligible is defined by the convergence criterion  $\sum(I < 0) \leq \sqrt{\sum I}$ ).

Figures 6.2 and 6.3 show the results of a trial inversion performed with the back-projection method. The algorithm assures that the fit to the data is essentially perfect ( $\chi^2 \sim 0$ ). The plot in figure 6.3 shows the 1st, 2nd, and 3rd quartiles of the He II line profile. The differences (mean and RMS) between the true and reconstructed data are summarized in table 6.2.

### 6.1.2 Pixon Inversion

Pixon reconstruction is a powerful Bayesian technique for restoring or reconstructing complexly encoded image data. The basic ideas behind the technique and its use are covered in a variety of references (Puettner, 1994, 1996; Piña & Puettner, 1993; Dixon et al., 1996; Alexander & Metcalf, 1997; Metcalf et al., 1996). The technique relies

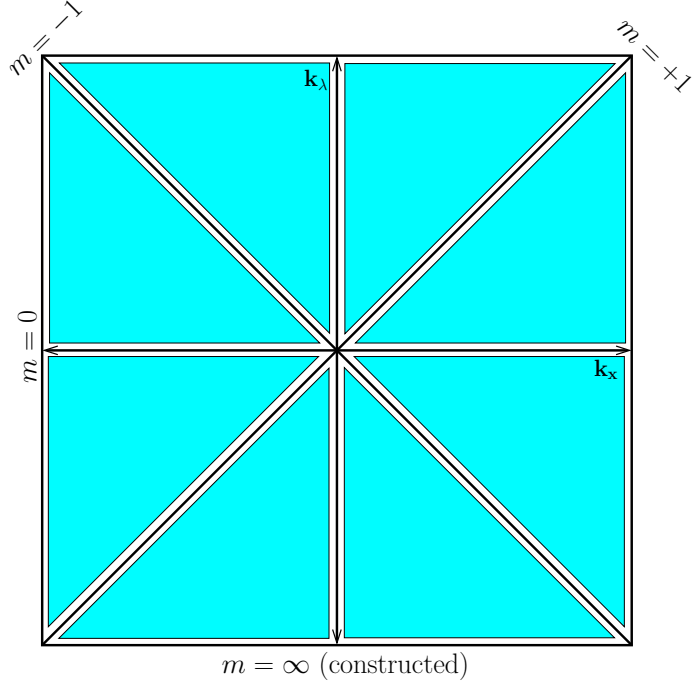


Figure 6.1: The Fourier space representation of a spectral cube. The dark lines are measured by *MOSES* or constructed from prior knowledge. The shaded wedges are constrained by the requirement of non-negativity in real space.

on ideas from information theory. The standard representation of images, collections of square pixels with uniform intensity across the area of the pixel, while convenient for working with physical detectors, is not ideal as a mathematical representation. The contents of images, or rather the physical objects the image data represent, are seldom structured in square, same-size, flat blocks. Pixons are a generalization of pixels, allowing an image to be represented by a set of elements (basis functions) which can be whatever shape and size is appropriate for the content of a specific image. The Pixons need not be flat, like pixels, but can distribute intensity over their area in any way desired. If the Pixon shape functions and intensity distributions are smoothly varying functions, local smoothness is automatic. Different Pixons can be used at different places in the image, according to whatever is best for representing the

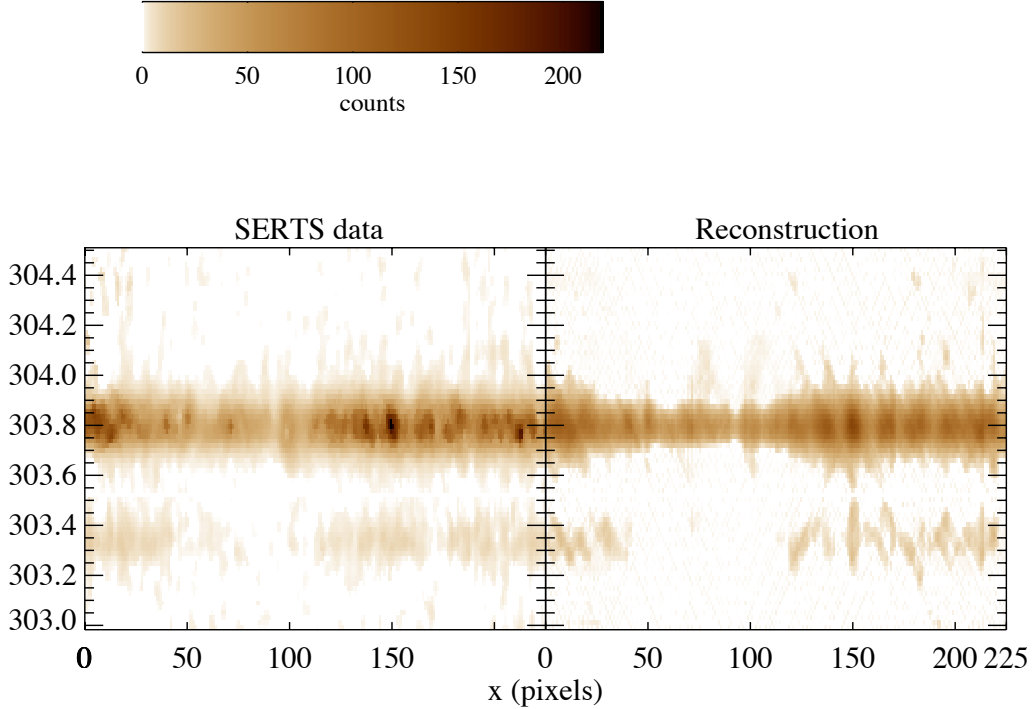


Figure 6.2: Original *SERTS-95* data vs. the Fourier backprojection reconstruction. The *SERTS-95* data have been rescaled to correspond to anticipated *MOSES* count rates.

image. With so much freedom to choose image parameters how shall we decide which is “best” for a particular image? Information theory guides us: the image model with minimal information content is “best”. In other words try to specify the image using the smallest possible number of parameters. This is a statement of Ockham’s Razor in the terms of information theory. In the Pixon approach one allows the image model to change during the reconstruction while attempting to maximize the goodness-of-fit (GOF) and minimize the information content of the image (quantified as the number of Pixons). In this regard the Pixon prior is very similar to Maximum Entropy.

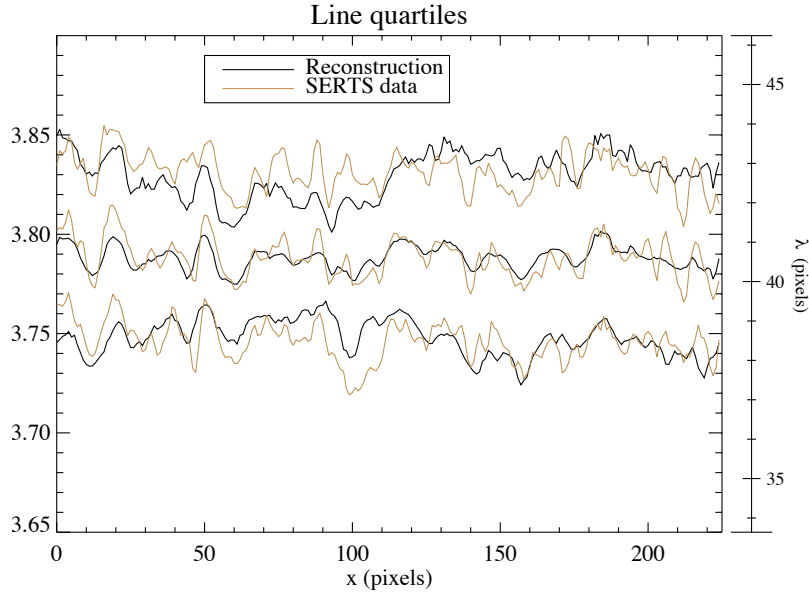


Figure 6.3: 1st, 2nd, and 3rd quartiles of the *SERTS-95* image and the Fourier backprojection reconstruction.

One common image model, which we use for *MOSES* reconstructions, is a pseudo-image/Pixon-map pair with “fuzzy” Pixons. In practice one specifies a set of Pixons with which to model the image. This set is not the optimal set of Pixons for a generic image; its selection is driven by the kind of image one expects to find. The reconstruction only approaches the ideal of minimal information content as a result of the limited selection of Pixons in the basis set. The image is a “convolution” of the pseudoimage with the Pixon map,  $\mathbf{I} = \mathbf{M} \otimes \mathbf{P}$ . The “ $\otimes$ ” operator is not a true convolution, but very similar. The Pixon map specifies the fuzzy Pixon basis function to use at a given pseudoimage position. The fuzzy Pixons are normalized shape functions (convolution kernels) which give the size scale and shape of the information content in the image at that place. The pseudoimage intensity at each point is multiplied by the appropriate shape function, which spreads this intensity out over some area. Both the pseudoimage and Pixon map are allowed to vary in order to accomplish the

twin goals of minimizing information and maximizing fidelity to the measured data functions. The pseudoimage is easily chosen to be strictly non-negative, as are the Pixon basis functions. The convolution process which generates the image from the pseudoimage and the Pixon map enforces both smoothness and positivity.

We have performed a reconstruction with this Pixon method. The initial Pixon map is chosen to consist entirely of the largest size Pixon. The pseudoimage is initialized with two lines at approximately the locations of the He II and Si XI line. The pseudoimage and Pixon map are optimized independently of each other to maximize the GOF criterion (we have chosen  $\chi^2$ , minimizing  $\chi^2$  is equivalent to maximizing GOF). When the  $\chi^2$  has been minimized over  $\mathbf{P}$  with  $\mathbf{M}$  held constant we allow the next smallest Pixon shape function to be put into the map and then minimize  $\chi^2$  over  $\mathbf{M}$  with  $\mathbf{P}$  held constant. At the end of this optimization we return to minimizing over  $\mathbf{P}$  with  $\mathbf{M}$  constant. At the end of each such iteration we reset the entire Pixon map to the largest size and allow one smaller size from the Pixon basis than was allowed in the last iteration. The procedure terminates on the  $\mathbf{P}$  optimization after the last Pixon in the basis has been added to the available Pixons.

Our Pixon basis for this reconstruction is shown in figure 6.4. The Pixons are elliptical truncated gaussians with major axis aligned with the  $\lambda$  direction. The shape function is defined by

$$S(x, \lambda) = \frac{R(x, \lambda)}{\int R(x, \lambda) dx d\lambda}$$

where

$$R(x, \lambda) = \exp \left( -\frac{(x - c_x)^2}{2r_s^2} - \frac{(\lambda - c_\lambda)^2}{2(r_s + 3)^2} \right)$$

The constants  $(c_x, c_\lambda)$  and  $r_s$  define the center and minor axis scale of each Pixon. The Pixons all have a common center. The largest Pixon in figure 6.4 is circular rather than elliptical. This Pixon is intended to cover large areas of nearly uniform intensity.

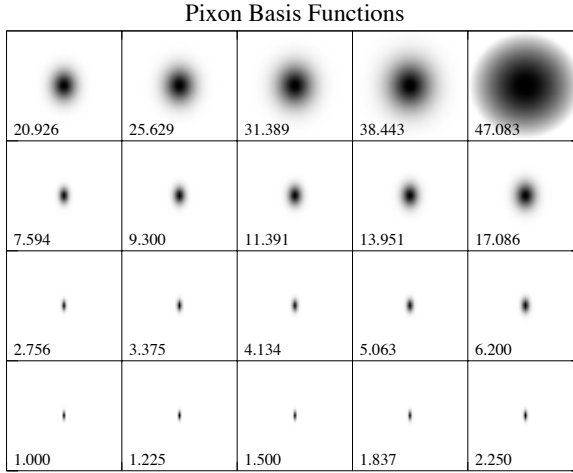


Figure 6.4: The Pixon basis for this reconstruction. The effective minor axis size is given in the lower left corner of each box. The major axis is 3 pixels larger than this value. The largest Pixon is circular rather than elliptical.

These will usually be nearly zero intensity regions for solar images in this passband and don't necessarily have any particular shape. The other Pixons are intended to cover the spectral lines, which are believed to be gaussian in the wavelength axis.

This Pixon basis is far from optimal. There are not enough Pixons in it and no Pixons which are longer in the  $x$  direction. Such Pixons might be thought appropriate for fitting sections of spectral lines where the width is nearly constant. Furthermore this basis is incomplete, in that it cannot produce a generic image because it contains no Pixon which is the size of one pixel. These problems with the basis are evident in the comparison of the data with the reconstruction which is presented in figure 6.5. The reduced  $\chi^2$  for each of the orders  $(+, -, 0, \infty)$  are  $(1.07, 1.05, 1.25, 4.54)$ . The quartiles plot for the central 225 pixels (equivalent to the plot for the Fourier

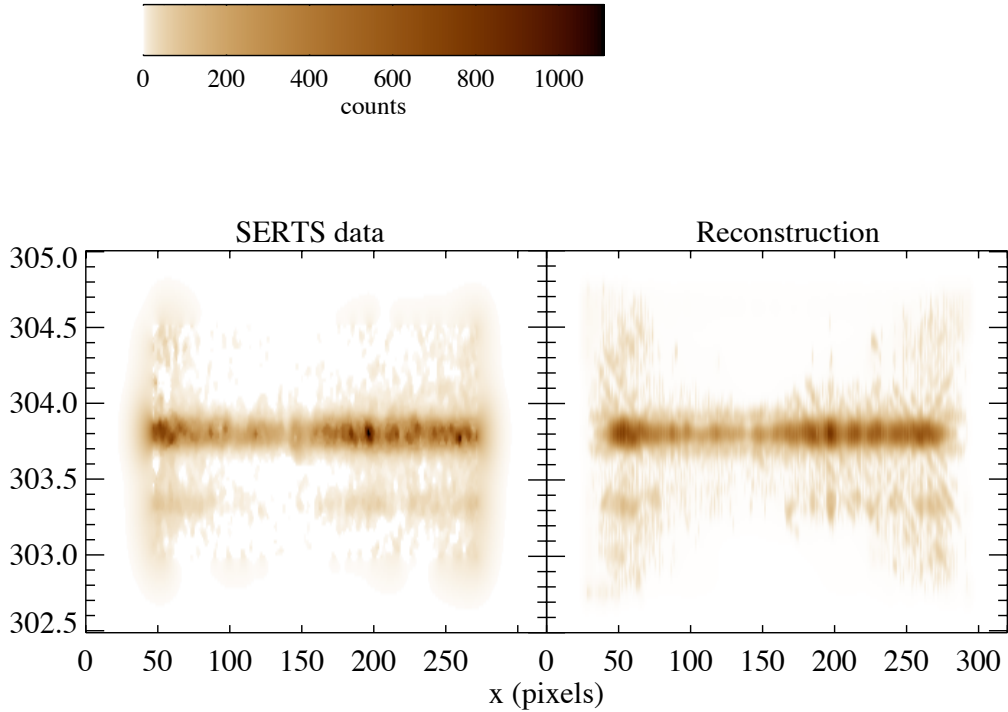


Figure 6.5: A comparison of *SERTS-95* data (rescaled) with the reconstruction via the Pixon method. The *SERTS-95* data has been extended so that it goes to zero smoothly in all directions at the edges.

backprojection method) is presented in figure 6.6. Table 6.2 summarizes the success of both Fourier backprojection and Pixons in reconstructing line profile parameters.

### 6.1.3 Smooth Multiplicative Algebraic Reconstruction Technique

The Smooth Multiplicative Algebraic Reconstruction Technique (SMART) was conceived and developed by Charles C. Kankelborg as a “quick and dirty” inversion method, with the goal of obtaining quick-look inversion products which might not be very robust. It turned out to be the best inversion method we investigated. It was first described in Kankelborg & Fox (2004). Kankelborg (2008a); Plumberg &

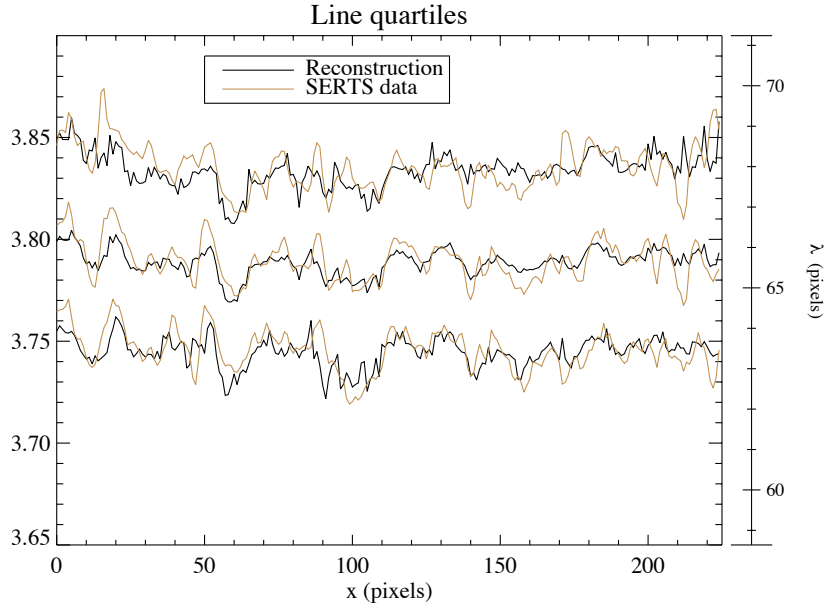


Figure 6.6: Quartiles plot for the Pixon reconstruction similar to figure 6.3.

Kankelborg (2010); Kankelborg (2008b) describe the method in more detail, with application to inverting data from the STEREO satellite mission. The method is similar to Multiplicative Algebraic Reconstruction Techniques (MART, see Okamoto & Yamaguchi, 1991; Verhoeven, 1993), but adds iterative smoothing. The first inversions of *MOSES* flight data were performed with SMART and were reported in Fox & Kankelborg (2009), and will be described in greater detail in section 6.3.

The core of the method begins with a cube in hyper-spectral space. Forward projecting the cube produces the 3+1 *MOSES* orders which *would* have been observed if this were the real solar source. Comparison is made between these projections and the measured (and inferred) inputs and correction factors are derived from the comparison. The cube is then multiplied by the correction factors and smoothed, and the process repeats. Concretely – denote the cube by  $G(x, \lambda)$ , the orders by  $I_m$ , and

the projection operator by  $T$  (see § 2.2 on page 12 for a definition of this operator), then:

1. Take as an initial guess,  $G(x, \lambda) = I_0(x)I_\infty(\lambda)/N$ .  $N$  is the total counts in the  $m = 0$  order image.
2. Project through this cube,  $[I'_0, I'_{+1}, I'_{-1}, I'_\infty] = \mathbf{T}[G]$ .
3. The projections will differ from the measured (inferred) data. Correct the cube using the ratios of the real and modeled images,

$$G = G \left[ \frac{I_0(x)}{I'_0(x)} \right]^\gamma \left[ \frac{I_{+1}(x + \lambda)}{I'_{+1}(x + \lambda)} \right]^\gamma \left[ \frac{I_{-1}(x - \lambda)}{I'_{-1}(x - \lambda)} \right]^\gamma \left[ \frac{I_\infty(\lambda)}{I'_\infty(\lambda)} \right]^\gamma.$$

The power  $\gamma$  is less than 1.0. It prevents numerical instabilities due to noise by not allowing the full correction factors to be applied in any one iteration.

4. Smooth the corrected cube,

$$G = G \otimes \frac{1}{1 + 2a + 2b} \begin{bmatrix} 0 & a & 0 \\ b & 1 & b \\ 0 & a & 0 \end{bmatrix}.$$

The smoothing parameters  $a$  and  $b$  apply smoothing to the  $\lambda$  and  $x$  axes, respectively.

5. Project through the new cube,  $[I'_0, I'_{+1}, I'_{-1}, I'_\infty] = T[G]$ .
  6. Evaluate the goodness-of-fit (GOF). We use the reduced  $\chi^2$  parameter, one for each of the measured orders,  $\chi_0^2, \chi_{+1}^2, \chi_{-1}^2$ .
  7. Adjust the smoothing parameters using the GOF,  $a = a/(\chi_{+1}^2 \chi_{-1}^2); b = b/\chi_0^2$ .
- This step drives the inversion to a reduced  $\chi^2$  of one. When the GOF is bigger than one it indicates underfitting, so we reduce the smoothing so higher-frequency information is retained; this causes the  $\chi^2$  to move toward one in the

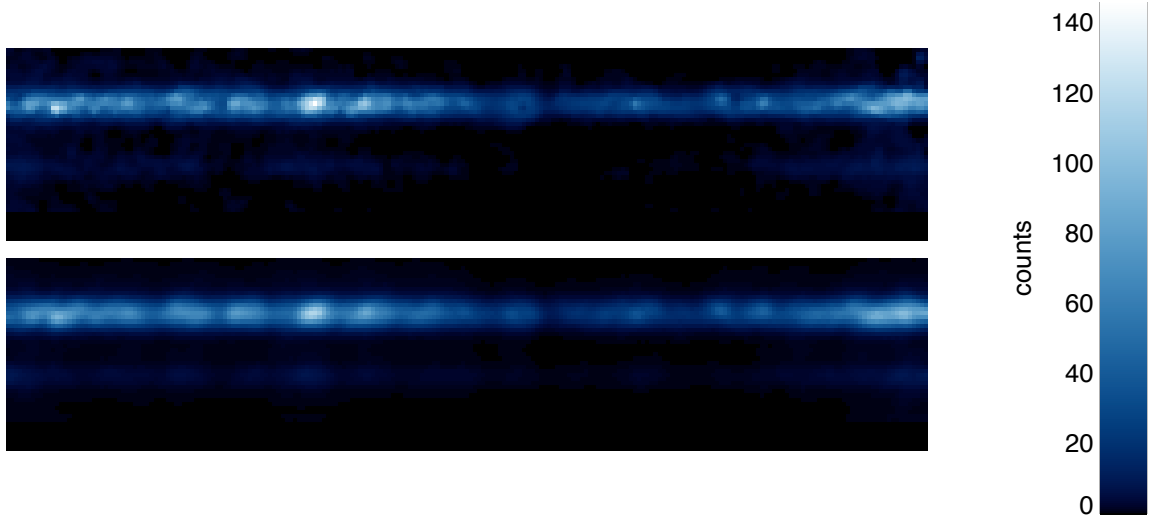


Figure 6.7: The SMART reconstruction of our simulated spectrum. The actual data is at top and the reconstruction at bottom.

next iteration. If the GOF is less than one it indicates that we are overfitting, and the smoothing parameters are increased, causing  $\chi^2$  to increase in the next iteration. The  $b$  parameter is most effective in the  $m = 0$  order, so that reduced  $\chi^2$  is used to tune it, whereas the  $a$  parameter most strongly affects the outboard orders, so the geometrical mean of those  $\chi^2$  are used.

8. Now loop to step 3. No convergence criterion is used to end the iterations. A fixed number are performed, and the final values of  $\chi^2$  are checked at the end. More iterations may be performed if necessary, by restarting the inversion method with the last output as the initial guess.

The results of applying this method to a simulated spectrum are shown in figure 6.7. Quantitative results in fitting the line center and line width via SMART are presented alongside similar results for the other two methods in table 6.2.

## 6.2 Discussion of Simulation Results

We have presented three methods for reconstructing an image cube from *MOSES* data. Our Pixon implementation is still very new and incomplete. Although work on the Fourier backprojection method has not ceased, it is far closer to maturity than the Pixon method. The SMART method provides, so far, the best reconstructions, and is the only method that has had any success in fitting the Si XI 303.3 Å data.

The methods have different computational and theoretical characteristics. The Fourier method is fast ( $\sim 1$  min to run on the *SERTS* test cube) and provides a “quick-look” data product with roughly the right character. The Pixon method is based on a technique that has proven powerful and robust in other applications (Dixon et al., 1996; Alexander & Metcalf, 1997; Metcalf et al., 1996). We believe Pixons may yield the best reconstructions possible. This method is slow ( $\sim 2.5$  hr to run on test data) and may require tuning for the *MOSES* application, especially in the choice of Pixon basis. The SMART algorithm is both fast ( $\sim 1$  min) and produces high fidelity reconstructions.

Cursory inspection of figures 6.2 and 6.5 leads to the conclusion that Fourier backprojection and Pixons produce comparable reconstructions. The quartile plots in particular give us confidence that both methods are generally able to reproduce the features of the strong He II line. The general similarity between these two methods should be taken as validation that the *MOSES* concept is sound. However, there are detectable differences between the two reconstructions. Inspection of figure 6.7 shows SMART to be the best of the three methods. The features of the He II line are more faithfully recovered. It is evident that all three methods tend to overly smooth the line features. This is a general feature of reconstructions of Radon transform data, by any method.

To be quantitative we take the quartiles as measures of the line parameters of physical interest, line center and width. These would allow us to produce, for instance, dopplergrams in He II and doppler broadening maps. The errors in line center and line width (based on quartiles) from each inversion method are summarized in Table 6.2. Both the Fourier backprojection and the Pixon methods centroid the line profile to  $\sim \frac{1}{3}$  pixel, which corresponds to approximately 10 mÅ or 10 km/s velocity discrimination. Fourier backprojection infers a linewidth that is systematically narrow. The Pixon method yields superior, sub-pixel line width determination with no overall bias. The SMART algorithm does better, achieving  $\sim 1/4$  pixel precision in line center, and  $\sim 1/3$  pixel precision in linewidth, but infers a systematically wide line width.

Table 6.1: Differences between true and reconstructed line profile parameters. Line center and linewidth errors are in pixels. For each parameter, a mean offset and RMS error are given. One *MOSES* pixel is approximately 29 mÅ.

Algorithm	center (median)		width (quartiles 1-3)	
	mean	RMS	mean	RMS
Fourier	-0.01	0.32	-0.19	0.97
Pixon	-0.04	0.36	-0.04	0.59
SMART	0.04	0.23	0.18	0.34

It is apparent from the reconstructed images (figures 6.2 and 6.5) neither Fourier backprojection nor Pixon reconstruction recovers the relatively weak Si XI line accurately. Perhaps a fully matured Pixon method will allow recovery of Si XI intensity. This would undoubtedly also lead to improved determination of the He II line profile, which is likely limited by noise from the unrecovered Si XI. By contrast the SMART algorithm does reconstruct the Si XI line.

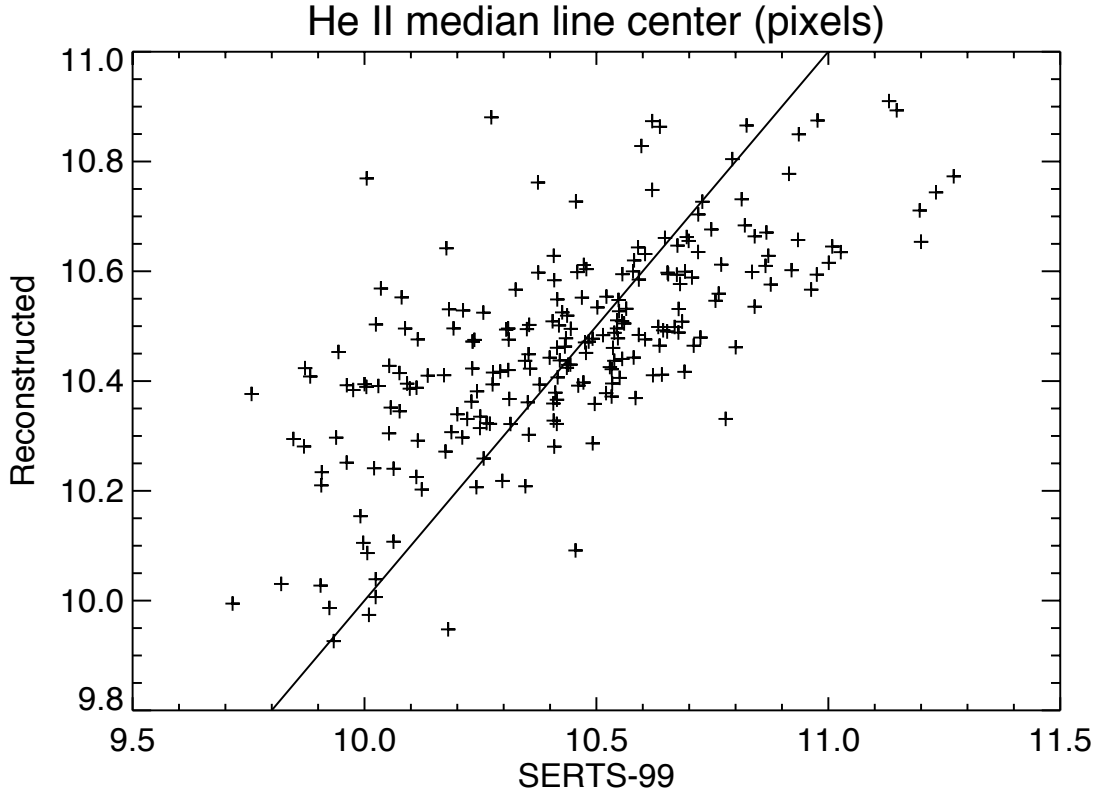


Figure 6.8: The systematic error in the SMART reconstruction of line center. The scatter plot shows the median line center of the real spectrum versus the reconstructed spectrum. The solid curve is the line  $y = x$ , showing where the scatter should lie if there were no systematic error.

Figure 6.8 shows the systematic bias of the SMART algorithm measurements of line center, an obvious underestimate. This systematic underestimate of line shift, although it does not show up in the mean line center measurement (see table 6.2), is a feature of all three reconstruction algorithms.

### 6.3 Inversion of *MOSES* Flight Data

I have performed inversions of flight data using the SMART algorithm. SMART was chosen because it is the most mature, best performing algorithm we tested, and

it is also computationally fast. Our trial inversions were performed on a cube  $273 \times 57\lambda$  pixels. The full *MOSES* flight data is  $(x, y, \lambda, t) = 2048 \times 1024 \times 64 \times 27$  pixels, so algorithm time complexity is of some concern. To increase the speed of reconstructions I selected one *MOSES* flight frame for analysis, frame 23, studied extensively in chapter 5. I further reduced the size of the cube by selecting only a narrow strip of data  $1761 \times 128$  pixels for each of the three orders. The width is enough to include data from off the limb to somewhat west of the explosive event. The 128 pixel height extends just north of the EE. It was carefully chosen so that no saturated pixels would be included in the field of view in any of the three orders. This strip of data is shown in figure 6.9.

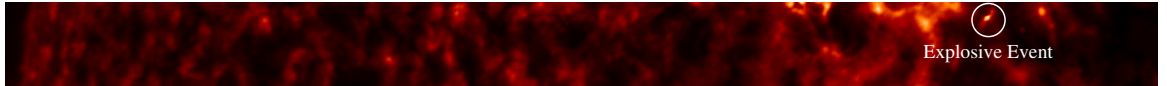


Figure 6.9: The section of flight data used in inversion. This strip is from frame 23.

The SMART algorithm used for the flight reconstruction was modified somewhat from that given above in section 6.1.3. Step 3 was altered so that the correction power,  $\gamma$ , depends on spectral order, thus:

$$G = G \left[ \frac{I_0(x)}{I'_0(x)} \right]^{\gamma_0} \left[ \frac{I_{+1}(x + \lambda)}{I'_{+1}(x + \lambda)} \right]^{\gamma_{+1}} \left[ \frac{I_{-1}(x - \lambda)}{I'_{-1}(x - \lambda)} \right]^{\gamma_{-1}} \left[ \frac{I_\infty(\lambda)}{I'_\infty(\lambda)} \right]^{\gamma_\infty}.$$

Step 4 was modified to use a constant 3-D symmetric smoothing kernel,  $\kappa_\zeta$ , the 3-D  $\zeta$  kernel, a cubic kernel with 27 elements ( $3 \times 3 \times 3$ ). The “body-centered” element is  $\zeta^3$ , the six “face” elements (directly adjacent) are  $\zeta^2$ , the 12 “edge” elements are  $\zeta$ , the 8 “corners” are zero. The kernel is normalized by dividing by  $\zeta^3 + 6\zeta^2 + 12\zeta$ . The parameter  $\zeta$  is chosen before reconstruction. We also introduce a smoothing parameter,  $S \in [0, 1]$ , allowing us to adjust the amount of smoothing used for an inversion run. The final smoothing kernel is  $\kappa = (1 - S)\delta_{111} + S\kappa_\zeta$ .  $S = 1$  is maximal smoothing, while  $S = 0$  is no smoothing at all. We also no longer use variable

smoothing parameters to drive the convergence of  $\chi^2$ . Instead this is accomplished by altering the correction factor  $\gamma$ 's with each iteration. Thus step 7 now uses the following control law:

$$\gamma'_i = \gamma_i + g_X X_i + g_V V_i$$

where  $X_i = \ln \chi_i^2$  and  $V_i = dX_i/dt$ . The factors  $g_X$  and  $g_V$  are gain constants chosen before reconstruction. The order index,  $i$ , only runs over measured data orders,  $+1, 0, -1$ . The  $\gamma$  powers are not allowed to go above a maximum value, or below zero. The  $\gamma_\infty$  is set to  $\min(\gamma_i)/e$ , where  $e$  is a suppression factor,  $e \gg 1$ . The  $m = \infty$  order correction factors are not pushed as hard, since that order is inferred rather than measured.

We must compute an inferred spatially averaged spectrum for our  $m = \infty$  order. The average parameters of the two spectral lines in our passband are well known from previous experiments with slit spectrometers. I use the measurements of Brosius et al. (1998) from the *SERTS-95* rocket mission. The line parameters are given in table 6.2. Our instrumental line width is unknown, as our point spread functions have never been measured. The value given in table 6.2 is a conservative estimate, based on the results of parallax analysis in chapter 5.

Table 6.2: Line parameters used in the inferred  $m = \infty$  order. The line width parameters are FWHM.

	line center ( $\text{\AA}$ )	line width ( $\text{m\AA}$ )	Integrated Intensity ( $\text{erg/cm}^2 \cdot \text{s} \cdot \text{sr}$ )
He II	303.782	97.8	36000
Si XI	303.317	72.1	3360
Instrument	303.782	115.0	

The integrated intensities measured by Brosius et al. (1998) are not used directly, but give the ratio of He intensity to Si intensity. It should be noted that my estimate

of the intensity ratio is derived from Brosius et al. (1998, see their table 2) active region data, even though our flight data is essentially all quiet-sun. I used their quiet-sun data for the He II line width, but no measurement of Si XI was available in the quiet-sun (see their table 1). Since the implied intensity ratio derived from AR data would give a Si XI intensity that should have been observable by them in quiet-sun, this is strong evidence that the true quiet-sun He to Si intensity ratio is much less than what I have used.

An estimate of the continuum intensity in our passband is also necessary. Significant uncertainty exists in this estimation. It is possible there is no continuum emission. Many different models of the continuum were tried. The inversion shown below used a parabolic model of continuum intensity, with the parabola peaking at the He II line center and falling to zero at the edges of the cube. The percentage of total flux in the continuum is an adjustable parameter. I used 5% for this reconstruction. This estimate, as are others, is conservative. It is highly probable that the He II contribution dominates the cube, in all respects, more than I have assumed.

The width of the cube in the  $\lambda$  axis was chosen to be 64 pixels. This gives a passband,  $B = [302.854 \text{ \AA} - 304.710 \text{ \AA}]$ . In making this choice I have implicitly assumed nothing outside this band contributes to our data. This assumption is valid due to the dominance of our two lines in this part of the solar spectrum, especially the He II line. The nearby contaminant lines at 284  $\text{\AA}$  and 335  $\text{\AA}$  have been highly suppressed by our multilayer coatings, and the continuum emission, if it exists, is small. The choice of 64  $\lambda$  pixels is wide enough to contain any conceivable line shift of the He II line – a 1  $\text{\AA}$  shift at this wavelength would imply a doppler velocity of 1000  $\text{km s}^{-1}$ , an unlikely speed in the transition region. At the same time the width of the  $\lambda$  axis is short enough that the reflectivity of our optics is nearly constant (see Owens et al., 2005).

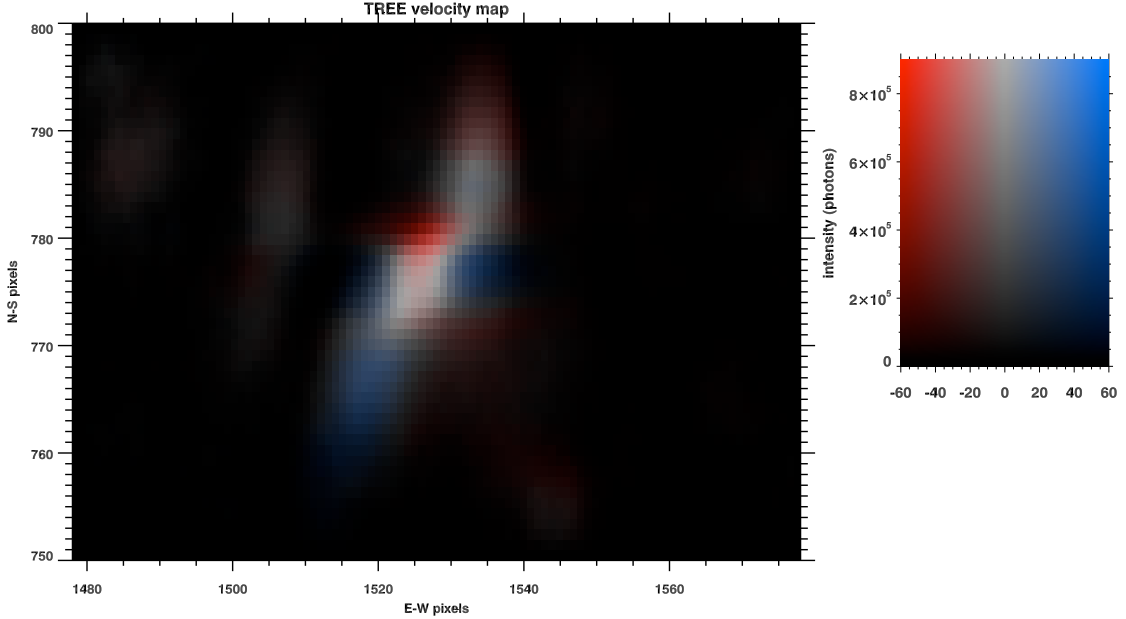


Figure 6.10: Dopplergram of the explosive event from inversion of *MOSES* data using SMART. The color indicates the line shift in  $\text{km s}^{-1}$ , the color saturation shows the photon intensity. The intensity in the legend is EUV photons at the aperture.

The other reconstruction parameters for the run that generated the results in figure 6.10 are:  $S = 0.01$ ,  $\zeta = 2.5$ ,  $g_X = 0.05$ ,  $g_V = 0.15$ ,  $\max \gamma = 0.5$ , initial  $\gamma = 0.5$ ,  $m = \infty$  order suppression factor  $e = 30$ , number of iterations, 300. The final reduced  $\chi^2$  values at the end of the inversion were:

$$\chi^2_{+1} = 1.00118, \quad \chi^2_0 = 0.997448, \quad \chi^2_{-1} = 2.05374$$

The IDL code used to implement SMART for flight data is given in the supplemental material (see B.11).

#### 6.4 Flight Inversion Results and Discussion

Figure 6.10 reveals that the inversion results, while qualitatively similar to what I found in chapter 5, underestimate the magnitude of the doppler shifts. This quantitative underestimate is unaffected by the choice of reconstruction parameters. Many

values of smoothness, continuum emission, and even line widths give largely the same result. The underestimate is due to systematic error in reconstructing line center shifts by SMART. In fact all tomographic inversion methods suffer from this problem to some degree. The reconstructed doppler shifts are always smaller and smoother than in the original test data.

Figure 6.8 on page 126 demonstrates the magnitude of the systematic underestimate that we expect from the SMART method. It is about 40%. This error may be somewhat different in the case of the modified SMART algorithm used on flight data, but will still be present. The  $75 \text{ km s}^{-1}$  SE jet blue-shift found in §5.6, if the SMART systematic error is taken to be 40%, would appear as  $45 \text{ km s}^{-1}$  in the inversion results. We actually find  $45 \text{ km s}^{-1}$  for this jet blue-shift in the data given in figure 6.10. For the NW jet the parallax analysis result is a red-shift of  $25 \text{ km s}^{-1}$ , with an expected estimate by SMART of  $15 \text{ km s}^{-1}$ , whereas we find  $20 \text{ km s}^{-1}$  for this jet doppler velocity in our results. This is somewhat less underestimated than we expect, but not unusually so given the  $8 \text{ km s}^{-1}$  ( $1/4$  pixel) random error for SMART (see table 6.2). For smaller velocities the random error and the systematic error become confounded. Doppler velocities in the core are small,  $\sim 5 \text{ km s}^{-1}$ ; too small to reliably measure by this method. The core, while a region of high non-thermal broadening (interpreted as large unresolved red and blue doppler shifts), has doppler shifts mostly balanced between red and blue, resulting in a net line shift of nearly zero. The exception is the large red-shift at the north edge of the core (see fig. 5.15 on page 104), where parallax analysis finds a very large red-shift component dominating a smaller blue-shift, for a net red-shift of  $60 \text{ km s}^{-1}$ . SMART finds  $50 \text{ km s}^{-1}$  at this point (versus our expectation of  $36 \text{ km s}^{-1}$  with the 40% underestimate).

While the systematic error in line center is somewhat limiting, for high velocity events, such as EE's, the reconstruction is very useful, bearing in mind that whatever

velocities are found will appear smaller than they are in reality. The systematic error is conservative in the sense that we can have confidence, if high velocities are found, that they are not an artifact. Further work on reconstruction techniques may also be able to improve the systematic error, for the SMART algorithm as well as others that are currently less mature. There is room for improvement in the Pixon technique, as well as others not discussed in this chapter, such as parametric inversion. Additional systematic errors may exist due to optical aberrations (see appendix C). The effect of aberrations on inversions is unclear and requires further study of synthetic data to determine the likely magnitude of the systematic error.

## 6.5 Acknowledgements

I gratefully acknowledge the helpful comments and suggestions of Dr Curt Vogel during his course on Inverse Problems in Image Processing and Adaptive Optics at MSU, Fall 2002.

## CHAPTER 7

### CONCLUSIONS

We have successfully built, tested, and flown a new sounding rocket instrument, a proof-of-concept mission of a novel slitless spectrograph design which performs tomography of a hyper-spectral cube (chapter 2 and 3). Our instrument returned 27 flight exposures during its 5 minute flight, images of the Sun in a narrow passband centered at 304 Å (chapter 3). Due to the dispersion in our three distinct spectral orders, these images contain information on the line profiles of both the He II 303.8 Å and Si XI 303.3 Å lines (chapter 2). We have also developed an algorithm for producing instrument flat-fields from a highly structured input beam (chapter 4). We obtained flat-fields from this technique which are accurate to 0.04%, although for flight-data the flat-fields are limited by the flight thin-film filters to 1% (§4.8).

We have invented a new technique for interpreting slitless spectroscopy data, Parallax Analysis, and with it discovered the first example of a He II 304 Å explosive event (chapter 5). Its physical structure is not what is predicted by standard  $X$ –point reconnection models. The plasma outflow jets are not collinear, or anti-parallel, both predictions of previous models. This discovery beautifully illustrates the power of simultaneous fast imaging spectroscopy. In the case of our event, an imager would have uncovered nothing of note, because without spectral data to show it was an explosive event it would have been passed over as being nothing out of the ordinary. With a conventional spectrograph, whether slit-scanning or otherwise, it is unlikely the event would have been seen at all. If fortuitously pointed at the event, it would have seen that it was an explosive event, but not observed its spatial structure, but it is the spatial structure of the event that contradicts standard explosive event models. Conventional spectrographs do not have the ability to image both the spatial and

spectral features of this event because of its highly transient nature. With only spectral data it would have been passed over as being nothing out of the ordinary.

The explosive event has three distinct regions, a core, a NW jet, and a SE jet. The jet velocities in three dimensions, are  $v_{NW} = (12 \pm 10.2, 80 \pm 13.8, -25 \pm 5) \text{ km s}^{-1}$  and  $v_{SE} = (17 \pm 10.3, -70 \pm 10.6, 75 \pm 5) \text{ km s}^{-1}$  where the first two coordinates are in the plane of the sky, and the third is along the line-of-sight. The angle between the jets is  $146^\circ \pm 7^\circ$  and it is 99% likely that the data are not consistent with anti-parallel jets. The core of the explosive event is a region of large non-thermal doppler broadening, with a peak width of  $380 \text{ km s}^{-1}$  FWHM. We interpret the non-thermal broadening as two unresolved doppler velocities, one toward the observer, and one away (§5.6). Mysteries remain; we do not know what causes the explosive event's unusual structure. We do not know how it is connected to the nearby filament channel, if at all. We have no model of a reconnection process which would generate it (§5.7).

We have shown that we can reproduce, through tomographic inversion, the line shifts of simulated spectral cubes to better than 1/3 pixel, or  $\sim 10 \text{ km s}^{-1}$ , using three reconstruction algorithms, Fourier backprojection, Pixon reconstruction, and SMART (§6.2). SMART performs best, with 1/4 pixel precision in line center, and 1/3 pixel precision in line width. It is also the only method that can reproduce the Si XI line to any degree. Other promising avenues for reconstruction remain to be explored. Our first attempt to invert *MOSES* flight data (§6.3) has met with some success, and can reproduce qualitatively and quantitatively the explosive event line shifts we observed using parallax analysis, albeit with systematic underestimation of doppler shifts by the SMART algorithm, a common phenomenon in tomographic reconstructions. The systematic error can be diagnosed using simulated data and has a fractional magnitude of  $\sim 40\%$ . The direction of the error is conservative; velocities are always underestimated, so measurements of large velocities are confi-

dently described as lower bounds on real solar phenomena. Future work on inversion algorithms may alleviate this large systematic error somewhat, but it is likely that it cannot be removed entirely; it is a limitation of tomography (§6.4).

### 7.1 Potential Applications

We have validated the concept of multi-order slitless spectroscopy in the EUV solar spectrum. We have thus invented the first EUV snapshot imaging spectrograph, and the first truly *fast* imaging spectrograph with wide field of view and high spatial resolution in this spectral regime. While we have applied it only to one narrow frequency band this is not a niche instrument. The concept is broadly applicable to any spectral band from infra-red to X-ray and to emission or absorption lines, using any optical design suited to the experiment at hand, with as many orders as are necessary and prudent, and flying either as a sounding rocket or an instrument on an orbital mission. Adding more orders, although it complicates the optical design, improves reconstruction fidelity, and would also allow the determination of line parameters for more than one spectral line simultaneously.

Multi-order slitless spectroscopy is already being used at visible wavelengths, in absorption lines, from the ground to perform high-speed magnetography (DeForest & Kankelborg, 2007; DeForest et al., 2009). Spectral measurements of magnetically sensitive lines are only one potential application. Observation of density sensitive line pairs, coupled with emission measure available from 0 order data can provide measurements of both density and filling factor over large fields and potentially many regions of the solar atmosphere. With spectral data over a wide field of view, temperature maps can be made more accurately than using ratios of narrowband images which are not simultaneous. There is a solar “zoo” of phenomena – bright points,

coronal loops, explosive events, spicules and macro-spicules, transient brightenings, flares, prominences, EUV blinkers, sigmoids, solar wind source points, jets, propagating wavefronts, shocks, etc. – all of which have EUV signatures. These transient phenomena evolve quickly and can only be fully understood when we have simultaneous imaging and spectra at high spatial and temporal resolution. Such data are needed to constrain theories of the heating of coronal loops, the source points of the solar wind, or the events leading up to the activation or eruption of prominences and filaments. Finally there are all the surprises that are bound to occur when we begin to look at the Sun in a new way, the “unknown unknowns”. Multi-order slitless snapshot imaging spectroscopy can be expected to discover the *unexpected*.

REFERENCES CITED

### Bibliography

- Alexander, D. & Metcalf, T. R. 1997, ApJ, 489, 442
- Andretta, V., Jordan, S. D., Brosius, J. W., Davila, J. M., Thomas, R. J., Behring, W. E., Thompson, W. T., & Garcia, A. 2000, ApJ, 535, 438
- Arnaud, M. & Rothenflug, R. 1985, A&AS, 60, 425
- Bendlin, C., Volkmer, R., & Kneer, F. 1992, A&A, 257, 817
- Bracewell, R. N. 1956, Australian Journal of Physics, 9, 198
- Brosius, J. W., Davila, J. M., & Thomas, R. J. 1998, ApJS, 119, 255
- Brosius, J. W., Thomas, R. J., & Davila, J. M. 1999, ApJ, 526, 494
- Brueckner, G. E. & Bartoe, J. 1983, ApJ, 272, 329
- Brueckner, G. E., Bartoe, J., Cook, J. W., Dere, K. P., Socker, D., Kurokawa, H., & McCabe, M. 1988, ApJ, 335, 986
- Bruner, M. E., Brown, W. A., & Appert, K. L. 1989, in Society of Photo-Optical Instrumentation Engineers (SPIE) Conference Series, ed. R. B. Hoover, Vol. 1160, 620–628
- Comte, A. 1858, The Positive Philosophy of August Comte, ed. H. Martineau (New York: Calvin Blanchard)
- Cook, J. W. & Brueckner, G. E. 1991, Fine structure of the solar transition region - Observations and interpretation, ed. Cox, A. N., Livingston, W. C., & Matthews, M. S., 996–1028
- Culhane, J. L., Harra, L. K., James, A. M., Al-Janabi, K., Bradley, L. J., Chaudry, R. A., Rees, K., Tandy, J. A., Thomas, P., Whillock, M. C. R., Winter, B., Doschek, G. A., Korendyke, C. M., Brown, C. M., Myers, S., Mariska, J., Seely, J., Lang, J., Kent, B. J., Shaughnessy, B. M., Young, P. R., Simnett, G. M., Castelli, C. M., Mahmoud, S., Mapson-Menard, H., Probyn, B. J., Thomas, R. J., Davila, J., Dere, K., Windt, D., Shea, J., Hagood, R., Moye, R., Hara, H., Watanabe, T., Matsuzaki, K., Kosugi, T., Hansteen, V., & Wikstol, Ø. 2007, Sol. Phys., 243, 19
- DeForest, C., Elmore, D. F., Bradford, M. P., Elrod, J., & Gilliam, D. L. 2004, ApJ, 616, 600
- DeForest, C., Rimmele, T., Berger, T., & Peterson, J. 2009, in AAS/Solar Physics Division Meeting, Vol. 40, AAS/Solar Physics Division Meeting 40, 33.01

- DeForest, C. E. 2003, in Proc. of the 3rd Solar Workshop on Spectropolarimetry, Trujillo-Bueno, J.; Sanchez-Almeida, J.; Eds., ASP Conf. Ser. 307 (in press)
- DeForest, C. E. & Kankelborg, C. C. 2007, ArXiv e-prints
- Dere, K. P. 1994, Advances in Space Research, 14, 13
- Dere, K. P., Bartoe, J., & Brueckner, G. E. 1989, Sol. Phys., 123, 41
- Dere, K. P., Bartoe, J., Brueckner, G. E., Ewing, J., & Lund, P. 1991, J. Geophys. Res., 96, 9399
- Dere, K. P., Doschek, G. A., Mariska, J. T., Hansteen, V. H., Harra, L. K., Matsuzaki, K., & Thomas, R. J. 2007, PASJ, 59, 721
- Descour, M. R., Volin, C. E., Dereniak, E. L., Gleeson, T. M., Hopkins, M. F., Wilson, D. W., & Maker, P. D. 1997, Appl. Opt., 36, 3694
- Dixon, D. D., Johnson, W. N., Kurfess, J. D., Pina, R. K., Puetter, R. C., Purcell, W. R., Tuemer, T. O., Wheaton, W. A., & Zych, A. D. 1996, A&AS, 120, C683
- Fox, J. L. & Kankelborg, C. C. 2002, in Bulletin of the American Astronomical Society, Vol. 34, Bulletin of the American Astronomical Society, 733
- Fox, J. L. & Kankelborg, C. C. 2008, in Eos Transactions of the AGU, Vol. 89, AGU Joint Assembly Supplement, Abs. SP51B-05
- Fox, J. L., Kankelborg, C. C., & Metcalf, T. R. 2003, in Society of Photo-Optical Instrumentation Engineers (SPIE) Conference Series, ed. A. M. Larar, J. A. Shaw, & Z. Sun, Vol. 5157, 124–132
- Fox, J. L., Kankelborg, C. C., & Thomas, R. J. 2010, ApJ, 719, 1132
- Fox, L. & Kankelborg, C. C. 2009, in AAS/Solar Physics Division Meeting, Vol. 40, AAS/Solar Physics Division Meeting 40, 33.04
- Freeland, S. L. & Handy, B. N. 1998, Sol. Phys., 182, 497
- Gore, D. B. 1999, PhD thesis, UNIVERSITY OF ALABAMA AT BIRMINGHAM
- Handy, B. N., Acton, L. W., Kankelborg, C. C., Wolfson, C. J., Akin, D. J., Bruner, M. E., Caravalho, R., Catura, R. C., Chevalier, R., Duncan, D. W., Edwards, C. G., Feinstein, C. N., Freeland, S. L., Friedlaender, F. M., Hoffmann, C. H., Hurlburt, N. E., Jurcevich, B. K., Katz, N. L., Kelly, G. A., Lemen, J. R., Levay, M., Lindgren, R. W., Mathur, D. P., Meyer, S. B., Morrison, S. J., Morrison, M. D., Nightingale, R. W., Pope, T. P., Rehse, R. A., Schrijver, C. J., Shine, R. A., Shing, L., Strong, K. T., Tarbell, T. D., Title, A. M., Torgerson, D. D.,

- Golub, L., Bookbinder, J. A., Caldwell, D., Cheimets, P. N., Davis, W. N., Deluca, E. E., McMullen, R. A., Warren, H. P., Amato, D., Fisher, R., Maldonado, H., & Parkinson, C. 1999, Sol. Phys., 187, 229
- Huggins, W. & Huggins, M. L. 1899, An Atlas of Representative Stellar Spectra from  $\lambda$ 4780 to  $\lambda$ 3300, together with a discussion of the evolution order of the stars, and the interpretation of their spectra; preceded by a short history of the observatory, Vol. 1 (London: Publications of Sir William Huggins' Observatory)
- Innes, D. E., Inhester, B., Axford, W. I., & Wilhelm, K. 1997, Nature, 386, 811
- Johnson, W. R., Wilson, D. W., & Bearman, G. 2005, Optics Letters, 30, 1464
- Kak, A. C. & Slaney, M. 1988, Principles of Computerized Tomographic Imaging (New York: IEEE Press)
- Kankelborg, C. C. 2008a, AGU Spring Meeting Abstracts, D2
- . 2008b, ArXiv e-prints
- Kankelborg, C. C. & Fox, J. L. 2004, in Bulletin of the American Astronomical Society, Vol. 36, American Astronomical Society Meeting Abstracts, #204, 794
- Kankelborg, C. C. & Thomas, R. J. 2001, in Proc. SPIE Vol. 4498, p. 16-26, UV/EUV and Visible Space Instrumentation for Astronomy and Solar Physics, Oswald H. Siegmund; Silvano Fineschi; Mark A. Gummin; Eds., 16–26
- Kankelborg, C. C., Walker, II, A. B. C., & Hoover, R. B. 1997, ApJ, 491, 952
- Kankelborg, C. C., Walker, II, A. B. C., Hoover, R. B., & Barbee, Jr., T. W. 1996, ApJ, 466, 529
- Kent, B. J., Harrison, R. A., Sawyer, E. C., Hayes, R. W., Richards, A. G., Culhane, J. L., Norman, K., Breeveld, A. A., Thomas, P. D., Poland, A. I., Thomas, R. J., Thompson, W. T., Aschenbach, B. R., Braeuninger, H. W., Kjeldseth-Moe, O., Kuehne, M., Hollandt, J., Paustian, W., & Bromage, B. J. 1995, in Proc. SPIE Vol. 2517, p. 12-28, X-Ray and EUV/FUV Spectroscopy and Polarimetry, Silvano Fineschi; Ed., Vol. 2517, 12–28
- Kosugi, T., Matsuzaki, K., Sakao, T., Shimizu, T., Sone, Y., Tachikawa, S., Hashimoto, T., Minesugi, K., Ohnishi, A., Yamada, T., Tsuneta, S., Hara, H., Ichimoto, K., Suematsu, Y., Shimojo, M., Watanabe, T., Shimada, S., Davis, J. M., Hill, L. D., Owens, J. K., Title, A. M., Culhane, J. L., Harra, L. K., Doschek, G. A., & Golub, L. 2007, Sol. Phys., 243, 3
- Kuhn, J. R., Lin, H., & Loranz, D. 1991, PASP, 103, 1097

- Longcope, D. W. 1998, ApJ, 507, 433
- Metcalf, T. R., Hudson, H. S., Kosugi, T., Puetter, R. C., & Piña, R. K. 1996, ApJ, 466, 585
- Moses, D., Cook, J. W., Bartoe, J., Brueckner, G. E., Dere, K. P., Webb, D. F., Davis, J. M., Harvey, J. W., Recely, F., Martin, S. F., & Zirin, H. 1994, ApJ, 430, 913
- Okamoto, T. & Yamaguchi, I. 1991, Optics Letters, 16, 1277
- Owens, S. M., Gum, J. S., Tarrio, C., Grantham, S., Dvorak, J., Kjornrattanawanich, B., Keski-Kuha, R., Thomas, R. J., & Kankelborg, C. C. 2005, in Society of Photo-Optical Instrumentation Engineers (SPIE) Conference Series, ed. O. Citterio & S. L. O'Dell, Vol. 5900, 5–13
- Patel, A. M. & Hong, S. J. 1974, IBM Journal of Research and Development, 18, 579
- Piña, R. K. & Puetter, R. C. 1993, PASP, 105, 630
- Plumberg, C. & Kankelborg, C. C. 2010, in American Astronomical Society Meeting Abstracts, Vol. 216, American Astronomical Society Meeting Abstracts 216, 407.22
- Potts, H. E. & Diver, D. A. 2008, A&A, 492, 863
- Press, W. H., Teukolsky, S. A., Vetterling, W. T., & Flannery, B. P. 1992, Numerical recipes in C. The art of scientific computing, ed. Press, W. H., Teukolsky, S. A., Vetterling, W. T., & Flannery, B. P. (Cambridge: University Press, —c1992, 2nd ed.)
- Puetter, R. C. 1994, in Proc. SPIE Vol. 2302, p. 112-131, Image Reconstruction and Restoration, Timothy J. Schulz; Donald L. Snyder; Eds., 112–131
- Puetter, R. C. 1996, in Proc. SPIE Vol. 2827, p. 12-31, Digital Image Recovery and Synthesis III, Paul S. Idell; Timothy J. Schulz; Eds., 12–31
- Scherrer, P. H., Bogart, R. S., Bush, R. I., Hoeksema, J. T., Kosovichev, A. G., Schou, J., Rosenberg, W., Springer, L., Tarbell, T. D., Title, A., Wolfson, C. J., Zayer, I., & MDI Engineering Team. 1995, Sol. Phys., 162, 129
- Schumacher, R. J. & Hunter, W. R. 1977, Appl. Opt., 16, 904
- Settele, A., Carroll, T. A., Nickelt, I., & Norton, A. A. 2002, A&A, 386, 1123
- Thomas, R. J. & Kankelborg, C. C. 2001, in Bulletin of the American Astronomical Society, Vol. 33, Bulletin of the American Astronomical Society, 1434
- Thomas, R. J. & Neupert, W. M. 1994, ApJS, 91, 461

- Tyson, J. A. 1986, Journal of the Optical Society of America A, 3, 2131
- Verhoeven, D. 1993, Applied Optics, 32, 3736
- Vernazza, J. E. & Reeves, E. M. 1978, ApJS, 37, 485
- Wachter, R., Schou, J., Rabello-Soares, M. C., Miles, J. W., Duvall, T. L., & Bush, R. I. 2011, Sol. Phys., 19
- Wilson, D. W., Maker, P. D., & Muller, R. E. 1997, in Proc. SPIE Vol. 3118, p. 184-193, Imaging Spectrometry III, Michael R. Descour; Sylvia S. Shen; Eds., 184-193
- Zelik, M., Gregory, S. A., & Smith, E. V. P. 1992, Introductory astronomy and astrophysics, ed. Zelik, M., Gregory, S. A., & Smith, E. V. P. (Fort Worth : Saunders College Pub., c1992. 3rd ed.)
- Zirker, J. B. 2002, Journey from the center of the sun, ed. Zirker, J. B. (Princeton and Oxford: Princeton University Press)

## APPENDICES

APPENDIX A

LIST OF ACRONYMS

**ACS** Attitude Control System

**ADC** Analog-to-Digital Converter

**AIA** Atmospheric Imaging Assembly

**AR** Active Region

**CCD** Charge Coupled Device

**CDS** Coronal Diagnostic Spectrometer

**COTS** Commercial Off-The-Shelf

**CPU** Central Processing Unit

**CTIS** Computed Tomography Imaging Spectroscopy

**CXRO** Center for X-Ray Optics

**DC** Direct Current

**DIO** Digital Input/Output

**DN** Data Number

**DR** Design Review

**EBX** Embedded Board eXpandable

**EE** Explosive Event

**EGSE** Electronic Ground Support Equipment

**EIS** EUV Imaging Spectrometer

**EUNIS** Extreme Ultraviolet Normal-Incidence Spectrometer

**EUV** Extreme UltraViolet

**FFT** Fast Fourier Transform

**FIO** Flexible Input-Output

**FOV** Field Of View

**FUV** Far UltraViolet

**FPGA** Field-Programmable Gate Array

**FWHM** Full Width at Half Maximum

**GOES** Geostationary Operational Environmental Satellite

**GOF** Goodness-Of-Fit

**GSFC** Goddard Space Flight Center

**HK** House-Keeping

**HLP** House-keeping Link Protocol

**HRTS** High-Resolution Telescope and Spectrograph

**HSL** High-speed Science Link

**I&T** Integration and Test

**ICU** Interface Control Unit

**LCAS** Low-Cost Access to Space

**LISS** Lockheed Intermediate Sun Sensor

**LN2** Liquid Nitrogen

**LOTS** Lockheed Optical Table System

**LVDS** Low-Voltage Differential Signaling

**MASS** Medium Acquisition Sun Sensor

**MDI** Michelson Doppler Imager

**MOSES** Multi-Order Solar EUV Spectrograph

**MRR** Mission Readiness Review

**MSSL** Mullard Space Science Laboratory

**MSU** Montana State University

**NASA** National Aeronautics and Space Administration

**NIST** National Institute of Standards and Technology

**NTSC** National Television System Committee

**PCU** Power Control Unit

**PMF** PreModulation Filter

**PSF** Point Spread Function

**PTB** Physikalisch-Technische Bundesanstalt

**RAL** Rutherford Appleton Laboratory

**ROE** Read-Out Electronics

**SDO** Solar Dynamics Observatory

**SIS** Snapshot Imaging Spectroscopy

**SERTS** Solar EUV Rocket Telescope and Spectrograph

**SMART** Smooth Multiplicative Algebraic Reconstruction Technique

**SOHO** SOlar and Heliospheric Observatory

**SPARCS** Solar Pointing Attitude Rocket Control System

**SPU** Serial-to-Parallel Unit

**SSR** Solid State Relay

**STEREO** Solar TERrestrial RElations Observatory

**SUMER** Solar Ultraviolet Measurements of Emitted Radiation

**SVD** Singular Value Decomposition

**TCS** Thermal Control System

**TEC** ThermoElectric Cooler

**TM** TeleMetry

**TMU** Temperature Measurement Unit

**TRACE** Transition Region And Coronal Explorer

**TU** Timer-Uplink

**ULE** Ultra-Low Expansion

**UT** Universal Time

**VI** Voltage Current(I)

**WAN** Wide Area Network

**WMSR** White Sands Missile Range

APPENDIX B

LIST OF SUPPLEMENTAL MATERIAL

Following is a list of supplemental material included on the CD available from Special Collections in the MSU library.

1. `36193_DR.pdf` – The Design Review document.
2. `flightharness.pdf` – The flight harness specification.
3. `HLP.pdf` – The Housekeeping Link Protocol.
4. `MOSES_MRR_EDP.pdf` – The Mission Readiness Review Experimenter’s Data Package.
5. `Launch.mov` – A video of the launch. It begins with a slow-motion. The full speed video contains sound.
6. `MOSES_flight_sequence.mov` – A movie of the 27 flight images. The data are flat-fielded, dark subtracted, coaligned, and normalized.
7. `moses_ff.tgz` – A GZIP compressed tarball containing IDL code which implements the flat-fielding algorithm in § 4.5 on page 66. The code files unpack into a directory `moses_ff/`.
8. `moses_coregistrate.tgz` – A GZIP compressed tarball containing IDL code which implements the coalignment procedure in § 5.2.1 on page 83. The code files unpack into a directory `moses_coregistrate/`.
9. `EE_1530_0780.mov` – A movie of image triples in the same format as figure 5.2 on page 86.
10. `moses_pa.tgz` – A GZIP compressed tarball containing IDL code which implements the parallax analysis fitting technique described in § 5.5 on page 91. The code files unpack into a directory `moses_pa/`.

11. **smart3Dm.tgz** – A GZIP compressed tarball containing IDL code which implements the SMART algorithm for flight data detailed in § 6.3 on page 126. The code files unpack into a directory **smart3Dm/**.

APPENDIX C

INSTRUMENT ABERRATIONS

Close inspection of flight data reveals instrument aberrations at a level unexpected from the optical design. Figures C.1 - C.3 demonstrate the problem in flight data. We now believe that the primary mirror mount is distorting the mirror such that aberrations are introduced which are different between the  $m = +1$  and  $m = -1$  orders, as well as increasing the size of all three point spread functions (PSFs).

As previously explained in §3.2 we could not focus the outboard orders directly because we lacked an EUV collimator of sufficient quality. We focused the central order and then placed the outboard detectors based on optical calculation from the central order position. This can only be done accurately if the optics as-flown match their design performance.

The focus experiment data raise suspicion. While the design of *MOSES* optics does not give diffraction limited performance in EUV, it should in green light. However the focus spots in figure 3.5 on page 27 and the reduced data in figure 3.7 on page 29 do not show diffraction limited performance. The spots are too big and no diffraction pattern is seen.

The visible differences between PSFs in the different orders, including what appear to be differences in PSF tilt, add systematic error to the interpretation of data. The differences in orders caused by the PSFs will be interpreted as changes in line profiles.

Figure C.4 shows a difference image  $I_{+1} - I_{-1}$  for FOV 1. The two circled objects look like bipolar jets, with a redshift to the north and blueshift to the south. Can we be sure they are real? Anisotropic PSFs could cause a localized object to be imaged differently in the two orders in exactly this way, producing an apparent bipolar jet with no basis in reality. They would produce many such jets in fact, everywhere a small object exists which is separated from any nearby emission measure, and always with the same sense of motion – redshift on top, blueshift on bottom.

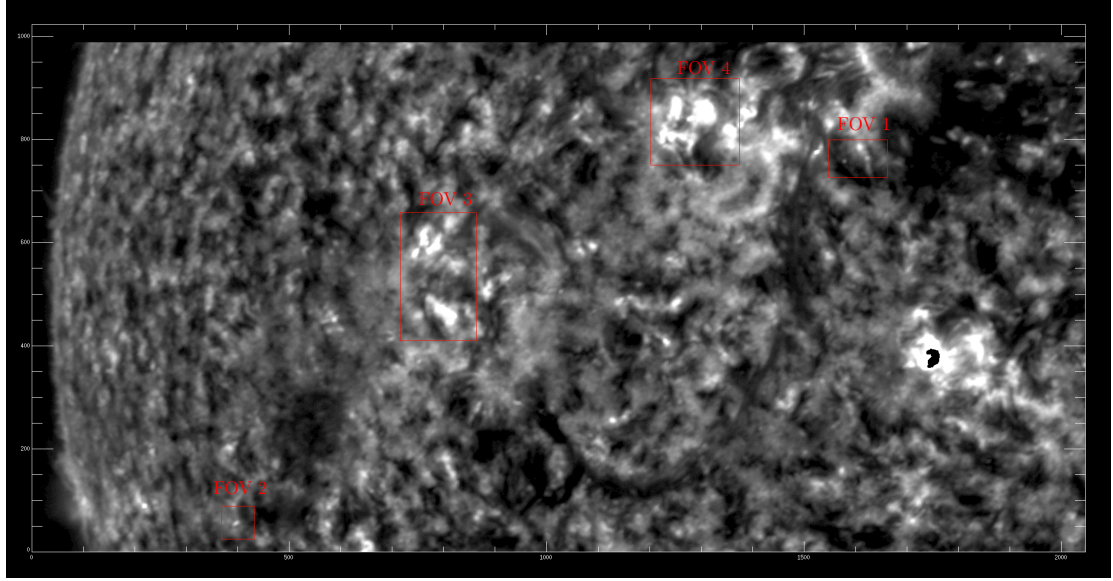


Figure C.1: A  $m = 0$  order image with four fields of view outlined in red. The data from all three orders are shown side by side for each of these FOV's in figs. C.2 and C.3.

Parallax Analysis (see chapter 5) can detect such spurious jets. Unless the PSFs are special<sup>1</sup>, the jet velocities found would depend on which pair of orders is used,  $m = (-1, +1)$ ,  $m = (0, +1)$ , or  $m = (-1, 0)$ . By careful analysis of the results of each pairing it will be possible to determine whether a feature is real and if so quantify the error introduced by the different PSFs.

The affect of the PSF anomaly on inversions is less clear. Our forward model (the projection operator  $\mathbf{T}$ ) does not include any model of PSF. It will therefore be difficult for an inversion algorithm to produce a cube which can fit every order simultaneously when the PSF differs between orders. The  $\chi^2$  values found in §6.3 indicate this. The

---

<sup>1</sup>PSFs that could fool Parallax Analysis would have a particular symmetry. The  $m = 0$  order PSF would be symmetric about the  $y$  axis, and the  $m = -1, +1$  order PSFs would be reflections of each other about the  $y$  axis.

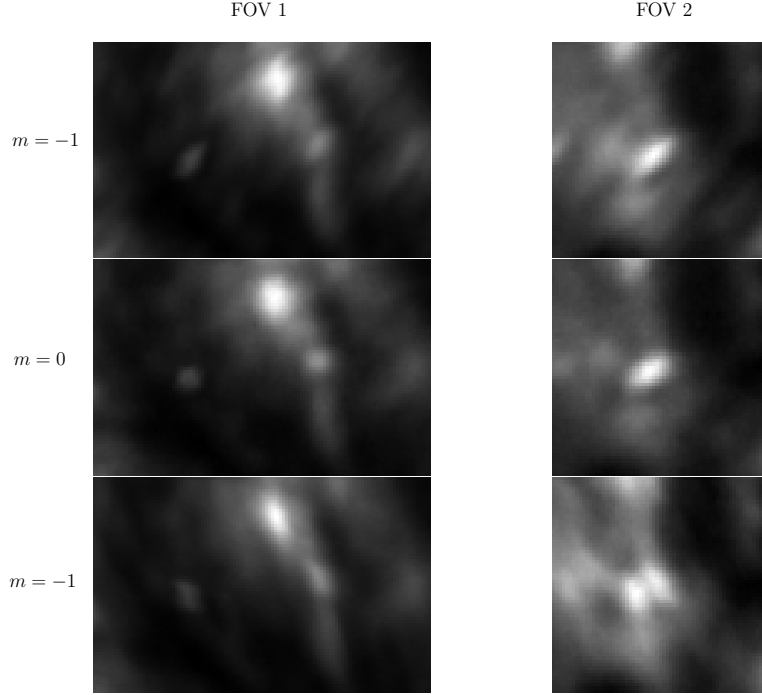


Figure C.2: Comparison of flight data in FOV 1 and 2

SMART algorithm was able to reconstruct a cube which can fit both the  $m = 0$  and  $m = +1$  data. The  $m = -1$  fit however has about twice as much error as the other two orders. The size of the error introduced in the cube is unknown. It may depend on the specific PSFs, the contents of the data, and the reconstruction algorithm used. In the case shown in §6.3 above, the SMART algorithm appears to have “trusted” the  $m = 0, +1$  data more than  $m = -1$ . Clearly more simulations, of the kind performed in §§6.1.1, 6.1.2, and 6.1.3 but with the addition of PSF differences between the orders, will be needed to understand the nature of this error.

Measuring the *MOSES* PSFs in EUV would be helpful. If we knew what they were we might be able to account for them in reconstructions – perhaps by building them into the forward model, or perhaps adjusting the flight data to force a common

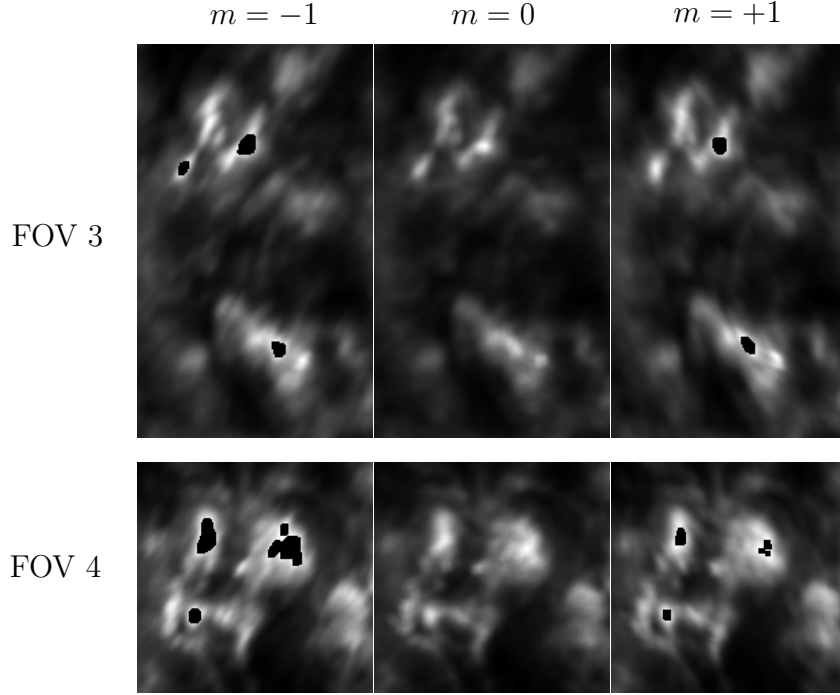


Figure C.3: Comparison of flight data in FOV 3 and 4

PSF<sup>2</sup>. However, currently we have no way to measure the PSFs; this would require an accurate, collimated EUV source sufficient to perform the focus experiment. It might also be possible to infer the shape of the PSFs from the flight data. Attempts to do this so far are very preliminary (Fox & Kankelborg, 2008), but suggest a systematic error of  $22 \text{ km s}^{-1}$  might be introduced in Parallax Analysis. It is clear from figure 5.2 on page 86 that the EE velocities are not greatly affected by this error. Other objects as bright and nearly as compact are visible in the immediate area of the EE and do not show the degree of spectral broadening that it has. There are also isolated, dim, compact objects nearby which show some evidence of possibly spurious bi-directional jets, but the spectral signature is not nearly as pronounced as for the EE.

---

<sup>2</sup>Currently a method of doing this, from flight data alone (without need to know the PSFs), is being worked out (Charles Kankelborg and Shane Atwood, private communication).

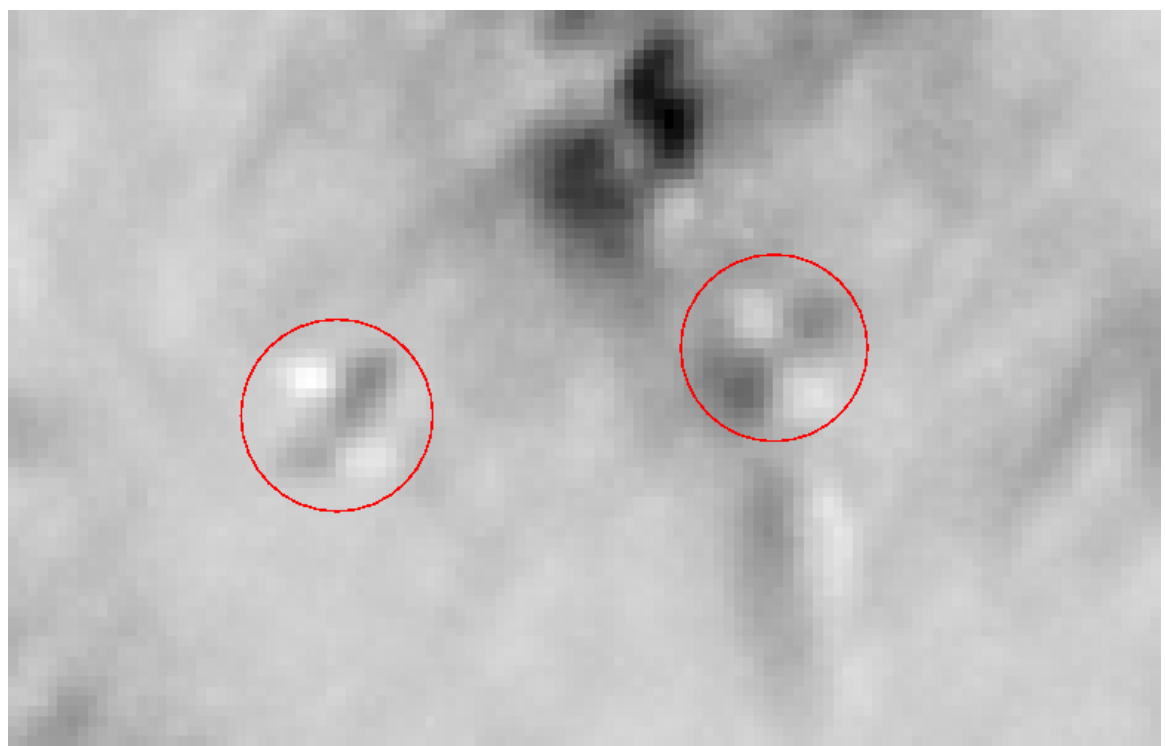


Figure C.4: The  $m = +1$  to  $m = -1$  difference image for FOV 1. Two apparent bipolar jets have been circled.